Motion Compensation Techniques for Aerospace

Denver, Troelz

Publication date:
2005

Document Version
Early version, also known as pre-print

Motion Compensation Techniques for Aerospace

PhD Dissertation by

Troelz Denver

Technical University of Denmark

First edition, December 2004

Printed at:
Measurement & Instrumentation Systems
Ørsted•DTU
Elektrovej
Building 327
Technical University of Denmark
DK-2800 Kongens Lyngby
Denmark

ISBN: 87-91184-45-2

This dissertation was typeset using LaTeX, prepared for printing in a 80% A4 format.

Preface

This dissertation is a part of the fulfilment of the Ph.D. programme in electrical engineering at the Ørsted•DTU institute at the Technical University of Denmark. The work has been carried out within the Space Instrumentation Group at the Measurement & Instrumentation Section. This group is primarily involved in the development of the Advanced Stellar Compass (ASC) star-tracker, and is cooperating with almost all the larger national and international space agencies.

Consequently, this work has been focussed on increasing the operational envelope of the ASC. The work on software filtering for increasing the ionizing radiation tolerance is currently being exploited by the two ASC's onboard the European SMART-1 satellite, which was successfully captured in a lunar orbit mid November this year. The radiation handling work is further planned for several additional high-radiation spacecraft missions.

The work on proving the Bering mission target tracking concept, is further used for public outreach purposes on the University of Hawai'i 20inch telescope. After deployment of the telescope cart, the software package is used for a rapid and accurate alignment of the telescope axes - a task that would otherwise require 10s of minutes of valuable observation time. Alternatively, the software package is directly inserted into the control sequence and used for unaligned tracking and guiding.

The realization of the TDI star-tracker prototype has enabled the star-tracker operation during high angular velocities. This star-tracker configuration is expected to be offered for attitude recovery onboard future spinner satellites.

The effort has further resulted in 4 prime authorship publications and 15 co-authorship publications, which are listed in a separate section.

Acknowledgements

I wish to use this opportunity to thank my colleges at the Measurement & Instrumentation Section at the Technical University of Denmark for excellent and immediate support throughout the project phases, whenever needed. A special thank is directed to my supervisor John L. Jørgensen, Ørsted•DTU for excellent supervision.

As part of the dissertation work a collaboration with the Institute for Astronomy, University of Hawai'i in Hilo was established. I wish to thank the very friendly staff at Hilo for a successful and fruitful co-operation. At the same time, I wish to thank the institute for providing office space as well as access to their 20" outreach telescope.

Finally, this work could not have been carried out without the funding, for which I am deeply grateful. This is partly based on a grant from the "Radioparts Foundation", partly based on the economic overhead generated by the Space Instrumentation Group.

Troelz Denver
December 2004, Kongens Lyngby, Denmark

List of Publications

The following publications have been authored and co-authored as part of the dissertation work:

1. T. Denver, J. L. Jørgensen, T. Riis, M. Betto: "The Autonomy of the Advanced Stellar Compass In-Flight Performance compared to On-Ground Testing", Proceedings of On-Board Autonomy 2001, ESTEC, Noordwijk, The Netherlands, October 2001.

2. T. Denver, P. S. Jørgensen, J. L. Jørgensen, R. Shelton, E. Sousa, J. Hoblitt, M. Maberry: "Autonomous Control of a Mobile 20-inch Outreach Telescope Using a Star-Tracker", 2003 AMOS Technical Conference, Maui, USA, September, 2003.

3. T. Denver, J. L. Jørgensen, M. Betto, P. S. Jørgensen: "The Bering Target Tracking Instrumentation", 1st conference on Recent Advances in Space Technologies, Istanbul, Turkey, November 2003.

4. T. Denver, P. S. Jørgensen, J. L. Jørgensen: "High Accuracy Target Tracking Concepts", in Proceedings of the 4S Symposium - Small Satellites Systems & Services, La Rochelle, France, September, 2004.

5. J. L. Jørgensen, M. Betto, T. Denver: "Onboard Autonomous Correction for Accurate IRF Pointing", AGU Spring Meeting 2002, May 2002.

6. M. Betto, T. Denver, J. L. Jørgensen, P. S. Jørgensen: "Advanced Stellar Compass On-Board Autonomous Determination, Preliminary Performance", New Trends in Astrodynamics and Applications, January 2003.

7. J. L. Jørgensen, M. Betto, P. S. Jørgensen, T. Denver: "Onboard Autonomous Correction for Accurate IRF Pointing", 4th IAA Sym-

posium on Small Satellites for Earth Observation, Berlin, Germany, April 2003.

8. J. L. Jørgensen, T. Denver, M. Betto, P. v. d. Braembussche: "The PROBA Satellite Star Tracker Performance", 4th IAA Symposium on Small Satellites for Earth Observation, Berlin, Germany, April 2003.

9. J. L. Jørgensen, T. Denver, M. Betto, P. S. Jørgensen: "MicroASC a Miniature Star Tracker", 4th IAA Symposium on Small Satellites for Earth Observation, Berlin, Germany, April 2003.

10. P. S. Jørgensen, J. L. Jørgensen, T. Denver, M. Betto: "In-Flight Quality and Accuracy of Attitude Measurements from the CHAMP Advanced Stellar Compass", 4th IAA Symposium on Small Satellites for Earth Observation, Berlin, Germany, April 2003.

11. M. Betto, J. L. Jørgensen, P. S. Jørgensen, T. Denver: "Advanced Stellar Compass Deep Space Navigation, Ground Testing Results", 5th IAA Conf. on Low Cost Planetary Missions, ESTEC, Noordwijk, 2003.

12. J. L. Jørgensen, P. S. Jørgensen, M. Betto, T. Denver, L. J. Tuñón: "Enhanced Mission Performance from Autonomous Instrument Guidance", 5th IAA Conf. on Low Cost Planetary Missions, ESTEC, Noordwijk, 2003.

13. M. Betto, J. L. Jørgensen, P. S. Jørgensen, T. Denver : "Bering Mission Navigation Methods", 1st conference on Recent Advances in Space Technologies, Istanbul, Turkey, November 2003.

14. J. L. Jørgensen, T. Denver, M. Betto, P. S. Jørgensen: "The Bering Autonomous Target Detection", 1st conference on Recent Advances in Space Technologies, Istanbul, Turkey, November 2003.

15. P. S. Jørgensen, J. L. Jørgensen, T. Denver, M. Betto, L. J. Tuñón: "Autonomous Target Ranging Techniques", 1st conference on Recent Advances in Space Technologies, Istanbul, Turkey, November 2003.

16. P. S. Jørgensen, J. L. Jørgensen, T. Denver: "Using an Autonomous Star Tracker As Formation Flying Sensor", in Proceedings of the 4S Symposium - Small Satellites Systems & Services, La Rochelle, France, September, 2004.

17. J. L. Jørgensen, T. Denver, P. S. Jørgensen: "Micro-ASC: The Next Step in Star Tracker Technology", in Proceedings of the 4S Symposium - Small Satellites Systems & Services, La Rochelle, France, September, 2004.

18. J. L. Jørgensen, T. Denver, M. Betto, P. v. d. Braembussche: "The PROBA Satellite Star Tracker Performance", to appear in Acta Astronautica Journal, Vol. 56, Issue 1-2, pp 153-159. International Academy of Astronautics, 2005.

19. P. S. Jørgensen, J. L. Jørgensen, T. Denver, M. Betto: "In-Flight Quality and Accuracy of Attitude Measurements from the CHAMP Advanced Stellar Compass", to appear in Acta Astronautica Journal, Vol. 56, Issue 1-2, pp 181-186. International Academy of Astronautics, 2005.

Abstract

The subject of motion compensation techniques for aerospace applications is presented in this work. A special focus has been put on motion effects for low-light imaging applications.

In order to connect the two fields of motion and imaging, a thorough introduction to each of them is given. The imaging implications caused by the described motion regimes are then derived.

Before motion compensation can take place, a characterization of the motion must be established. A number of different techniques are presented, primarily based on a rotating imaging platform in a stationary scene.

After motion characterization, the actual compensation can take place. Different techniques are presented including opto-mechanical stabilization, CCD based compensations and post-processing methods.

Four case studies related to star-tracking, being a low-light application, are presented and possible solutions are proposed, implemented and verified:

1. *Star-Tracking at High Rotation Rates.* Since star-tracking is based on image acquisition of stars, operation onboard a fast rotating spacecraft is facing considerable challenges. From analysis it is found that the time delayed integration is the most suitable compensation technique. The analysis, implementation and the verification are discussed. Finally, the test results are presented.

2. *Target Tracking.* The Bering mission is presented, being a deep space vehicle targeted for a mapping of the asteroid population. It is discussed how science instruments can be aimed at the targets in the fastest and most reliable way. The representative ground tests proving the concept are described, and the obtained results are given.

3. *Two-Stage Star Tracking.* The need for a highly accurate rotation characterization of rotating platforms surpass the performance of the

most accurate star-trackers. A star-tracker system containing two optical stages is described, hereby improving the angular velocity determination accuracy by increasing the resolution and sensitivity of the star-tracking. The results from real sky tests on both a meagre and a rich star-field are presented and evaluated.

4. *Star-Tracker Radiation Handling.* When a CCD is subjected to ionizing radiation, charges are being generated. Since this effect is highly similar to the image of a star, this effect impose a sizable challenge to star-tracking. This phenomenon is investigated and a mitigation solution is found. In-flight results from the European satellite mission SMART-1 are presented to demonstrate the performance.

Resumé

Emneområdet bevægelseskompensering indenfor rumfart bliver behandlet gennem dette arbejde. Der er specielt fokusseret på effekter fra bevægelser på applikationer der anvender billedtagning ved lav lysintensitet.

For at kunne forbinde de to felter, bevægelse og billedtagning, bliver der givet en grundig introduktion til begge. Implikationerne for billedtagningen, forårsaget af de beskrevne bevægelsesregimer bliver efterfølgende udledt.

Inden bevægelseskompensering kan finde sted, må den pågældende bevægelse karakteriseres. Der præsenteres flere forskellige teknikker, primært baseret på en roterende billedtagningsplatform i en stationær scene.

Når bevægelsen er karakteriseret, kan den aktuelle kompensering finde sted. Forskellige teknikker bliver præsenteret, herunder opto-mekanisk stabilisering, CCD baseret kompensering og efter-processeringsmetoder.

Fire cases bliver presenteret, relateret til anvendelse af et stjernekamera, som er en applikation der anvender billedtagning ved lav lysintensitet. Mulige løsninger bliver udledt, implementeret og afprøvet:

1. *Anvendelse af et stjernekamera ved høje rotationsrater.* Da et stjernekamera baseres på billedtagning ved lav lysintetsitet, er anvendelsen af disse en betydelig udfordring ombord på hurtigt roterende rumskibe. Gennem analyse udledes, at tidsforsinket integration (TDI) er den bedst anvendelige kompenseringsteknik. Analysen, implementeringen og afprøvningen bliver diskutteret. Endeligt vises resultater fra testen.

2. *Fastholdelse af et bevægligt mål.* rummisionen Bering, der er et fartøj planlagt til at kortlægge bestanden af asteroider, bliver præsenteret. Det bliver diskuteret, hvordan et videnskabeligt instrument kan udpege målene på den hurtigste og mest pålidelige måde. De repræsentative tests der beviser konceptet beskrives, og resultaterne fra målingerne gives.

3. *Anvendelse af et to-trins stjernekamera.* Behovet for en meget nøjagtig

karakterisering af bevægelserne på roterende platforme, overstiger ydeevnen for de mest nøjagtige stjernekameraer. Et stjernekamerasystem bestående af to optiske trin beskrives, hvilket vil forbedre den målte vinkelhastigshed ved både at have større opløsning og følsomhed. Resultater fra afprøvninger på tætte og spredte stjerneregioner præsenteres og vurderes.

4. *Anvendelse af et stjernekamera ved ioniserende stråling.* Når en CCD udsættes for ioniserende stråling, bliver ladninger fejlagtigt genereret. Siden denne effekt ligner billedet fra en stjerne, udgør den en anseelig udfording for anvendelsen af stjernekameraer. fænomenet undersøges, og en løsningsstrategi findes. Resultater fra anvendelsen ombord på den europæiske satellit SMART-1 præsenteres for at demonstrere anvendeligheden.

Contents

List of Figures

List of Tables

Abbreviations

as	Arc-seconds (1/3600°)
ADC	Analog to Digital Conversion
AO	Adaptive Optics
ASC	Advanced Stellar Compass
APS	Active Pixel Sensor
BOI	Beginning Of Integration
CCD	Charge Coupled Device
CDS	Correlated Double Sampler
CHU	Camera Head Unit
COI	Center Of Integration
DPU	Data Processing Unit
EFL	Effective Focal Length
FOV	Field Of View
FPGA	Field Programmable Gate Array
mas	milli arc-seconds
MTF	Modulation Transfer Function
PSF	Point Spread Function
PPS	Passive Pixel Sensor
QE	Quantum Efficiency
S/N	Signal/Noise
TG	Timing Generator

Nomenclature

In order to discern between different mathematical symbols, the following conventions are applied:

Variables: All letters denoting a mathematical variable will be represented in *italic* notion, e.g. x, η and $\bar{\bar{A}}$.

Mathematical Functions: All mathematical functions will be represented in standard lowercase typeface notion, e.g. $\sin\omega$, $\mathrm{tr}(\bar{\bar{A}})$.

Scalars: The scalars will be represented using lowercase letters. Generic variables that can only take integer values will be: $\{i, j, m, n\}$, while floating point variables will be: $\{u, v, x, y, z\}$.

Vectors: The vectors will be represented with lowercase letters with a bar, e.g. $\bar{p}$, $\bar{\tau}$. An exception to this standard is the rotation vector, Ω.

Matrices: The matrices will be represented with uppercase letters with a double bar, e.g. $\bar{\bar{A}}$ and $\bar{\bar{V}}$. An exceptions to this standard is the matrix realization of a reference frame, R.

Set: A set is a discrete group of values. The notion $i \in \{1..3\}$ means that the value of i can be equal to the integer values 1, 2 or 3.

Range: A range is a continuous group of values. The notion $x \in [1..3]$ means that the value of x can be equal to any floating point number between 1 and 3, both included.

The following list shows the variables and the assigned symbols used throughout the dissertation.

Symbol	Desciption
b	Radiation
$p_{x,y}$	A pixel in the image plane
$\bar{p}$	Scene position (given as a vector)
t_x	Time for event x
c	Centroiding accuracy
$\bar{\bar{A}}$	Attitude
B	Intensity
I_x	Image number x
L	List
$M_{m,n}$	Matching pair
N	A number of a certain category
O	Object
P	Plane
R	Reference frame
T_{int}	Integration time
T_{img}	Imaging interval
T_{pix}	Time for an object to move one pixel
α	Right-Ascension
β	Half angel field of view
δ	Declination
θ	Angle (azimuth)
η	S/N ratio
ξ	Noise
σ	Standard deviation
τ_x	Image token number x
υ	Velocity (linear)
ϕ	Angle
ω	Rotation angle
$\dot{\omega}$	Angular velocity
Δ	A given (small) range
Φ	Solid angle
Ω	Rotation vector

Chapter 1

Introduction

"I could have gone on flying through space forever", Yuri A. Gagarin.

Space-borne platforms realize a unique opportunity for science measurements, observation and commercial utilization that cannot be achieved from ground. The absence of atmospheric seeing and light pollution serve as excellent conditions for astronomical applications. The possibility of direct and constant visibility from a large ground segment is exploited on geostationary telecommunication satellites. The extended visibility from ground are further exploited by the constellation of 24 active GPS satellites located in six 20,200km altitude orbits, which are widely used for navigation. Earth observation satellites in low Earth orbits utilize the combination of the rotating Earth and the selected orbit to perform Earth observation and mapping measurements, with almost global coverage within a few days. Deep space satellite missions escape the Earth gravity field to approach unexploited celestial bodies and perform "close-up" scientific measurements that can never be achieved from ground. On top of this, several strategic applications can be imagined.

Apart from the orbital parameters defining the motion, an attitude profile for any mission is required. A telescope must be pointed towards a target for a given period of time, while solar intrusion must be avoided, solar panels must be pointed towards the Sun in order to generate power for the spacecraft, the communication antennas must be pointed towards ground during ground contact, and so forth. Any spacecraft is in itself an inertial body, which will be rotating freely if not actively controlled. Such a control is obtained using an *attitude control system* (ACS).

The latest development within the field of microelectronic and sensor

techniques has been striving for a continuous component miniaturization. These technological advances are of particular interest for the aerospace field, mainly due to the very high costs associated with launching heavy equipment. Unfortunately, smaller spacecraft probes face increasing challenges for (at least) two reasons:

1. Inertia and torque does not scale linearly with the size of the probe. Smaller probes are intrinsically more unstable than larger probes. A given disturbance will therefore have considerable higher impact on smaller probes.

2. A smaller antenna aperture will lead to a more narrow communication bandwidth. The operational autonomy hence required by the probe will pose higher performance requirements on the ACS.

During the last 15 years, researchers at the Technical University of Denmark have developed state of the art star-trackers. These reference attitude sensors are flying on-board, and planned for, the most demanding spacecraft missions. Since a star-tracker is based on integration of a relatively low directive photon radiation from the stars, a relatively long integration period is required to obtain a sufficient S/N ratio. As a consequence, it is highly sensitive to any type of motion.

Consider such a star-tracker being operated on a rotating spacecraft. The image acquisitions of the star-field will yield images of elongated stripes instead of distinct luminous point-like objects. Apart from posing challenges detecting the stars, the accuracy of the determined star positions is decreased. As a consequence, the performance will be degrading rapidly as the angular velocity is increasing. There is a large international interest on developing compensation methods for this kind of motion. The work has mainly been focused on post-processing techniques, but also pre-acquisition compensation techniques is studied. The currently most successful pre-acquisition technique is the *Time Delayed Integration* technique, where the image is moved accordingly with the motion inside the focal plane detector during integration. This technique is successfully implemented on several leading astronomical telescopes of the world, and could, implemented on a star-tracker, form a very powerful instrument for high-rate attitude recovery.

A second pre-acquisition motion technique for motion compensation, is to place a light-weight folding mirror in front of the star-tracker. By tilting the mirror, the irradiated photons paths can be redirected in the desired direction. By carefully controlling the tilt angles according to the motion,

long periods in a given pointing direction can be achieved even for fast rotating platforms. By co-aligning a star-tracker and e.g. a telescope, such that both instruments are capturing the scene through the folding mirror, a closed loop telescope pointing can be realized. In addition, since the star-tracker is capable of determining and outputting the pointing direction of moving objects, this instrument suite serve as a unique platform for closed loop tracking of moving targets. Such a configuration is proposed for the Bering satellite mission, which are planned to observe asteroids from within the asteroid belt. The onboard telescope control exploits the attitude information and the target direction from the star-tracker, to point and maintain the target in the telescope center during observation. Several other applications of this configuration can be imagined, ranging from pointing of laser communication equipment to strategic applications, such as detection and tracking of missiles within a defense network.

The objective of this work is to investigate spacecraft motion in general, with a particular focus on motion types that are relevant to star-tracking applications. Mitigation strategies will be developed, implemented and verified for the identified motion fields. The main design drivers for space instrumentation listed below will be considered as an important part of the feasibility analyses.

1.1 Realization of Aerospace Instruments

Generally, the realization process of space instrumentation is highly different from the realization of ground applications. This process is mainly driven by the following factors:

- Challenging conditions. The space environment is highly different from the ground environment, including vacuum, no humidity, rapidly changing platform temperatures and high radiation levels.

- Limited operational budgets. The high costs associated with space applications usually limits the design budgets, such as power consumption and mass. Also secondary budget elements such as computational power and computer memory usage are limited.

- System reliability. Since space operation is very costly, very strict scientific (and political) requirements to success rate, accuracy and reliability are usually imposed.

- Flight qualification. Since the space-environment is very different from the ground a complete verification can never be performed. Instead, ground tests as representative as possible are defined. One such comparison between ground measurements and in-flight measurements for a star-tracker has been performed and published as part of this work [6].

1.2 Problem Delimitation

As presented in the previous section, the topic of aerospace applications are posing high constraints for the algorithms sought. The theoretical study and the proposed solutions is thus constrained to a limited envelope:

- Autonomous operation. In order to reduce response time and operator requirements, only techniques that can operate autonomously will be considered.
- Short data latency. Since the algorithms sought will operate in closed loop with a spacecraft guidance system, a short temporal latency is required. Thus only compact, fast executable and highly optimized algorithms will be considered.
- Simple interface requirements. Only a limited amount of traffic can be sent across the spacecraft/ground link. Thus, only algorithms relying on a minimum of external information will be treated.
- Limited processor budget. Since the solutions proposed must be prepared for spaceborne systems with a limited amount of computation power, computational heavy algorithms will be disregarded.
- Low light applications. Since the effects from image motion scales linearly with integration time, these effects will be accentuated for low-light applications. Focus will therefore be on this class of applications.

In order to demonstrate (some of) the algorithms presented in the theoretical study, four different fields of motion associated with star-tracking have been identified:

1. *Star-Tracking at High Rotation Rates.* Since the star-tracker operates by observing stars, a rotating platform will cause a smearing in the imaged stars. For increased rotation rates, such a smearing will lead

to either an accuracy decrease or a failure to recover the attitude. A solution to this problem will be pursued, preferably without any mechanically moving components.

2. *Target Tracking.* A small deep-space vehicle is planned for an asteroid population mapping. A pointing instrument will be used to collect the scientific information foreseen. Since the relatively heavy instrument is located on a rotating platform, mechanical pointing will induce high torques on the spacecraft body. A solution is sought, taking into account the standard space instrumentation design drivers (§1).

3. *Two-Stage Star Tracking.* Sub-arcsecond motion knowledge is required for deep astronomical observation. Since a star-tracker pointing accuracy is highly dependent on the field of view of the optics, a more accurate setup is sought. The feasibility of a two-stage star-tracker featuring a higher resolution and sensitivity will be investigated.

4. *Star-Tracker Radiation Handling.* When a CCD is subjected to ionizing radiation, charges are being generated. The effect on the following image, is the appearance of a white dot in the associated pixel. Since this effect is highly similar to the image of a star, this effect impose a sizable challenge to star-tracking. This phenomena will be investigated and a solution will be demonstrated.

Chapter 2

Theory

2.1 Thesaurus

In order to avoid ambiguity and to support the descriptions in the following chapters, some of the applied notions are shortly summarized in this section.

Image An image is a discrete recorded state of a system, in motion or at rest, at a specific point in time (§2.2). In this work, the definition will be confined to discrete 2D mono-chromatic photographic imaging of low-light applications.

Distortion is for photographic imaging the deviation between the given image of a scene, and a projection of the scene made through a perfect lens. For scene elements close to the imager, perspective displacement will be dominant. For imager systems featuring a low focal length/lens aperture ratio (F number), a radial rotational-symmetric projection displacement will occur as well, often referred to as barrel and pin-cushion distortion [3].

Point Spread Function or PSF describes the lens system response to a spatial point source, defined by a Dirac delta function. A description of the PSF is given by Horn [10].

Modulation Transfer Function or MTF describes the lens system response to spatial frequencies. The real part of the MTF corresponds to the particular frequency attenuation while the imaginary part is an applied phase delay. Horn [10] gives a good introduction to the MTF.

Image processing is defined as operations performed on the image, leading to a new image. Such processing techniques include blurring, sharpening, filtering, edge enhancement, etc.

Image analysis is similarly defined as operations performed on an image. However, this operation leads to a feature vector containing application dependent information found in the image. Analysis techniques include centroiding, motion detection, etc.

System Noise is the deviation between the projected scene and the final quantized image at pixel level. Typical noise contributions originate from thermally induced noise, readout noise, electronics noise, quantization noise, etc. System noise is treated in more detail in §2.3.5.

Detectability is the ability of a given signal to be detected. The detectability is highly dependent on the S/N ratio (§2.4.3) and the image motion (§2.4.4).

Sampling Frequency or imaging frequency is the number of images recorded pr. unit time. The inverse of imaging frequency is imaging interval that is the time between two image recordings.

Image Tokens are unique areas within an object or a scene, being corners, discrete changes in illumination levels, etc. If the system is at rest, any subsequent image will contain the same tokens at the same locations. See §2.5 for a more thorough description.

Perfect Lens is defined as a lens system that can be described by the pinhole approximation and having an aperture large enough to allow for the irradiation required by the given application. The properties of a perfect lens are therefore:

- A PSF being a delta-function
- No optical distortion
- Having a uniform response
- Focuses at all distances
- The focal length f is equal to the distance between the lens center and the focal plane.

Attitude is the 3-axis orientation of a given device within a given reference frame. The attitude can be decomposed into a unit pointing vector (2 degrees of freedom) plus a given rotation about the pointing vector.

Optical Axis of a lens system is defined as the symmetry axis of the lens elements. For a optimal focus, the optical axis must be orthogonal to the image sensor plane.

Star Proper Motion is the apparent motion of the individual celestial stars as observed in an inertial reference frame. For most stars, this motion is below 1as/year.

2.2 Theoretical Imaging

An image is a discrete recorded state of a system, in motion or at rest, at a specific point in time. If an image I is recorded of a system $S(t)$ we have generally I=S(t). At time $t = t_1$, the image will be denoted I_1, such that

$$I_i = S(t_i) \tag{2.1}$$

The system to be imaged is built up from $N \in \mathbf{Z}*$ logical subsystems $s_n(t)$ such that

$$S(t) = \sum_{n=1}^{N} s_n(t) \tag{2.2}$$

Each subsystem $s_n(t)$ may again be built from smaller logical subsystems, etc.

If the state of the system is later recorded at a time $t = t_2$, where $t_2 > t_1$, a new image I_2 will be generated. If the state of the system has changed from $t = t_1$ to $t = t_2$, I_1 will be different from I_2. That is:

$$I_1 \neq I_2 \Leftrightarrow \exists i : s_i(t_1) \neq s_i(t_2) \qquad i \in \mathbf{Z}*, i \leq N \tag{2.3}$$

The reverse operation of imaging will be denoted reconstruction. This procedure recreates a discrete copy of the original system, $\widehat{S}$, based on 1 or more recorded images of $S(t)$. If the reconstructed system is equal to the original system, the imaging is denoted lossless. If the reconstructed system contains only a part of the original system, the imaging is denoted lossy.

The system $S(t)$ can take any given form. Typical applications for imaging include:

Computer backup - where an instant image of the harddisk is created and saved in case of a future computer malfunction. In this case $S(t)$ will be the state of a selected part of the harddisk. $s_n(t)$ will be either a physical subdivision of the harddisk (e.g. sectors) or a logical subdivision of the disk such as directories or files.

X-ray imaging - where an instant image of a projection of some occluded structure is recorded.

Photographic imaging - where a projection of a scene (e.g. a landscape) is recorded. Here the system $S(t)$ is composed of some trees, a river, some clouds, etc. . . , constituting the subsystems $s_n(t)$.

For all imaging applications a dedicated set of *constraints* exists. For the computer harddisk imaging, the state of the system is well established, it is deterministic and the system will change only at discrete points in time, defined by the user (for most operating systems). In addition, the system state can be measured in discrete levels (either 0 or 1) which means that the original system can be reconstructed based on the image. This particular case therefore constitutes a lossless imaging application. The x-ray imaging application is constrained by having a poor resolution and signal to noise ratio. On top of this, the nature of this application is constrained to yield a 2D projection of the 3D system to be imaged, wherefore a complete system reconstruction is impossible.

This work will be confined only to discuss photographic imaging. Several of the mechanisms and processing tools are shared with other imaging applications, but in order to treat the phenomenons associated with this particular imaging branch, this confinement is unfortunately necessary.

2.2.1 Photographic Imaging

Photographic imaging is based on the fact that all body surfaces will radiate[1] a certain amount of photons. Either the photon radiation is emitted due to internal processes[2] (such as the Sun, or light from a flash-light) or the photons are reflections or scatters of irradiated photons (such as the ground at night, when illuminated by a flash-light).

In either case surface materials with different characteristics will result in a difference in the frequency distributions of the radiated photons. Certain materials will have a high radiation at certain frequencies while other materials will have complete different frequency distributions. This difference is for instance used by the human eye to isolate and identify different types of body surfaces in an image.

If the photon flux of a certain surface element radiation is $b(\nu)$, ν being

[1] Radiation is defined as a combination of emission and reflection

[2] atomar, molecular or chemical processes

a given frequency, the intensity of the radiation, B_r, is defined as

$$B_r = \int_0^\infty b(\nu)d\nu \tag{2.4}$$

In order for the image to be recorded, a detector that is capable of detecting the photons in the various frequencies is needed. A discussion of different detector types is found in §2.3.1. A detector will not be equally sensitive to all photon frequencies. This sensitivity is often referred to as the quantum efficiency, $q(\nu)$, which again depends on the photon frequency ν. The total intensity obtained by a certain detector, B_d can therefore be found as

$$B_d = \int_0^\infty b(\nu)q(\nu)d\nu \tag{2.5}$$

In case only a selected spectral region is desired, an optical filter transmitting only a selected frequency band and reflecting the rest can be inserted in the optical pathway. If the spectral transmission of the filter is $f(\nu)$ the filtered intensity obtained by the detector B_f can be found from:

$$B_f = \int_0^\infty b(\nu)q(\nu)f(\nu)d\nu \tag{2.6}$$

Imaging systems capable of detecting only intensities will be referred to as being mono-chromatic, while imaging systems capable of performing a spectral separation will be referred to as being multi-spectral.

Multi-spectral imaging systems, in which different spectral bands are resolved can be realised in a number of ways. A typical application is the human eye, in which three different detectors types (called cones) are used in daylight conditions [10]. Each of the three types has it's own quantum efficiency function.

Another application is standard chromatic photographic film on which the photosensitive dye is built in three layers: (From the bottom) red, green and blue sensitive [25]. When a low frequency "red" photon enters, it is passing the green and blue sensitive layer and is not absorbed until it hit the red sensitive layer. An obvious advantage with this technology, is that all surface parts of the photosensitive layer can be designed to have a uniform spectral sensitivity.

Finally, the multi-spectral scene can be partially reconstructed by combining images that have been recorded using different optical filters. A clear disadvantage using this approach is that for physical reasons the three image acquisitions will be separated in time, wherefore risk of scene motion

is existing. One way to solve this problem, is to use a suite of detectors, such that the reflected light from the first filter is either recorded by a second detector or passed on to a new filter system. An example of such an application is given in [22].

The applications further described in this work will be confined to monochromatic imaging (unless otherwise specified).

2.2.2 Surface Reflection Properties

Dependent on the small scale structure of the surface all incoming photons will not be reflected uniformly. If the surface structure is small relative to the photon wavelength, the photon will be reflected according to a simple mirroring. Such a surface is referred to as being specular.

On the other hand, if the small scale structure of the surface is large compared to the photon wavelength it will be reflected in a diffuse manner dependent on the wave phase at the impact. This surface structure is referred to as being Lambertian. In an ideal Lambertian surface, the reflection will uniformly cover the hemisphere defined by the surface normal, disregarded the incident angle.

A good example of a specular surface for photons in the visible range is a mirror. Almost all incident photons will be mirrored according to the surface normal. Another example is a satellite television receiver dish. This surface is specular for the long wavelengths used for carrying the video signals (otherwise it wouldn't focus the signals onto the receiver). On the contrary, it is not specular for the short wavelengths in the visual range.

Usually, a surface will contain a certain amount of both reflection types. The combination of the two surface properties maps into a hemispherical distribution of reflected photons as function of the hemispherical distribution of the incident photons. This distribution function is often referred to as the Bidirectional Reflectance Distribution Function (BRDF) which is further described by Horn [10].

2.2.3 Image Focusing

Consider three Lambertian surface patches, each reflecting photons from a common light source. A photo-sensor is positioned such that it is irradiated by reflected photons from all three surfaces.

Even though the sensor is irradiated by all three surfaces, it is impossible to separate the three surfaces from the recorded image. In order to enable this separation, the photons must be focused.

A very simple way to perform this focusing, is to place a cover at a certain distance f (referred to as the focal length) in front of the sensor with an infinitely small entrance hole (pupil). Since the photons will always follow the shortest path, the photons reflected from one surface patch will be forced to irradiate the sensor at a well defined location.

Such focussing of an imaging system is referred to as a pinhole approximation, in which a theoretical perspective projection is realized, in contrast to an orthographic projection [20].

2.3 Applied Imaging

2.3.1 Photon Sensor Types

In order to perform the image recording, i.e. acquire the irradiated photons, an image sensor must be introduced. Previously, the human eye was introduced as a sensor, capable of detecting photons of three different frequency distributions. The recorded images are either stored in the human brain, processed, ignored or redirected to subjective "hard-copies" in the form of paintings or drawings.

At the early introduction to photography, large photographic plates containing light sensitive dye were applied. They were later replaced by the film roll, first based on paper, later on a celluloid, such that several images could be recorded without opening the camera system.

With the later introduction to the solid-state semiconductor technology, photo diodes and photo transistors exploit that an irradiated photon generates an electron-hole pair, that can be measured as a (small) electric charge [2]. For two-dimensional arrays the CMOS based Passive Pixel Sensor (PPS) exists, in which the individual pixels are selected using a row and column selector. For low(er)-light applications, signal amplification is performed directly at pixel level in the Active Pixel Sensor (APS). Finally, the Charge Coupled Device (CCD) technique implements a readout format, in which the images are read out one full line at a time.

Generally, the CCD is recognized to be superior to the CMOS technology with respect to image quality, measured in: Dynamic range, uniformity, quantum efficiency (QE) and fill-factor. On the other hand, the CMOS imagers are superior in more practical measures, such as: Speed, Access and cost [18]. For high yield applications the CCD based sensor is often selected, whereas for consumer applications, the CMOS sensor will typically be implemented.

Since the essential topic for this work is autonomous compensation for image motion, only imaging systems based on a computer back-end will be considered. The following sections will therefore be based on array sensors such as the CMOS and CCD type in order to reduce imager/computer interface complexity (unless anything else is specified).

2.3.2 Spatial Resolution

The sensor architecture is built around a number of charge storages, each capable of storing the electrons liberated from the incident photons. These charge carriers are located in an array defined by rows and columns. Since the electrons stored within one charge carrier cannot be individually resolved, the spatial resolution of the imager is defined by this "binning".

One such bin is referred to as a pixel having an area $A = \Delta x \Delta y$, where Δx and Δy are the physical extents along the x-axis and the y-axis of the imaging plane. These rectangular pixels are placed in a grid covering the entire imaging plane. The individual pixels can be addressed by a column and row identifier, where the rows follow the x-axis, and the columns follow the y-axis. I.e. pixel $p_{i,j}$ is found in column i and row j. $p_{0,0}$ is centered in the intersection between the optical axis and the imaging plane. If the photon intensity at the surface of the image plane at (x, y) is $B(x, y)$ the irradiating pixel intensity, $b_{i,j}$ is:

$$b_{i,j} = \int_{(i-\frac{1}{2})\Delta x}^{(i+\frac{1}{2})\Delta x} \int_{(j-\frac{1}{2})\Delta y}^{(j+\frac{1}{2})\Delta y} B(x, y) dy dx \tag{2.7}$$

Some architectures place the pixels in a triangular or a hexagonal grid for better symmetry and packing. In the following descriptions, a rectangular grid will be assumed.

A right handed orthogonal coordinate frame can now be defined: The x- and y-axis are located in the imaging plane following the pixel rows and columns, while the z-axis is parallel to the optical axis (going out of the photosensitive surface). For a well calibrated camera system, the optical axis is orthogonal to the imaging plane, intersecting the plane in the center pixel. The entire coordinate frame realized is hereby orthogonal. The origin of the coordinate frame is located i the intersection between the optical axis the the imaging plane.

Consider now the imaging plane being covered by a plate parallel to the imaging plane at a distance f. The plate contains an infinitely small hole at the intersection between the plate and the optical axis, such that a pin-hole

approximation is implemented. The irradiation of each pixel is now limited to radiation stemming from a well defined portion of the scene, bounded by the four vectors, defined by:

$$\begin{bmatrix} -(i \pm \frac{1}{2})\Delta x \\ -(j \pm \frac{1}{2})\Delta y \\ f \end{bmatrix} \tag{2.8}$$

2.3.3 Lensing

The process of a surface radiating a photon is by nature a discrete event. For a reflection, it is (among other things) obviously dependent on the irradiated intensity. The radiation of a surface patch can therefore only be described by a certain probability distribution.

One consequence of probability distributions is that the probability of an event taking place within a certain constraint window will be infinitely small as the constraint window size is decreased towards infinitesimal sizes.

Consider the surface radiating an imager plane through a pin-hole approximation. The probability of a photon radiated from the surface having the exact direction required for passing the infinitely small hole is also infinitely small. The hole therefore needs to have a certain size, in order to allow a non-zero probability for having incident photons.

Increasing the hole size obviously has the undesired effect of blurring the image projection in the image plane. Alternatively, a lens can be applied in the position of the pin hole. The lens has the effect, that for a perfectly focussed system, all light irradiating the lens from the same point source, will be focussed on the same point in the image plane. Since the extent of the lens is of a certain size, the probability of irradiation is non-zero.

Introducing a lens to an imaging system, does also introduce certain limitations, which will only be briefly mentioned here for completeness. The lens can only be focused at a specific distance. If several objects located at different distances are to be imaged, all objects cannot be completely focussed. The lens refraction will depend on the wavelength of the irradiation, such that different wavelengths will be focussed differently, leading to chromatism. Typically, the lens system will be implemented in more than one stage introducing vignetting and distortion effects. Please refer to e.g. [3] for a thorough description of lensing effects.

All effects described grow with the lens aperture, wherefore it should not be larger than absolutely needed.

2.3.4 Exposure Time

Consider a point source of a scene being projected on an imaging plane through a lens system. The radiation is Lambertian having an integral intensity B_r. The size of the lens, given as a solid angle as seen from the object, is Φ (in steradians). The amount of photons irradiating the image plane during the timeslot Δt is:

$$I = B_r \frac{\Phi}{2\pi} \Delta t \tag{2.9}$$

The amount of irradiated photons stemming from one point source is therefore proportional to the size of the lens as well as the permitted timeslot. A particular imaging application can therefore be optimized by adjusting these two parameters. The allocated timeslot is often referred to as exposure time for analogue systems, and integration time for digital systems. Since this work has been confined to digital applications, the expression integration time will be applied.

A severe drawback from increasing the integration time is when the scene is not static but in motion. If the integration time is increased such that a point source object is focussed on several pixels during integration, the projection will be smeared. The main topic of this work will be detection of such object motions, compensation techniques as well as post-processing methods.

2.3.5 Noise Performance

The classical measure of noise performance is to measure the signal relative to the noise floor, or the S/N ratio. One important feature is that the system amplification is omitted by the measure, because both signal and noise will be amplified evenly.

The S/N ratio can be maximized in one of two ways: Either the signal can be maximized or the noise can be minimized. As described earlier, signal maximization can be accomplished by increasing the lens aperture (with the added consequences of distortion and optical aberration) or by extending the integration period.

The noise can be minimized by the imager design in a number of ways. The dominant contributions to noise are:

Photon count noise is noise or deviations between the image projection and the true scene stemming from an insufficient number of photons irradiating the image plane. Such noise contributions follow a Poisson

distribution as opposed to the noise contributions described later, that will follow a Gaussian distribution.

Dark current noise is thermally released charges within the focal plane detector. One obvious method for reducing this effect is to decrease the operational temperature.

Read-out/system noise is the noise added by the sensor and support electronics. Noise of this class can be minimized by a proper electronics design including a well defined grounding philosophy, cascaded amplification, etc.

Quantization noise is the noise generated by the signal quantization when converting from an analogue to a digital signal. By increasing the amount of bits representing the signal, this noise contribution is decreased.

2.4 Image Motion Effects

In the previous sections, imaging has been discussed both in a theoretical sense and as a practical implementation with the associated limitations. During this discussion a set of constraints was defined, which are summarized as being:

- Discrete photographic imaging, since the imager should easily interface to a computer back-end.
- Mono-chromatic imaging, since the techniques described in this work will not depend on, or gain from, the additional information in multi-spectral imaging.
- Low-light applications.

The fraction of the scene that can be imaged is determined by the focal length and the size of the imaging plane and is referred to as the field of view (FOV). Objects that are located outside the FOV will be projected outside the imaging plane. For the human vision, objects that are located outside the FOV can be brought inside the FOV simply by turning the head or moving the eyes. Similarly for an imaging system, the objects can be brought inside the FOV simply by rotating the imager. This implementation is frequently seen in the field of astronomy, where an imager (telescope) is mounted on a mechanical setup, that can be programmed to rotate in

one or more directions. The closed loop operation of such an imaging system together with an attitude sensor has been implemented [7] and will be discussed in §3.2.

Due to the low-light applications foreseen by the constraints, a relatively long integration time is required to establish an image with a reasonable S/N ratio. If the relative motion between the imager and a radiating point source causes the projection of the point source onto the imaging plane to be dispersed over more than one pixel, the image is referred to as being smeared. This phenomenon is usually highly undesired in imaging applications and will result in the effects described in this section.

2.4.1 Loss of effective resolution

The loss of effective resolution in the motion direction is a dominant effect, since the high frequency fine-structure of the image is attenuated (or even completely removed for certain frequencies) [10].

Consider a point source being projected on an image plane of a certain size. The radiation is focussed on the pixel $I_{i,j} = I_{m,n}$ through a perfect lens using a certain integration period T_{int}. The projection in the image plane will be a discrete 2-D delta-function $\delta(i, j)$. For simplicity, the intensity in the given pixel is 1. The intensity of the corresponding image pixels $b_{i,j}$ can now be described as:

$$b_{i,j} = \begin{cases} 1 & \text{if } (i,j) = (m,n) \\ 0 & \text{otherwise} \end{cases} \tag{2.10}$$

Consider now that the point source is immediately accelerated to a certain velocity parallel to the x-axis of the image plane. The velocity is chosen such that the projection of the point source is moved N pixels on the image. The corresponding image pixels will now be:

$$b_{i,j} = \begin{cases} 1/N & \text{if } i \in \{m, m-1, ..., m-N+1\} \wedge j = n \\ 0 & \text{otherwise} \end{cases} \tag{2.11}$$

In case no knowledge about the motion is available, the resolution will be unaltered along the y-axis, but reduced by a factor of N along the x-axis. It is not possible to determine at which position the point source was located.

If the motion characteristics can be established, the resolution can be partly restored by subsequent image processing.

2.4.2 Loss of high frequency image information

Consider an image being acquired of a moving target, such that the projected image is evenly smeared over N pixels along the image sensor y-axis. In addition, let the target contain spatial frequency components with a period of N. When the target is subjected to such image smearing, components of this particular frequency will be effectively removed from the image. In fact all frequency components with a period $N/k, k \in \mathbf{Z}*$ will be effectively removed from the image.

The modulation transfer function $H(u, v)$ originating from the N pixel smearing will, according to [10] be:

$$H(u, v) = \frac{\sin 2v/N}{2v/N} \tag{2.12}$$

where u and v are the frequency components along the x- and y-axis respectively. Since no motion is taking place along the x-axis, spatial frequencies along this axis u are modulated unattenuated. All spatial frequencies along the y-axis v, higher than 0, will be attenuated according to eq. 2.12.

2.4.3 Increased S/N ratio

Since the projection of the object will be dispersed over an increasing number of pixels, all noise components in the supported area will contribute to the noise measure.

Consider the main noise component in an imager to be noise induced by the read-out electronics. The noise in an acquired image is therefore close to white. That is, the noise in each pixel is independent of the neighbor pixels and has an intensity distribution that follows a Gaussian distribution with a standard deviation σ and a mean $\mu = 0$. The noise in each image pixel $b_{i,j}$ is denoted $\xi_{i,j}$. If noise is added to the image in eq. 2.10 the following noisy image is obtained:

$$b_{i,j} = \begin{cases} \xi_{i,j} + 1 & \text{if } (i, j) = (m, n) \\ \xi_{i,j} & \text{otherwise} \end{cases} \tag{2.13}$$

Accumulating the intensity over the region that received irradiation from the point source yields:

$$b_{object} = \sum_{i=m}^{m} \sum_{j=n}^{n} b_{i,j} = b_{m,n} = \xi_{m,n} + 1 \tag{2.14}$$

Since $\xi_{i,j}$ has a standard deviation of σ, the intensity of the point source is also measured with a standard deviation of σ.

On the other hand, if the noise is added to the image recorded at the point source in motion in eq. 2.11, the image will be:

$$b_{i,j} = \begin{cases} \xi_{i,j} + 1/N & \text{if } i \in \{m, m-1, ..., m-N+1\} \wedge j = n \\ \xi_{i,j} & \text{otherwise} \end{cases} \tag{2.15}$$

Accumulating the intensity over the region receiving irradiation yields:

$$b_{object} = \sum_{i=m-N+1}^{m} \sum_{j=n}^{n} b_{i,j} = \sum_{i=m-N+1}^{m} b_{i,n} = 1 + \sum_{i=m-N+1}^{m} \xi_{i,n} \tag{2.16}$$

where the first term is the irradiated pixel intensity (b) and the second term is the accumulated noise from the object support area.

The variance of a sum of N variables each having a variance $V = \sigma^2$ is the sum of the variances. The total standard deviation of the measured intensity σ_{total} is therefore:

$$\sigma_{total}^2 = \sum_{i=m-N+1}^{m} \sigma_{i,n}^2 = N\sigma^2 \Leftrightarrow \sigma_{total} = \sqrt{N}\sigma \tag{2.17}$$

i.e. if the support area increases N times in an uncorrelated system, the total noise is increased by $\sqrt{N}$ times as well. The S/N ratio is hereby decreased by $\sqrt{N}$.

2.4.4 Detectability

Since the intensity (e.g. from a point source) is smeared on several pixels, the recorded immediate intensity (in a single pixel) is being reduced (see eq. 2.15). This increases the complexity of a later detection of an object in the image, increasing the risk of wrongly detecting noise spikes instead of the true object projection.

Consider that the S/N ratio η is known for a given system. The signal intensity b will be coupled to the standard deviation of the system noise σ by the relation $\eta = b/\sigma$. The noise is again considered white. The signal density d is defined as the number of signal pixels divided be the total number of pixels. The density of background pixels will therefore be $1 - d$. The histogram of an image having a signal density $d = 0.2$ and $\eta = 10$ is given in figure 2.1. For simplicity, the intensity of the background has been set to $b = 0$, while the intensity of the object is set to $b = 1$. Even

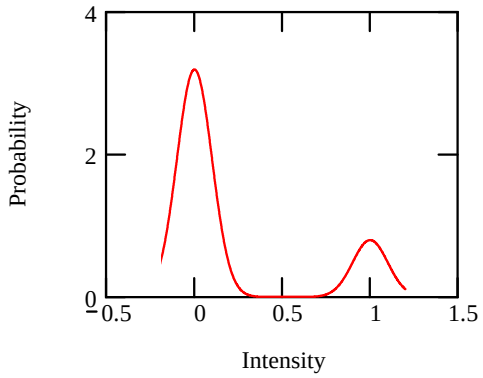

Figure 2.1: A typical image histogram showing the intensity probability density. The given image has $\eta = 10$, $d = 0.2$ and $b = 1$.

though negative intensities are not possible, they are included to illustrate the principle.

The histogram of an ideal image containing noise $H(b)$ is basically built from adding two Gaussian distributions

$$H(b) \approx \frac{1}{1/\eta\sqrt{2\pi}} \left\{ d \cdot e^{\frac{-(b-1)^2\eta^2}{2}} + (1-d) \cdot e^{\frac{-b^2\eta^2}{2}} \right\} \tag{2.18}$$

where the signal intensity has been normalized to $b = 1$, leading to the S/N ratio $\eta = 1/\sigma$. In eq. 2.18 the left term defines the signal, while the right term defines the background.

In this case the signal will be in the right top in figure 2.1, while the background will be at the left top. An obvious, well-defined and often applied classification of a pixel is to make a threshold at the local histogram minimums. These minimums are shown in a zoomed logarithmic plot in figure 2.2 for an image having $\eta = 10$ and signal densities $d = 0.5, 0.1, 0.01, 0.001$ and 0.0001.

If the S/N ratio is decreased, the minimum will be less well defined. This is illustrated in figure 2.3 for an image having $\eta = 5$ and the same signal densities as before.

It can be seen from the figure that the minima are less well defined. For the signal $d = 0.0001$ image the minimum is non-existent, wherefore the proposed thresholding is no longer well defined. To draw a conclusion, systems based on automatic thresholding to classify pixels will suffer heavily with applications having a poor S/N ratio.

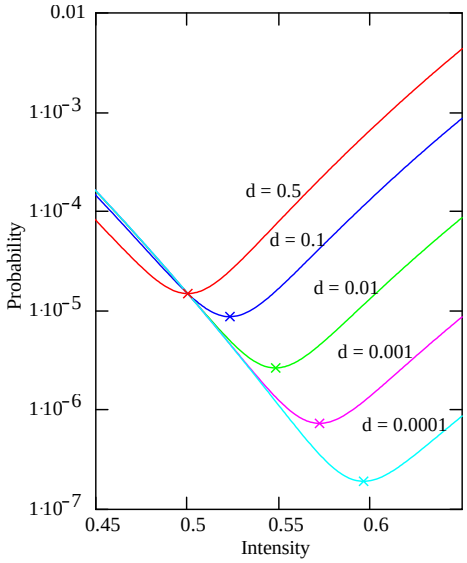

Figure 2.2: A zoom of the image histogram having $\eta = 10$ and $d = 0.5, 0.1, 0.01, 0.001$ and 0.0001. The minima are marked with $\times$'s.

Defining the local minimum to be the detection threshold, is not necessarily the optimal setting for a given application. That is, the inconvenience of wrongly detecting noise as a signal is not necessarily equal to the inconvenience of wrongly detecting signal as noise. A cost function based on the associated impacts can advantageously be included in the threshold determination function [10].

It is found from the analysis above that the signal detectability is heavily aggravated by the lower S/N ratio induced by image motion.

2.4.5 Classification

Independent of the threshold strategy, a certain rate of pixels being wrongly classified will exist. This rate E is again heavily dependent on the S/N ratio η and can be calculated from:

$$E = \int_{-\infty}^{thres} d \cdot e^{\frac{-(x-1)^2\eta^2}{2}} dx + \int_{thres}^{\infty} (1-d) \cdot e^{\frac{-x^2\eta^2}{2}} dx \qquad (2.19)$$

where the $thres$ is the threshold value, e.g. found at the histogram minimum described in the previous section. The first term in eq. 2.19 is the rate of

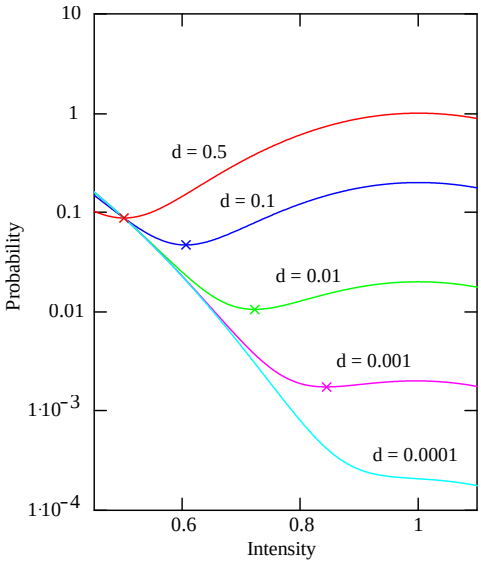

Figure 2.3: A zoom of the image histogram having $\eta = 5$ and $d = 0.5, 0.1, 0.01, 0.001$ and 0.0001. The minima are marked with x's.

signal pixels being determined as background pixels, while the second term is vice versa. The rate of mis-classifications for a signal density $d = 0.1$ as a function of the S/N ratio η is given in figure 2.4.

The classification thresholds applied in figure 2.4 have been put at the histogram minima. It is found from the figure that the classification of pixels suffers heavily from poor S/N ratios.

The theory described has been based on one object of a constant intensity $b = 1$ (normalized to 1) being classified on a background having 0 intensity. For practical applications, the intensity will rarely be constant. In the histogram, the affected top will open up and no longer have a Gaussian shape.

Additionally, several objects may appear in the image simultaneously. Having different intensities they will individually appear in the histogram. The theory behind detection and classification of several image objects is analogous to the theory described here for one object.

Consider again that the object is moved relative to the image plane during image integration in such a way, that the image projection is moved N bytes along the x-axis. It follows from eq. 2.11 that the signal intensity b for a given irradiated pixel will decrease to b/N. The S/N ratio η will

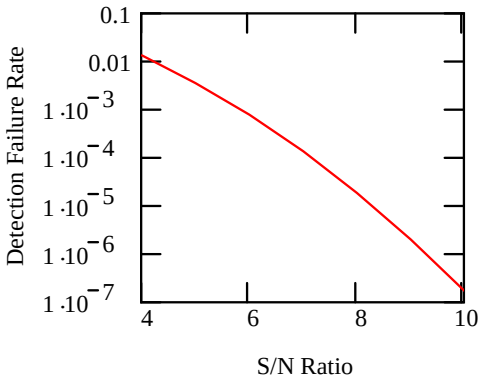

Figure 2.4: The relationship between the rate of mis-classification and the S/N ratio for a signal density $d = 0.1$.

therefore also drop to η/N. It appears from figure 2.4 that this effect is highly undesirable.

2.4.6 Limitations on achievable S/N ratio

In order to enable an accurate object centroiding (i.e. measuring the position and intensity on the focal plane), the image acquisition must yield a certain S/N ratio for the integral object. Since the object to be imaged is moving through the imager field of view (or since the projection is moving across the imaging plane), the object will only be subject to imaging in a limited amount of time. This effect enables the risk that the required S/N ratio cannot be obtained from the irradiated number of photons.

Consider an imaging system having a S/N ratio η_0 at a given integration time T_{int} when the object is at rest. Consider now, that the object is in motion relative to the image plane, such that the projection is moving with a velocity of $\upsilon = 1/T_{pix}$ measured in [pixels/s]. T_{pix} is therefore the time spent for the projection to move one pixel. The effective S/N ratio η is therefore according to eq. 2.17 and using that $\eta = b/\sigma$, b being the signal intensity:

$$\eta = \frac{\eta_0}{\sqrt{N_{pix}}} = \frac{\eta_0}{\sqrt{\left\lceil \frac{T_{int}}{T_{pix}} \right\rceil}} \tag{2.20}$$

where the ceiling operators $\lceil$ and $\rceil$ of a real variable r returns the closest

integer $i > r$ such that $i - r \in]0; 1]$. For a given application, an S/N ratio of $\eta', \eta' > \eta$ is required. To obtain this, the required integration time T'_{int} must be:

$$T'_{int} = T_{int}\frac{\eta'}{\eta} = T_{int}\frac{\eta'}{\eta_0}\sqrt{N_{pix}} \tag{2.21}$$

where the noise is considered independent of the integration period. The dark current noise is considered low compared to following noise components. The total time that the image projection is available at the image plane is constrained by the number of pixels N_{total} along the axis of motion. The maximum integration time T_{total} can be determined from

$$T_{total} = N_{total}T_{pix} \tag{2.22}$$

In case $T'_{int} > T_{total}$, it is not possible with the current setup to obtain the requested S/N ratio.

2.5 Motion Regimes

Consider an object to be imaged that has a certain extent (i.e. it is not a point source). On this object a certain number of unique areas is defined, being corners, discrete changes in illumination levels, etc. Such unique areas are referred to as tokens. If the system is at rest, any subsequent image will contain the same tokens at the same locations.

One example is the image of a satellite. The satellite will be the object, whereas corners on the body and the solar panels could be tokens. Another example is from the star-tracker application, where the object is the night sky and the stars will be the tokens.

In order to correctly detect, compensate and/or process a motion in an image projection, a characterization of the motion must be established. The following list describes features that, when applicable, can be used in the characterization process:

Conservation of intensity The integral projected intensity of an imaged object or of distinct isolated object areas is maintained.

Conservation of geometry The geometry between all tokens within the object are maintained (possibly after a geometric reconstruction).

Aliasing Correct identification of motion is dependent on the sampling frequency. In case the revolution time is smaller than two times the imaging interval aliasing will occur (according to Nyquist).

In the following section, different motion types will be identified. Since a motion of an object is always relative to some frame, the following duality is existing: Is the object spinning around the imager or is the object position fixed while the imager itself is in a rotating state? In order to remove this duality it is defined that all object motion is described in the coordinate frame of the camera.

2.5.1 Translation

The simplest form of motion is when the object moves within the reference frame defined by the imager and the orientation within this frame is maintained. The object is considered to be rigid, i.e. the geometry of the object itself is constant (see figure 2.5).

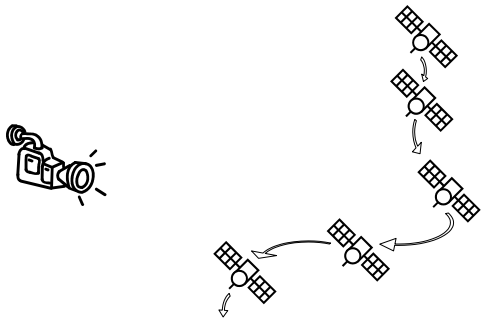

Figure 2.5: In the translation motion regime, the object moves within the reference frame having a fixed orientation.

This motion category translates into a simple object translation on the image projection. If the object position projected onto the optical axis is *not* constant (the object motion is not within a plane parallel to the imager plane), the projected scale will vary. The token geometry is hereby not conserved.

Let the object be moving in front of the imager in a plane parallel to the image plane. As the object approach the optical axis, faces pointing in the motion direction will be visible. Since the object is *not* rotating about it's own axis, when the object retreat from the optical, this face will be occluded by the object itself. Analogue observations can be derived for the face pointing opposite the motion direction. Tokens located on these surfaces will not be present in the image projection during the entire motion, wherefore object geometry is not guaranteed to be conserved for this subclass

of translation.

Since the distance between the object and the imager is not guaranteed to remain constant and a Lamberdian radiation is considered, the intensity will decrease with distance (the intensity decreases with the square of the distance). This class of motion will therefore not satisfy the conservation of intensity characteristic.

Unless multiple objects having the same geometry constitutes the motion (e.g. items in a production on a conveyer belt), there is no risk of aliasing associated with this class of motion.

A typical application of planar translation is the motion of products on an assembly line.

2.5.2 Rotation

For this type of motion, the position of the object in the imager reference frame is held constant, whereas the orientation is constantly changing (see figure 2.6).

Figure 2.6: In the rotation motion regime, the object position is fixed while the orientation is varying.

Since the faces of the object is not guarantied to radiate the same intensity and different faces will be pointed towards the imager, the intensity is not conserved. Unless the optical axis is co-aligned with the rotation axis, the token geometry is broken by the same argument. Finally, aliasing may occur.

2.5.3 Spherical Translation

This type of motion is generated from a combination of the translation and the rotation regimes. The object is moving at a constant distance and constantly having the same face towards the imager. The possible positions are therefore on a sphere having the imager in the center, such that the trace of the object on the sphere is a smaller or greater circle. The object is again considered to be stiff (see figure 2.7).

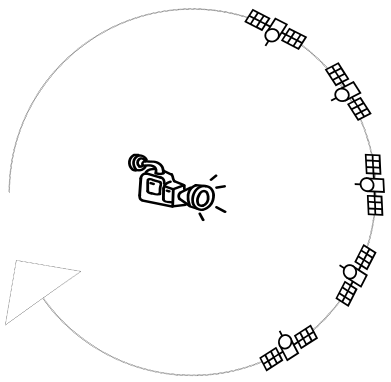

Figure 2.7: In the spherical translation motion regime, the object moves on a sphere centered in the imager lens, posing the same face towards the imager at all times.

For the spherical translation, the intensity will almost be conserved (for small FOVs). Since the angular distance between the optical axis and the object is not constant, the size of the apparent lens aperture as seen from the object will change slightly due to changing perspectives. Secondly, vignetting will cause an intensity drop-off for large photon incident angles. On the other hand, the geometry will be conserved (after a geometric reconstruction). Aliasing can occur, if the revolution time of the object is smaller than twice the imaging interval. One example of such motion is the revolution of the Moon around the Earth (as well as the Earth's rotation). The Moon has the same face towards the Earth at all times.

2.5.4 Flow

For the flow motion, the tokens within the object will move in separate independent directions. The motion of flies within a swarm is an example of a flow motion. The motion of the individual fly is (apparently) independent of the surrounding flies (figure 2.8).

The motion of the leaves falling from the trees during the fall is an example of flow motion field combined with a planar translation. The wind and the Earth gravity will cause the leaves to be moving in a common direction, constituting the planar translation, while the small differences in the leaf geometry, position relative to the wind, etc. will cause a chaotic motion of the leaves relative to each other.

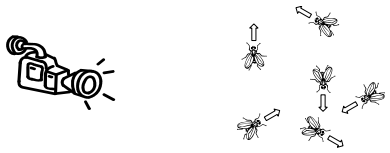

Figure 2.8: In the flow motion regime, the tokens (objects) move in separate directions independently of each other.

For the flow motion, neither the intensity nor the token geometry will be conserved. On the other hand, since the motions of the tokens are independent the risk of aliasing is non-existent.

2.5.5 Source and Drain

The final type of image motion that will be treated here is the source and drain type. For this type of motion, tokens will appear and tokens will disappear. The intensity of the individual tokens will not be conserved (since they tend to disappear), neither is geometry. There is, however, no risk of aliasing.

Once again, this class of motion is (usually) highly dependent on the imaging frequency. One exception is the effects from transient hotspots in CCD's, which are further described in §3.4.

2.5.6 Motion Regime Summary

The different motion regimes with the associated characteristics discussed in this section are summarized in table 2.1. These characteristics are all global measures. For small motions, yielding local measures, several of the characteristics are maintained.

The motion of the stars (and galaxies) on the night sky implements several of the motions regimes described:

- In a short time frame (seconds-hours), the rotation of the Earth will cause an apparent spherical translation of the stars. The geometry between the tokens is unaltered.
- In a longer time frame (years), the proper motion of the stars generate a (well defined) change in the token geometry, such that the motion translates into a flow regime field.

Table 2.1: Characteristics of different flow regimes.

Motion regime	Intensity cons.	Geometry cons.	Alias free
Translation	No	No[1]	Yes
Rotation	No	No[1]	No
Spherical trans.	Yes	Yes	No
Flow	No	No	Yes
Source and drain	No	No	Yes

1) The geometry will be conserved for certain configurations

- In an even longer time frame (millions of years), the forming of new stars and annihilation of stars will implement a source and drain scenario on top of the previous identified regimes.

It is apparent from the example above, that the motion regime considered must be related to a well defined observation interval.

2.6 Attitude Representations

The 3-axis orientation of an object or a rigid system within a given reference frame can be described in a number of ways. The purpose of this section is to give a brief introduction to 3 different representations for completeness. For further reading please refer to e.g. [24].

Let the reference coordinate frame be a 3 dimensional orthonormal[3] right-handed reference frame R, defined by the three unit vectors $\bar{x}$, $\bar{y}$ and $\bar{z}$. In addition, let the coordinate frame of the object O be defined by the three unit vectors $\bar{u}$, $\bar{v}$ and $\bar{w}$.

2.6.1 Euler Angles

The orientation of the object O can be described as a sequence of three rotations about the axis defining R. The three rotations will bring the axis defining R parallel to the axis defining O. Since the first rotation of R will change the reference axes, the order of rotations must be maintained.

Within astronomy, a zyz representation is often applied, such that the orientation is defined by the three angles α, δ and θ. First a rotation of α

[3]Orthonormal frame: The N vectors defining the N-dimensional frame are individually orthogonal *and* unit vectors

is performed about the z-axis, then a rotation of δ is performed about the new y-axis and finally a rotation of θ is performed about the new z-axis.

2.6.2 Direction Matrix

The three columns in a 3×3 matrix $\bar{\bar{M}}$ represents the directions of the three axes of an object in the absolute reference frame R. If R is an orthonormal frame the attitude matrices will be orthogonal.

$\bar{\bar{M}}$ can be used as a coordinate transfer matrix, such that vectors defined in the object can easily be converted into the absolute reference frame (and vice verca) by linear operations.

2.6.3 Quaternion

It can be shown, that all possible 3-axis orientations can be achieved by rotating the reference frame a certain angle ω about a certain rotation vector $\Omega = [\Omega_x \Omega_y \Omega_z]^T$, $|\Omega| = 1$. A quaternion is a four-row vector, which basically contains the three components of Ω plus ω. A quaternion $\bar{Q}$ describing the attitude defined by a rotation of ω about Ω is:

$$\bar{Q} = \begin{bmatrix} \Omega_x \sin\frac{\omega}{2} \\ \Omega_y \sin\frac{\omega}{2} \\ \Omega_z \sin\frac{\omega}{2} \\ \cos\frac{\omega}{2} \end{bmatrix} \tag{2.23}$$

such that $|\bar{Q}| = 1$.

2.7 Motion Characterization

Consider the image acquisition of a series of images being controlled according to the flowchart in figure 2.9.

If the post processing step is omitted the flowchart is reduced to a simple closed loop control. Image I_n is recorded using the motion characteristics found in Image I_{n-1}. I_n is input to the motion characterization that determines the motion characteristics present in this image, for which a motion model is updated. The motion in the following image I_{n+1} is extrapolated from the model to be used as feedback to the following I_{n+1} integration.

If the feedback loop is omitted, the motion compensation must rely on a priori knowledge only, turning the system into a simple open loop control. The image is again passed to the motion characterization block to determine the proper input to a post processing block.

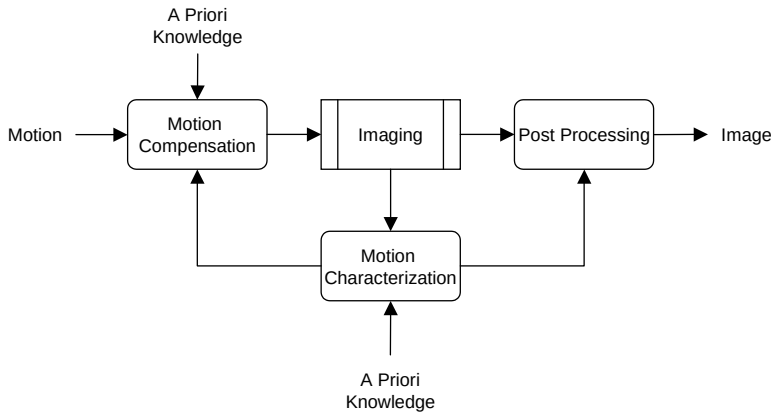

Figure 2.9: Flowchart describing the different steps required for motion compensation control, and how they interact.

Each of the process blocks: Motion characterization and motion compensation are treated individually in this and the following section. Post-processing is highly application dependent and will not be treated further.

Motion characterization covers the task of detecting and characterizing the motion in an image or in an image sequence. Unless a priori knowledge about the exact motion exists, this characterization is a prerequisite for correct compensation and/or post processing.

2.7.1 Image Transformation

Depending on the imaging application, a transformation of the image into an appropriate format may be necessary. Examples of such transformations include:

- High pass filtering and edge enhancement used to accentuate tokens [10]
- Down-sampling to lower resolutions for a faster processing of larger-scale objects (see e.g. [19])
- Image subtraction to emphasize image tokens.

Especially for uncompensated systems, a dominant motion may cause the S/N ratio to be insufficient to correctly detect the image tokens. It was

demonstrated in §2.4.5 that a motion of N pixels during integration caused a drop in detectability of N as well.

Consider a point source in planar motion with velocity υ (measured in pixels/integration) being imaged through a perfect lens. The acquired image I contains the image pixels $b_{i,j}$. The motion direction and the velocity are considered unknown, whereas the effective S/N ratio is $\eta_{eff} = \eta/\upsilon$. In order to increase the detectability, a down-sampling of the image is performed such that $N \times N$ neighbor pixels are combined (binned), yielding the image $I\prime$ (containing the image pixels $b'_{i,j}$:

$$b'_{i,j} = \sum_{m=1}^{N} \sum_{n=1}^{N} b_{Ni+m,Nj+n} \tag{2.24}$$

Since the projection is following a linear, non-accelerated path, the signal will be multiplied by N. Simultaneously, the noise will increase by the squareroot of the supported area. The new effective S/N ratio η'_{eff} becomes:

$$\eta'_{eff} = \eta_{eff} \frac{N}{\sqrt{N^2}} = \eta_{eff} \tag{2.25}$$

from which it is apparent that the S/N ratio (of a point-source originating from a perfect lens) cannot be increased by binning.

In case the imaged object is not a point source but has an extent in the projection orthogonal to the motion direction, the binning will have some effect. Similarly, if the velocity direction is known, binning along this line of motion alone will increase η'_{eff}.

In the following sections image transformation will not be considered or treated further. It is presumed that the image is in such a state, that the objects and tokens can be recovered.

It is also presumed that the motion in question implements a spherical translation, defined by having the position of the objects fixed and having the imager rotating with a constant angular velocity. As observed from the imager, the objects will be rotating around a fixed rotation axis Ω, $|\Omega| = 1$ with a fixed angular velocity $\dot{\omega}$ (see Figure 2.10).

The objective of the image characterization is therefore to establish Ω and ω based on one image or an image sequence.

It is often more convenient to represent the position of the object as a vector from the lens center (origo) to the object. This vector $\bar{p}$ can be formed from the image projection $(x, y) = (x_1, y_1)$ and the focal length f as:

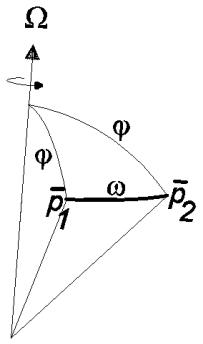

Figure 2.10: Sketch of a simple motion of ω about the rotation vector Ω taking the object from position (direction) $\bar{p}_1$ to $\bar{p}_2$

$$\bar{p} = \frac{\begin{bmatrix} -x_1 \\ -y_1 \\ f \end{bmatrix}}{\sqrt{x_1^2 + y_1^2 + f^2}} \tag{2.26}$$

where the denominator is inserted for normalization of the vector. This representation will be used unless otherwise specified.

2.7.2 Change in Morphology

This type of motion characterization is based on analysis of a single image. The object in question is considered to be a point source, recorded during the integration time T_{int}. At time $t = 0$ the object will be projected in $(x, y) = (x_1, y_1)$, whereas at time $t = T_{int}$ the object will be projected in $(x, y) = (x_2, y_2)$. It is presumed that the object revolution time is smaller than the integration time, such that the trace will form an arc or a line.

However, the same trace will appear if the object is located at $(x, y) = (x_2, y_2)$ at $t = 0$ and in $(x, y) = (x_1, y_1)$ at $t = T_{int}$ rotating in the opposite direction. *It is therefore not possible to establish whether the object rotates clockwise or anti-clockwise based on one image.*

Arc Detection

Since the object is rotating about Ω, the angle between Ω and the object vector will be constant by definition (see e.g. figure 2.10).

Consider three arbitrary points $\bar{p}_1$, $\bar{p}_2$ and $\bar{p}_3$, $\bar{p}_1 \neq \bar{p}_2 \neq \bar{p}_3$, located on the trace of the object. The angle between Ω and $\bar{p}_1$ will be equal to the angle between Ω and $\bar{p}_2$, or

$$\Omega \cdot \bar{p}_1 = \Omega \cdot \bar{p}_2 \tag{2.27}$$

which is one equation with 3 unknown variables $(\Omega_x, \Omega_y, \Omega_z)$. Since the same is valid for $\bar{p}_2$ and $\bar{p}_3$ and taking advantage of $|\Omega| = 1$ yields:

$$\begin{aligned} \Omega \cdot \bar{p}_1 &= \Omega \cdot \bar{p}_2 \\ \Omega \cdot \bar{p}_2 &= \Omega \cdot \bar{p}_3 \\ |\Omega| &= 1 \end{aligned} \tag{2.28}$$

resulting in three equations with 3 unknown variables which can be solved numerically.

Unfortunately, the three equations given in 2.28 do not form a linear system. One mean to generate a linear system is to fix one of the components of Ω, e.g. setting $\Omega_x = 1$ and perform the normalization of Ω after solutions of Ω_y and Ω_z have been found. This approach will unfortunately introduce a singularity for Ω being located in the y-z plane ($\Omega_x = 0$). In case of small angular velocities $\dot{\omega}$ relative to T_{int}, the geometry between $\bar{p}_1$, $\bar{p}_2$ and $\bar{p}_3$ will be poor, leading to a poor determination of Ω.

Alternatively a geometric approach can be applied: From the vectors $\bar{p}_1$ and $\bar{p}_2$ a plane of possible rotation vectors P_1 can be determined. This plane will contain the cross product between $\bar{p}_1$ and $\bar{p}_2$ denoted $\bar{v}_1$, corresponding to Ω being orthogonal to $\bar{p}_1$ and $\bar{p}_2$. It will also contain the sum of $\bar{p}_1$ and $\bar{p}_2$ denoted $\bar{v}_2$, corresponding to Ω being located at the middle of the trace. The scenario is sketched on figure 2.11.

The normal vector to P_1, $\bar{n}_1$, can now be determined as the cross product of $\bar{v_1}$ and $\bar{v_2}$, i.e.

$$\bar{n}_1 = \bar{v}_1 \times \bar{v}_2 = (\bar{p}_1 \times \bar{p}_2) \times (\bar{p}_1 + \bar{p}_2) \tag{2.29}$$

Similarly, combining $\bar{p}_2$ and $\bar{p}_3$ yields:

$$\bar{n}_2 = \bar{v}_2 \times \bar{v}_3 = (\bar{p}_2 \times \bar{p}_3) \times (\bar{p}_2 + \bar{p}_3) \tag{2.30}$$

Since Ω is present in both P_1 and P_2, and $P_1 \neq P_2$, Ω must be the intersection between the two planes, or

$$\Omega = \frac{\bar{n}_1 \times \bar{n}_2}{|\bar{n}_1 \times \bar{n}_2|} \tag{2.31}$$

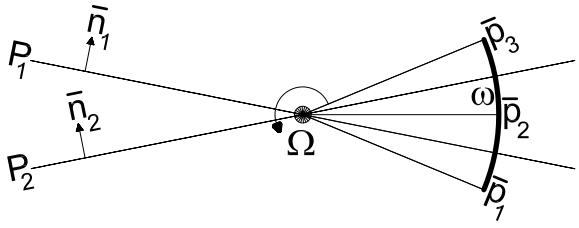

Figure 2.11: Motion characterization from "arc detection". Projection on the rotation plane showing the three measured trace positions $\bar{p}_1$, $\bar{p}_2$ and $\bar{p}_3$. The positions are used to define the two planes P_1 and P_2, that intersect at the rotation vector Ω

where the denominator is inserted for normalization. Additional trace points can be included, such that a hyper-accuracy solution can be formed from an averaging using a suitable weighting of the Ω's determined.

Finally, the size of the rotation ω can be found from Ω and the two end points of the trace denoted $\bar{p}_a$ and $\bar{p}_b$. The normal vector to the plane containing Ω and $\bar{p}_a$ is $\bar{n}_a$, while the normal vector to the plane containing Ω and $\bar{p}_b$ is $\bar{n}_b$. ω can be determined as the angle between $\bar{n}_a$ and $\bar{n}_b$, i.e.

$$\cos(\omega) = \frac{\bar{n}_a}{|\bar{n}_a|} \cdot \frac{\bar{n}_b}{|\bar{n}_b|} = \frac{p_a \times \Omega}{|p_a \times \Omega|} \cdot \frac{p_b \times \Omega}{|p_b \times \Omega|} \tag{2.32}$$

As mentioned previously, it is unknown whether $\bar{p}(0) = \bar{p}_a$ and $\bar{p}(T_{int}) = \bar{p}_b$ or vice versa. Unfortunately this approach leads to a singularity as well for $\bar{n}_1 \times \bar{n}_2 \to 0$ (i.e. the geometry between $\bar{p}_1$, $\bar{p}_2$ and $\bar{p}_3$ is being poor).

The procedure described in this section has been constrained to the trace of one point source object. If several objects are present in the scene, a higher accuracy solution of both Ω and ω can be formed from e.g. a least-square fit.

2.7.3 Feature Recognition

Consider an object in motion and two images I_1 and I_2 being sequentially recorded. The objective is to find the rotation vector Ω and the rotation velocity $\dot{\omega}$ based on information retrieved from the two images. This information can exist in several forms and is highly application dependent. It is presumed that a number of image tokens can be extracted from the images. These image tokens given as unit vectors will be denoted $\bar{\tau}_i, i \in 0..N_{total} - 1$, where N_{total} is the number of tokens in an image.

To each image token, a predetermined set of characteristics is derived, referred to as features. The union of features belonging to a token is referred to as a feature vector [10]. The definition of the exact feature is application dependent, and may include (to mention a few): Integral intensity, shape, orientation and position, but also far more abstract measures can be included.

Since this work concentrates on image motion, the images applied to feature recognition may contain a dominant amount of image smear. Since the motion characteristics are unknown at this point, the smear cannot be compensated for in order to restore the original image objects. The features selected for the recognition (the feature vector) must therefore be independent of the smear, excluding shape and orientation from the features listed above.

The token position could be calculated from the center of mass, which is a rotational symmetric, invariant measure. The motion of the center of mass will be described by the motion of the image. However, since a motion is expected to take place between the image recordings, the position will change (if $\bar{\tau}_i \neq \Omega$).

Since the work described here is confined to a spherical translation, the characteristics of this motion regime can be reinvoked. According to table 2.1, the integral intensity will almost be conserved, the geometry between tokens is fully conserved, while there is a risk of aliasing.

The integral intensity can be found from integration of pixel values inside the contour of the token. It should be noted, that if the image motion is considerably high, the support area contained by the contour will also be large, effectively decreasing the S/N ratio (§2.4.3). This must be taken into account in the recognition process.

The conservation of token geometry characteristic can be applied by including the image "neighborhood" in the feature vector. The closest token $\bar{\tau}_1$ to a given token $\bar{\tau}_0$ in I_1 will also be the closest token in I_2. Since the intensity of all tokens will be approximately conserved, a feature could be the intensity either of the closest token or the N closest tokens ($N \leq N_{total} - 1$). Unfortunately, one of the effects of image motion is that tokens may move outside the imager field of view. It is therefore not guaranteed that the complete list of closest token intensities in I_1 is available in I_2, which must be taken into consideration during the recognition process.

As mentioned previously, the absolute token positions are not conserved but their positions relative to each other will be conserved (conservation of

geometry). Since the image is a projection of a motion on a sphere, the token geometry will be distorted when approaching the image border. Therefore the vector from the lens center to the token in object space should be used instead of the image position (see §2.7.1). The angles between the token vectors will remain constant, wherefore the angles to the N closest tokens $\phi_{0,j}, j \in \{1..N\}$ can be included in the feature vector.

Also the mutual angles between neighbor tokens can be included in the feature vector. The neighbor tokens can be numbered according to their distance to the token in question $\bar{\tau}_0$ such that:

$$\bar{\tau}_0 \cdot \bar{\tau}_i > \bar{\tau}_0 \cdot \bar{\tau}_j \Leftrightarrow i < j \qquad i, j \in \{1..N\} \tag{2.33}$$

In addition, all mutual angle combinations,

$$\phi_{i,j} = \arccos(\bar{\tau}_i \cdot \bar{\tau}_j) \qquad i, j \in \{1..N\}, i \neq j \tag{2.34}$$

leading to $N(N-1)/2$ separate angles could be included in the feature vector.

The azimuth angle θ_j of the neighbor tokens will also provide information that is conserved after an image motion. This azimuth angle can be determined from a projection of all $\bar{\tau}_j, j \in \{1..N\}$ onto the plane defined by the normal vector $\bar{\tau}_0$ followed by a normalization. The projections of $\bar{\tau}_j$ will be denoted $\bar{\tau}'_j$. This can be performed by:

$$\bar{\tau}'_j = \frac{\bar{\tau}_0 \times (\bar{\tau}_j \times \bar{\tau}_0)}{|\bar{\tau}_0 \times (\bar{\tau}_j \times \bar{\tau}_0)|} \qquad j \in \{1..N\} \tag{2.35}$$

One problem is, that there is no fixed origin for the azimuth frame. Lee [17] proposes that the closest neighbor $\bar{\tau}_1$ is used to define the azimuth frame, such that $\theta_1 = 0$. Cosine to the azimuth angle θ_j can now be found from:

$$\cos\theta_j = \bar{\tau}'_1 \cdot \bar{\tau}'_j \qquad j \in \{2..N\} \tag{2.36}$$

Similarly, the sine of θ_j can be derived from:

$$\sin\theta_j = |\bar{\tau}'_1 \times \bar{\tau}'_j| \qquad j \in \{2..N\} \tag{2.37}$$

The full $\theta_j \in [0..2\pi[, j \in \{1..N\}$ can now be found from $sin(\theta_j)$ and $cos(\theta_j)$. Setting $j = 1$ will yield:

$$\begin{array}{rrl} \cos\theta_1 = & \bar{\tau}'_1 \cdot \bar{\tau}'_1 & = 1 \\ \sin\theta_1 = & |\bar{\tau}'_1 \times \bar{\tau}'_1| & = 0 \end{array} \tag{2.38}$$

which is true for $\theta_1 = 0$ as expected.

Considering the selected type of motion regime, features that are meaningful to include in the feature vectors include:

- intensity of the token
- intensity of the N closest neighbor token
- angular distance to the N closest neighbor tokens
- angular distance between the N closest neighbor tokens
- azimuth position of the $(N-1)$ closest neighbor tokens

Since the objective is to find the image motion between I_1 and I_2 all tokens in the two images $\tau_{img,i}$ are assigned a feature vector $T_{img,i}$. The number of tokens in image I_{img} will be denoted $N_{img,total}$. The feature vectors denoted $T_{img,i}$ where img denotes the source image and i is an arbitrary enumeration. Each of the token feature vectors from I_1, $T_{1,i}$ are compared to all the token feature vectors from I_2, $T_{2,j}$ in order to find the best matches. A match $M_{m,n}$ is found for all $m \in \{1..N_{1,total}\}$ if possible, such that:

$$[\text{dist}\,(T_{1,m}, T_{2,n}) \leq \text{dist}\,(T_{1,m}, T_{2,j})] \wedge [\text{dist}\,(T_{1,m}, T_{2,n}) < \epsilon] \qquad j \in \{1..N_{2,total}\} \tag{2.39}$$

where $\text{dist}\,(T_1, T_2)$ is a penalty function determining the distance between two feature vectors. ϵ is inserted to include a maximum allowed distance between two feature vectors (used for outlier rejection). This distance measure will not be treated further here. The matching process results in a list of corresponding token pairs L. The matching results can be refined e.g. by repeating the matching in the opposite direction, i.e.

$$[\text{dist}\,(T_{1,m}, T_{2,n}) \leq \text{dist}\,(T_{1,i}, T_{2,n})] \wedge [\text{dist}\,(T_{1,m}, T_{2,n}) < \epsilon] \qquad i \in \{1..N_{1,total}\} \tag{2.40}$$

For each pair in the list L, $M_{i,j}$ it is known, that the rotation ω about the rotation vector Ω moves the token $\bar{\tau}_{1,i}$ to $\bar{\tau}_{2,j}$. Ω can be derived by adopting that the angle to Ω will be equal for two matching tokens

$$\Omega \cdot \bar{\tau}_{1,i} = \Omega \cdot \bar{\tau}_{2,j} \qquad M_{i,j} \in L \tag{2.41}$$

Including two matching token pairs $M_{i1,j1}$ and $M_{i2,j2}$ and the requirement of Ω being normalized yields (analogous to eq. 2.28):

$$\begin{aligned} \Omega \cdot \bar{\tau_{1,i1}} &= \Omega \cdot \bar{\tau_{2,j1}} \\ \Omega \cdot \bar{\tau_{1,i2}} &= \Omega \cdot \bar{\tau_{2,j2}} \\ |\Omega| &= 1 \end{aligned} \tag{2.42}$$

Alternatively, Ω can be retrieved geometrically analogous to eq. 2.29 through 2.31

When Ω is resolved, the solution of ω can be found according to eq. 2.32 by replacing $\bar{p}_s$ with $\bar{\tau}_{1,i}$ and by replacing $\bar{p}_e$ with $\bar{\tau}_{2,j}$, such that

$$\cos(\omega) = \frac{(\bar{\tau}_{1,i} \times \Omega) \cdot (\bar{\tau}_{2,j} \times \Omega)}{|\bar{\tau}_{1,i} \times \Omega||\bar{\tau}_{2,j} \times \Omega|} \tag{2.43}$$

where the normality of $\bar{\tau}$ has been taken into account. Since the temporal order of the two images is known, the sign of $\dot{\omega}$ can be recovered from the relation:

$$\sin \omega = \frac{|(\bar{\tau}_{1,i} \times \Omega) \times (\bar{\tau}_{2,j} \times \Omega)|}{|\bar{\tau}_{1,i} \times \Omega||\bar{\tau}_{2,j} \times \Omega|} \tag{2.44}$$

2.7.4 Attitude Sensing

An alternative technique for motion characterization is to import information from a secondary instrument, providing information about the present attitude. Consider the attitude being available at time $T = t_1$ and $T = t_2$, denoted $\bar{\bar{A}}_1$ and $\bar{\bar{A}}_2$ respectively. The attitudes are given in the form of 3×3 matrices, often referred to as direction cosine matrices ([24] or §2.6.2). Each matrix represents a basis for the current reference frame in the absolute reference frame R.

The motion to be established is the 3-axis rotation required to rotate $\bar{\bar{A}}_1$ to $\bar{\bar{A}}_2$, denoted $\bar{\bar{V}}_{1,2}$. This rotation can be found from a simple matrix multiplication:

$$\bar{\bar{V}}_{1,2} = \bar{\bar{A}}_1^{-1} \bar{\bar{A}}_2 = \bar{\bar{A}}_1^T \bar{\bar{A}}_2 \tag{2.45}$$

taking advantage of the property of $\bar{\bar{A}}^T = \bar{\bar{A}}^{-1}$ for an orthogonal matrix $\bar{\bar{A}}$ (e.g. [8]).

An implementation of such motion characterization has been performed and is described further in §3.3.

2.8 Motion Compensation

The motion of an imaged object relative to the camera system is for most applications a disadvantage caused by either system requirements or external effects that cannot be directly controlled. One logical approach is to verify whether it is possible to either de-spin the object to be imaged or de-spin the imager, such that no motion is taking place.

Throughout the previous section, different techniques to characterize this undesired motion were discussed. This section will discuss various alternative techniques to compensate for the motion taking the output from the motion characterization process as input. All compensation methods described are related to the spherical translation motion regime.

2.8.1 Folding Mirror

The basic problem associated with motion smearing is that the apparent direction of the photons radiated from an object is changing during the image integration. An apparent solution to this problem is to change the direction of the photons during the image integration in order to counteract for the motion, such that the apparent direction of the photons (as seen from the imager) is constant.

This change in direction can be performed before the photons enter the lens by placing a mirror in front of the lens as illustrated in figure 2.12. The mirror can be rotated about one or two axis depending on the motion complexity.

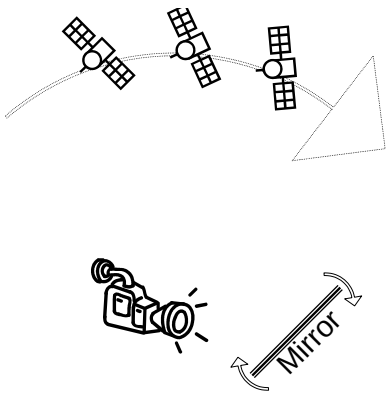

Figure 2.12: An application using a folding mirror in front of the lens to compensate for the object motion.

The irradiated photons will be mirrored in the image according to the local mirror surface normal. It is a strict requirement that the mirror is of a high optical quality. Otherwise image blurring will be introduced effectively reducing the S/N ratio.

Consider that the reference frame being orthonormal and right-handed, defined by the imager plane x-axis, y-axis and the optical axis, being the

x, y and z axis respectively. The y-axis direction is selected such that a right-handed frame is realized, and the frame origin is located in the lens center. An object (token) is moving from $\bar{p}(0)$ to $\bar{p}(T_{int})$ during the period $t \in [0..T_{int}]$, where $\bar{p}(t)$ is given as a normalized vector from the origin to the object position at time t. $\bar{p}(t)$ is extrapolated from a motion model established by a preceding motion characterization.

According to [23] the vector $\bar{s}$ mirrored in the normalized mirror surface normal $\bar{n}$ yields a new vector $\bar{s}_1$ given by:

$$\bar{s}_1 = \bar{s} - 2\bar{n}(\bar{s} \cdot \bar{n}) \tag{2.46}$$

Since the mirror surface normal is assumed to be well known in the given reference frame, the vector to the object acquired through the mirror $\bar{p}'(t)$ is:

$$\bar{p}'(t) = \bar{p}(t) - 2\bar{n}(t)(\bar{p}(t) \cdot \bar{n}(t)) \tag{2.47}$$

where $\bar{n}(t)$ is the mirror normal at time t and $\bar{p}(t)$ is given by the true object position. In order to correctly track the object, $\bar{p}'(t)$ must be held constant during the integration:

$$\bar{p}'(t) = \bar{p}'(0) \qquad 0 < t < T_{int} \tag{2.48}$$

Solving eq. 2.47 for the required surface normal $\bar{n}(t)$ and applying eq. 2.48 yields:

$$\bar{n}(t)\left\{2\bar{p}(t) \cdot \bar{n}(t)\right\} = \bar{p}(t) - \bar{p}'(0) \Leftrightarrow \bar{n}(t) = \frac{\bar{p}(t) - \bar{p}'(0)}{|\bar{p}(t) - \bar{p}'(0)|} \tag{2.49}$$

applying that the $\{2\bar{p}(t) \cdot \bar{n}(t)\}$ term is a scalar and in this context used for normalization of $\bar{n}(t)$ only. The system can be optimized (if possible) by setting $\bar{p}'(0) = [0 \quad 0 \quad 1]^T$ such that the object (token) is imaged in the center of the image plane. Distortions and optical aberrations from the lens are hereby minimized.

Motion compensation using a folding mirror can only realize a one or two-axis compensation. Rotation of the mirror around it's surface normal does not change the optical path. A full compensation can therefore only be applied to motions, where the rotation vector Ω is located in the x-y plane of the imager reference frame.

For a practical implementation, the mirror will be limited to a certain size effectively limiting the applicable observation range. It is additionally presumed that the object distance is large relative to the distance to the mirror.

Alternatively, the imager and folding mirror can be treated as one combined unit defining a new reference frame $R'(t)$ depending on the mirror surface normal at time t, $\bar{n}(t)$. The three axes defining $R'(t)$ will all be mirrors of the axis defining R, such that $R'(t)$ will realize a left-handed reference frame:

$$R'(t) = R - 2\bar{n}(t)\left[\bar{n}(t)^T R\right] \tag{2.50}$$

This definition is highly applicable if the full 3-axis attitude of the object is required (e.g. within star-tracking).

Additionally, since all irradiated photons are mirrored in the surface normal the projected image will be mirrored as well. However, a correction for this effect as part of the post-processing will be a minor detail.

The algorithms for deriving the control pulses for the mirror drives are analogue to the algorithms used for a mechanical motion of the imager (apart from a sign-change due to the mirror). An introduction to these will be given in the following section.

A study of an application using a folding mirror as compensation for spacecraft motion during image integration has been carried out as part of this work. This work is described in two publications [4], [5] as well as a technical report [11]. This study is further discussed in §3.2.

2.8.2 Mechanical Motion of the Imager

Alternatively, the entire imager can be rotated in order to counteract for the motion of the object. This application is widely used within the field of ground-based astronomical telescopy, where the rotation of the Earth causes an apparent motion of the celestial sphere. The faint targets observed, typically require integration periods of tens of minutes to meet the required S/N ratios. During a typical integration of 20 minutes for a 0.5° FOV telescope, the Earth will be rotating 5° corresponding to 10 times the telescope FOV.

For this particular application, the object motion is well established, enabling the possibility to observe using an open loop control. The motion characterization feedback in the flowchart (figure 2.9) is therefore omitted. The rotation vector Ω is equal to the Earth rotation axis. ω is determined from T_{int} and the Earth's sidereal revolution time relative to the star-field of ∼23hours and 56minutes.

Consider again the orthonormal reference frame R being defined outside the imager. The imager attitude $\bar{\bar{A}}(t)$ is determined from the location of the imager axis (image plane and optical axis) within R. For a one-axis

compensation system, the imager can be re-oriented about a rotation vector Ω_1 defined in R. The imager pointing is determined from the imager attitude $\bar{\bar{A}}(t)$ z-axis within R, denoted $\bar{p}(t)$. Since $\bar{p}(t)$ will be rotated about Ω_1, $\bar{p}(t) \cdot \Omega_1$ will be constant.

The possible imager pointings (the trace of $\bar{p}(t)$ on a unit sphere in R) depends on the angle between $\bar{p}(t)$ and Ω_1, such that:

$$\text{trace of } \bar{p}(t) = \begin{cases} \text{greater circle} & \bar{p}(t) \cdot \Omega_1 = 0 \\ \text{smaller circle} & 0 < \bar{p}(t) \cdot \Omega_1 < 1 \\ \text{point} & \bar{p}(t) \cdot \Omega_1 = 1 \end{cases} \tag{2.51}$$

The 1-axis compensation system is sufficient if the object motions are envisaged to be in one dimension only (e.g. the product on an assembly line). For other applications it is a severe drawback that only a limited part of the unit sphere can be targeted.

A second rotation axis $\Omega_2(t)$, $\Omega_1 \neq \Omega_2(t)$ can be introduced, such that the imager can be re-oriented in two different directions. The drive generating the rotation about $\Omega_2(t)$ is considered to be mechanically realized closer to the imager, such that the position of $\Omega_2(t)$ within R depends on the current rotation about Ω_1 (explaining the Ω_2 time-dependency).

If $\Omega_1 \cdot \Omega_2(t) = 0$ (the rotation axes are orthogonal), the imager can be oriented on the entire unit sphere. Otherwise, only a section dependent on the geometry between Ω_1, $\Omega_2(t)$ and $\bar{p}(t)$ can be targeted.

If $\Omega \cdot (\Omega_1 \times \Omega_2(t)) = 0$ (Ω is located within the $\Omega_1/\Omega_2(t)$ plane) the motion of the object can be fully compensated for. Otherwise, pointing to the object can be maintained but the object will have an apparent rotation about the optical axis. This rotation is often referred to as *field rotation*. Additionally, since the orientation of the $\Omega_1/\Omega_2(t)$ plane within R depends on Ω_1, if field rotation is to be avoided Ω must be parallel to either Ω_1 or $\Omega_2(t)$.

In order to avoid field-rotation for all possible rotation vectors, a third axis of compensation $\Omega_3(t)$ e.g. orthogonal to $\Omega_2(t)$ can be introduced. If $\Omega_3(t)$ is chosen such that it is parallel to $\bar{p}(t)$, the required compensation about $\Omega_3(t)$, ω_3 is exactly equal to the field rotation (see figure 2.13).

Within astronomical telescopy, a typical telescope drive implementation contains 2-axis compensation system. For a polar-aligned altitude-azimuth system, Ω_1 will be parallel to the Earth's rotation vector, while $\Omega_2(t)$ is realized orthogonal to this axis. All targets available on the celestial sphere (if not occluded by the Earth) can be tracked. Additionally, objects having a small proper motion will be imaged without field rotation.

For a zenith-aligned altitude-azimuth system, Ω_1 will be parallel to the local zenith direction, and $\Omega_2(t)$ is realized orthogonal to this axis. All targets available can be tracked, but practically all target acquisitions will contain field rotations.

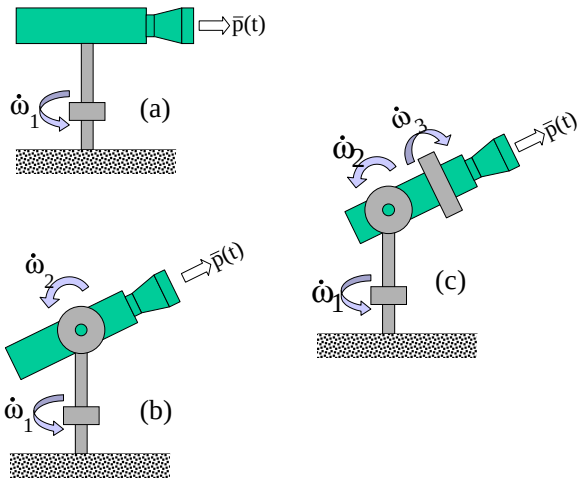

Figure 2.13: Examples on realizations of 1 (a), 2 (b) and 3-axis (c) compensation drives. $\dot{\omega}_i$ denotes the angular velocity about rotation vector Ω_i. In example (b) a zenith aligned altitute/azimuth drive is realized.

2.8.3 Synthetic Aperture

If a mechanical drive to reposition either the imager or a folding mirror is not practical for a given application, the light can be re-directed after entering the lens. A transparent plate e.g. made out of silicon can be mounted on a small tip/tilt system directly in front of the image sensor. The difference in refraction index between the silicon and the air gap will change the phase of the irradiated photons. By controlling the orientation of the plate, the photons can be repositioned on the image sensor.

2.8.4 Drift Scan

As an alternative to manipulating the direction or phase of the irradiated photons, the electrons generated by the photon impacts can be controlled. For a CCD, the electrons will be collected on the charge carriers by a positive

potential. The charge carriers are separated by other charge carriers having a negative potential.

When the image integration has been concluded, the integrated charges are read out, by concurrently shifting all pixels one line at a time into a horizontal 1-dimensional readout register. This readout technique is based on the charges being coupled together linewise by charge carriers, yielding the technology name *charge coupled device*. The integration and readout technique can be compared with rain being collected in an array of buckets as illustrated in figure 2.14 (horizontal and vertical has been exchanged relative to the conventional naming).

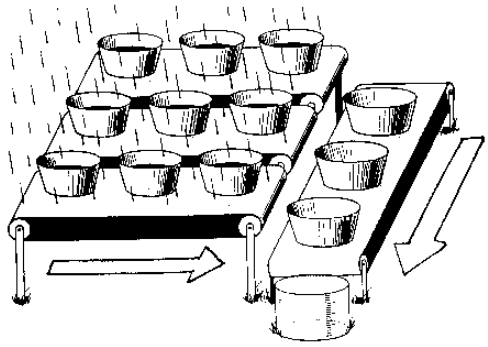

Figure 2.14: Principle of CCD operation using integration of rain in buckets. Courtesy D. Vielmann 1997

During the readout, all the "horizontal" conveyer belts are moved one line at a time, moving the collected rain into the buckets in the "vertical" conveyer belt, transporting the buckets out one at a time. In the following description, the *vertical* readout will represent the array of belts in the integration area, whereas the *horizontal* readout will represent the final single line readout.

The timing of the potentials of the charge carriers are controlled by a dedicated *timing generator*, while the actual potentials are generated by a *line driver*. The vertical readout pulse period T_{vert} is the time between two successive pixel lines are read out.

Consider now, that the CCD is used in an imager system to acquire an image of a moving point source O located in $\bar{p}(t)$. The motion has been established to be moving about Ω on a greater circle about the imager (i.e. $\Omega \cdot p(t) = 0$). The trace of O in the acquired image will be a straight line spanning $\lceil T_{int}/T_{pix} \rceil$ pixels, where T_{int} is the integration time and T_{pix} is

the mean time needed for the object trace to move one pixel in the imager plane.

The imager is physically positioned, such that the imager horizontal readout axis (denoted the x-axis) is aligned with the Ω in such a way that the image trace of the object is moving along the y-axis towards the horizontal readout register. The imager is rotated about the x-axis, such that the object is imaged in the rim of the image at time $t = 0$ (see figure 2.15).

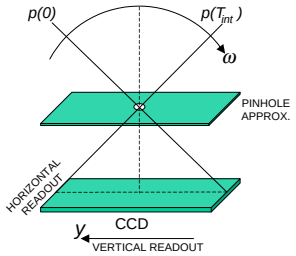

Figure 2.15: Sketch of the motion required to perform drift scan motion compensation. The object O moves from $\bar{p}(0)$ to $\bar{p}(T_{int})$ within the integration period

If the number of CCD pixel lines along the y-axis is denoted N_y, the time for the object trace to transit the CCD $T_{transit}$ will be: $T_{transit} = N_y T_{pix}$. If the timing generator clock frequency is adjusted such that $T_{vert} = T_{pix}$, the readout of the CCD will follow the trace of O. This simultaneous image integration and readout will (almost) remove the otherwise introduced motion smear. This motion compensation technique is referred to as *drift scan*.

The effective integration time $T_{int,eff}$ can *not* be arbitrarily selected, since it is determined by the angular velocity of O about Ω, $\dot{\omega}$ as well as the imager y-axis FOV, $2\beta_y$, such that

$$T_{int,eff} = \frac{2\beta_y}{\dot{\omega}} \tag{2.52}$$

One advantage of this technique is that the image integration can be extended arbitrarily, effectively extending the image dimension along the y-axis (see figure 2.16).

The object is rotating about Ω with a constant rotation rate $\dot{\omega}$. The projection will be moving accordingly on the imager plane along the y-axis. Since the object trace on a sphere is projected on a plane, distortions will

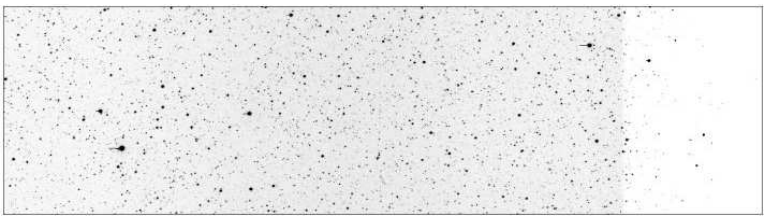

Figure 2.16: Example astronomical image acquired using drift scan. Courtesy Christian Buil (Audine) 2004.

be introduced. Likewise, if the drift scan is performed at a constant rate T_{vert} a blurring will be taking place. The blurring magnitude will increase at an increasing FOV along the y-axis. The scenario is illustrated in figure 2.17.

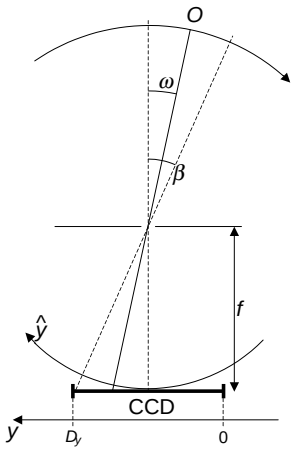

Figure 2.17: Distortion induced from spherical mapping on a plane. $\omega(t)$ is the present angular position of the object O, $y(t)$ is the projected position on the imager plane, while $\hat{y}(t)$ is the projection on a sphere with radius $r = f$

The object O rotates with an angular rate of $\dot{\omega}$. At time t the angular position of O is $\omega(t) = \dot{\omega}t$. The position in the imager plane at time t is $y(t) = f \tan \omega(t)$ while the position on the (distortion free) sphere is $\hat{y}(t) = f\omega(t)$.

In order to limit system complexity, T_{vert} is held constant during the

drift scan. Let T_{vert} be chosen such that

$$T_{vert} = \frac{T_{int,eff}}{N_y} = \frac{2\beta_y}{\dot{\omega} N_y} \tag{2.53}$$

The distance of the sphere, on which $\hat{y}(t)$ is projected is extended with a factor k such that $y(T_{int,eff}) = k\hat{y}(T_{int,eff})$, where $\omega(T_{int,eff}) = \beta_y$, i.e.

$$\begin{aligned} & y(t_{int,eff}) = k\hat{y}(t_{int,eff}) \\ \Rightarrow \quad & f\tan(\beta_y) = kf(\beta_y) \\ \Leftrightarrow \quad & k = \frac{\tan(\beta_y)}{\beta_y} \end{aligned} \tag{2.54}$$

The normalized error in projection $\epsilon(t)$ can now be determined:

$$\begin{aligned} y(t) - k\hat{y}(t) &= f\tan\omega(t) - f\frac{\tan(\beta_y)}{\beta_y}\omega(t) \\ \Leftrightarrow \frac{y(t) - k\hat{y}(t)}{D_y} &= \frac{f}{D_y}\left(\tan\omega(t) - \frac{\tan(\beta_y)}{\beta_y}\omega(t)\right) \\ &= \frac{1}{2\tan(\beta_y)}\left(\tan\omega(t) - \frac{\tan(\beta_y)}{\beta_y}\omega(t)\right) \\ &= \frac{1}{2}\left(\frac{\tan\omega(t)}{\tan\beta_y} - \frac{\omega(t)}{\beta_y}\right) \\ &= \epsilon(t) \end{aligned} \tag{2.55}$$

where small errors $\epsilon(t)$ are assumed. Using this definition, $\epsilon(t)$ depends on the FOV β_y and the current angular position $\omega(t)$. Furthermore, $\epsilon(t)$ is normalized such that it is independent on the focal length. In figure 2.18 $\epsilon(t)$ is illustrated for $\beta_y = 1°, 3°$ and $5°$.

The maximum normalized errors ϵ_{max} depends heavily on β_y. Figure 2.19 shows ϵ_{max} as function of β_y.

E.g. for a system having FOV $= 10°$ ($\beta_y = 5°$), $\epsilon(t)$ peaks at $\epsilon_{max} = \pm 5 \cdot 10^{-4}$. If the number of pixels along the y-axis in the image plane $N_y = 1000$, the error in pixels $\epsilon_p(t)$ will peak at $\epsilon_{p,max} = N_y\epsilon_{max} = \pm 0.5$pixels.

Since the projection errors $\epsilon(t)$ are the mapping errors of a point source, the evolution of $\epsilon(t)$ during the integration can be used to define a point spread function generated by the drift scan, $psf(\beta_y)$. Since the motion is along the y-axis passing through the optical axis, $psf(\beta_y)$ will not have an extent along the x-axis. Figure 2.20 shows the y-z plane projection of $psf(\beta_y)$ for $\beta = 1°, 3°$ and $5°$:

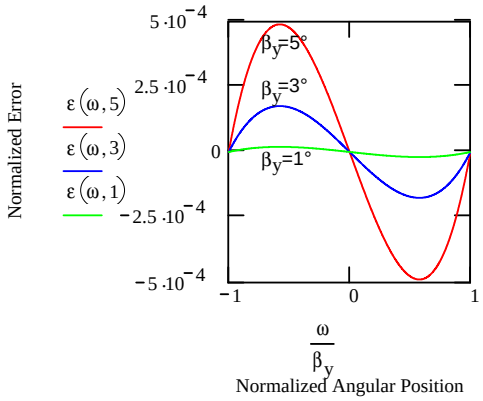

Figure 2.18: Normalized drift pointing error as function of FOV.

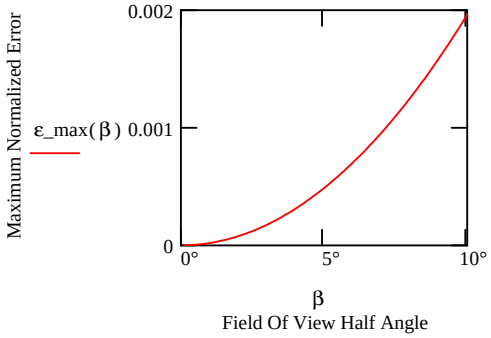

Figure 2.19: Maximum normalized error as function of FOV half angle (β)

The overall system PSF can now be determined by a convolution of the lens PSF and $psf(\beta_y)$. If the object trace is not passing the optical axis, a distortion will also be present along the x-axis due to the spherical projection. A combined PSF can be found from calculations similar to the y-axis PSF. This motion will not be treated within this work. For astronomical imaging, the FOV will usually be relatively narrow, yielding a negligible smearing.

An additional effect is that the thermal induced pixel noise is highly pixel dependent. Integration of a point source in N_y different pixels will lead to an averaging of the induced thermal noise, effectively decreasing the imaging

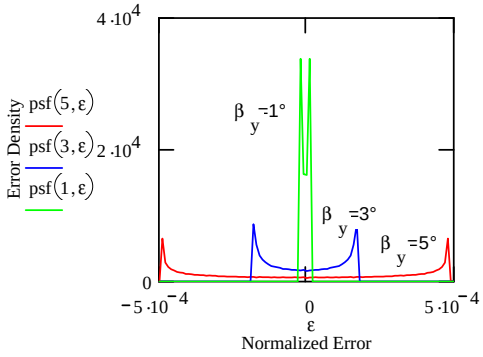

Figure 2.20: y-z plane projection of the point spread function $psf(\beta_y)$ induced by drift scan for FOV half-angles $\beta = 1°, 3°$ and $5°$

noise. The advantages and drawbacks of the drift scan concept are listed in table 2.2.

Table 2.2: Advantages and drawbacks of the drift scan concept

Advantages	Drawbacks
No motion of any mechanical parts	Added motion smear at large FOV's
Arbitrary extension of the y-axis image dimension	Limitation in choice of system FOV and effective integration time
Decrease of imaging noise due to averaging of thermal induced noise	Compensation can only be realized about one axis AND in one direction

This motion compensation technique is often found within the field of amateur astronomical imaging relaxing the mechanical drive stability requirements. The constant well-defined motion of the stars across the night sky at a rate $\dot{\omega} \approx 15as/s$ will for a $\beta = 0.5°$ imager result in an effective integration period of $T_{int,eff} = 240s$. For image acquisition outside the equatorial plane of the Earth (not orthogonal to the rotation vector), the angular velocity of O within the imager reference frame will decrease with

the cosine to the declination δ. Additionally, an increasing field rotation will be introduced.

2.8.5 Time Delayed Integration

Typically, a given system application will pose strict requirements on the imager FOV, $2\beta_y$ along the y-axis, as well as integration time T_{int}. Using the concept of drift scan imaging, and according to eq. 2.52, a fixed value of these two parameters would only allow for motion compensation of a fixed object angular velocity

$$\dot{\omega} = \frac{2\beta_y}{T_{int}} \tag{2.56}$$

Alternatively, requirements of compensation for a given angular velocity and imager FOV will lead to a fixed integration period. This period will be important for some applications because it simultaneously defines the data latency as well as the maximum imaging frequency.

Additionally, imaging of targets having different angular velocities will lead to different integration periods, which in turn will lead to different image qualities in terms of S/N ratios.

The drift scan motion compensation technique is based on pixel readout and pixel motion being performed simultaneously. Alternatively these two tasks can be separated, such that during the imager integrations the pixels are moved to compensate for the motion. When a sufficient S/N ratio has been achieved, the image pixels are read from the CCD using the standard (usually faster) read-out procedure. This technique is referred to as *time delayed integration* or *TDI*.

Since the object can only be tracked when it is present within the imager FOV, there is an upper limit in the selection of integration time, such that

$$T_{int} \leq \frac{2\beta_y}{\dot{\omega}} \tag{2.57}$$

In the following description it is presumed that the integration time T_{int} is fixed. It is furthermore presumed that Ω is located along the imager x-axis. O will be moving with an angular velocity $\dot{\omega}$. The trace angle ω during the integration period can be found from

$$\omega = T_{int}\dot{\omega} \tag{2.58}$$

If N_y is the number of pixel rows and β_y is the y-axis half-angle FOV, the number of rows over which the object O is distributed N_{tdi} can be found

from

$$N_{tdi} = \frac{\omega}{2\beta_y} N_y = \frac{T_{int}\dot{\omega}}{2\beta_y} N_y \tag{2.59}$$

where a relatively small FOV is assumed such that the distortion from the spherical projection is negligible. Since the angular velocity of O will be constant during the integration, and setting the time $t = 0$ at the beginning of integration, the operation of moving the pixels one row shall be performed at

$$t = t_n = \frac{n + 0.5}{N_{tdi}} T_{int} \qquad n = \{1..N_{tdi}\} \tag{2.60}$$

Let the pixel rows be enumerated from $j = 0..N_y - 1$, N_y being the total number of pixel rows. The row numbering is such that $j = 0$ is closest to the horizontal readout register. Let the rotation rate $\dot{\omega}$ of O be such that the trace is moving in the +y direction (away from the readout register). From $t = 0$ to $t = t_1$ normal image integration will take place. At $t = t_1$ the integrated charges are concurrently moved one pixel row in the +y direction. After the shift, the pixels located in $j = 0$ have *not* been integrated. Integration will take place between $t = t_1$ and $t = t_2$ followed by a second charge shift (in +y). The pixels now located in $j = 0$ have not been integrated whereas the pixels located in $j = 1$ have been integrated within the time interval $t = [t_1; t_2]$ and so forth. At $t = T_{int}$ the pixel rows will have received the following effective integration time:

$$T_{int,eff}(j) = \begin{cases} T_{int}\frac{j+0.5}{N_{tdi}} & j \in \{0..N_{tdi} - 1\} \\ T_{int} & j \in \{N_{tdi}..N_y - 1\} \end{cases} \tag{2.61}$$

This effect is also visible in the right side of the drift scan image in figure 2.16. Since this effect is deterministic it can be partially compensated for by amplifying the image pixels accordingly. Obviously the S/N ratio is not improved by this operation. Alternatively the image dimension can be reduced in the post-processing such that the N_{tdi} pixel rows are removed, yielding a constant S/N ratio in the entire image.

Analogous to the drift scan compensation, a distortion originating from the spherical projection will be introduced (for large FOV's). For a small $\dot{\omega}$, the distortion will translate into a shifted y-axis position (according to figure 2.18), which can be compensated for in the post-processing. For large $\dot{\omega}$, the distortion will translate into a smearing as well as a position shift.

As with the drift scan approach, integration of a point source in N_{tdi} different pixels will lead to an averaging of the induced thermal noise ef-

fectively decreasing the imaging noise. The advantages and drawbacks of motion compensation using TDI are summarized in table 2.3.

Table 2.3: Advantages and drawbacks of the time delayed integration concept

Advantages	Drawbacks
No motion of any mechanical parts	Added motion smear at large FOV's *and* large $\dot{\omega}$
System FOV and effective integration time can be chosen independently	Reduction of the y-axis dimension
Decrease of imaging noise due to averaging of thermal induced noise	Compensation can only be realized about one axis (in both directions)

An application using TDI for star-tracking has been developed as part of the thesis work. This work is described in detail in §3.1.

2.8.6 Superposition of Shifted Images

In the previous two sections motion compensation techniques where the image is moved along with the projected object trace were described. These techniques can be regarded as an on-chip superposition of shifted images.

Alternatively this superposition can be performed at multiple sub-images after the image sensor readout. Each sub-image will contain a part of the motion, e.g. corresponding to the object trace transition of one pixel. Before adding the pixels of the n'th sub-images $p_{i,j}^{(n)}$, they are shifted according to the object motion:

$$p_{i,j} = \sum_{n=0}^{N-1} p_{i+nv_x,j+nv_y}^{(n)} \tag{2.62}$$

where N is the number of sub-images, and v_x and v_y are the the object motion along the x and y-axis respectively between two sub-images. Eq. 2.62 assumes a linear motion, but also more complex motions can be recovered by assigning individual object motions v_x and v_y to each sub-image.

An additional advantage using superpositioning is that the compensation can be performed for any given rotation axis Ω. Image rotations and sub-pixels motions can be recovered using pixel interpolation.

Unfortunately, all sub-images will contain the readout noise and the quantization noise contributions listed in §2.3.5. Assuming a white noise distribution and an S/N ratio η at a certain integration time T_{int}, sub-image n will have S/N ratios $\eta_n = \eta/N$ (the signal is divided by N, the noise is unchanged). After the superposition, the total S/N ratio will be $\eta_N = \eta/\sqrt{N}$. On the other hand, the thermal induced noise will be decreased due to averaging.

Similarly to the TDI compensation technique, image parts close to the edges in the motion direction will not be integrated for the full integration period. This will lead to either a non-uniform S/N ratio or a dimension reduction. The advantages and drawbacks of superposition are summarized in table 2.4.

Table 2.4: Advantages and drawbacks of the superposition compensation concept

Advantages	Drawbacks
No motion of any mechanical parts	Added motion smear at large FOV's *and* large $\dot{\omega}$
System FOV and effective integration time can be chosen independently	Reduction of the motion axes dimension
Compensation can be realized about any axes	Increase of imaging noise due to accumulation of system noise

Chapter 3

Case Studies

3.1 Case: Star-Tracking at High Rotation Rates

Motion compensation using time-delayed integration

The platform attitude profile is for most spacecrafts a vital part of the performance envelope. In addition to serving science requirements such as science telescope pointing, it is also being included in bus tasks, such as antenna pointing. Any spacecraft is in itself an inertial body, which will be rotating freely if not actively controlled. On spinner satellites in contrast to 3-axis stabilized satellites, the spacecraft orientation is partly maintained by rotating the spacecraft about a given rotation axis Ω. Both Ω and the rotation velocity $\dot{\omega}$ is well defined by the mission specifications.

The attitude is controlled using an *attitude control system* (ACS). Apart from featuring a suite of actuators, the ACS will also contain a suite of sensors. The currently most accurate autonomous attitude sensors are star-trackers. One of the basic problems associated with aerospace star-tracking is the mass/performance trade-off: The number of photons irradiated from the stars on the lens is highly limited, while the lens must be small in order to limit the mass. In order to achieve the required centroid accuracy, the image integration must thus take place for a relatively long period of time (§2.4.3), typically in the range of 0.5s to 1s. For such relatively long integration periods, a star-tracker is highly susceptible to angular motions. A star-field image acquired by such a star-tracker at an integration time $T_{int} = 0.5$s and an angular velocity $\dot{\omega} = 4°/$s is shown in figure 3.1. The image has been inverted in order to accentuate image details.

The stars shown in the figure appear as stripes elongated along the ver-

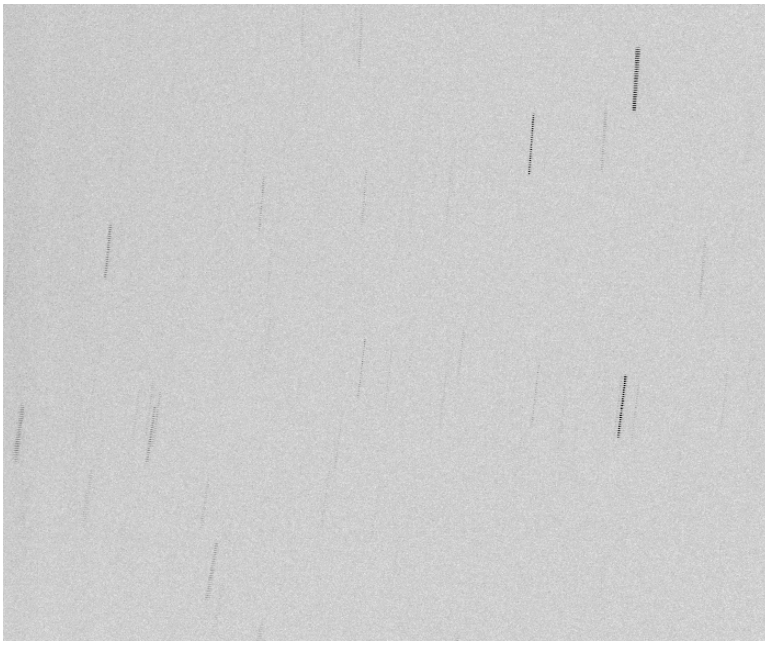

Figure 3.1: Inverted ASC image acquired $T_{int} = 0.476$s and $\dot{\omega} = 4°/$s

tical axis. More specifically, the following effects are observed:

- The stars will appear as stripes in the image rather than dots defined by the PSF of the lens system. This is not in accordance with the model of the expected star used for centroiding, causing an accuracy decrease.

- The irradiated photons will be dispersed over a larger support area. A substantially higher amount of background noise is therefore included in the measurement, hereby decreasing the accuracy.

- The larger support area of the individual star will cause a drop of the intensity at pixel level with a following decrease in detectability. This is especially a problem for the fainter stars.

- The motion will, in turn, cause some of the stars to pass the rim of the image during the integration. The centroids of star traces that touch this rim will consequently be misplaced by the centroiding algorithm.

This particular star-tracker has already been optimized for operation during high angular velocities. The performance starts to degrade at cross-axis rotation rates of $\dot{\omega} = 4°/s$ and will be lost when approaching $\dot{\omega} = 8°/s$. This performance envelope is illustrated in figure 3.2, where the validity or rate of successfully recovered attitudes is plotted versus the angular motion rate.

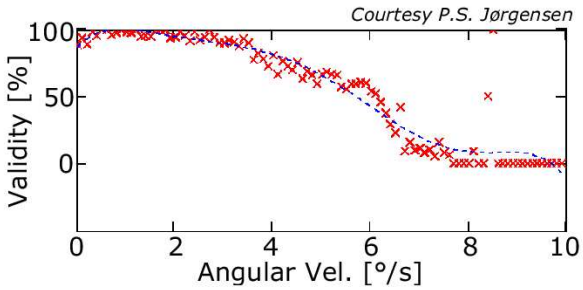

Figure 3.2: Validity versus angular rate for the ASC star-tracker. The isolated high validity points about $\dot{\omega} = 8.5°/s$ is due to a very low number of samples in this particular rate measurement region.

It is apparent that star-tracker attitude recovery is limited for the spacecraft de-tumbling phase and for spacecraft missions with high spin-rates, also referred to as *spinners*.

3.1.1 Introduction to the Advanced Stellar Compass

The Advanced Stellar Compass (ASC) is a fully autonomous star-tracker developed at the Technical University of Denmark (DTU). The instrument has successfully served as reference attitude sensor on a wide selection of satellites missions. The instruments features up to two CHU's, which can be operated at integration periods ranging from 1/16s up to 8s. A picture of an ASC DPU, with two inner baffle mounted CHU's and one separate CHU is shown in figure 3.3.

The optical and sensor specifications of the CHU's are:

- Effective Focal Length (EFL), f = 20mm
- Rectangular FOV, $2\beta_x \times 2\beta_y = 18.4° \times 13.7°$
- Lens aperture, 25mm (F/0.8)

Figure 3.3: The Advanced Stellar Compass shown with three CHU's. The two CHU's are mounted on baffles.

- Sensor technology: CCD (interline transfer)
- Number of pixels, $N_x \times N_y = 752 \times 580$
- Sensor pixel size, $\Delta x \times \Delta y = 8.6\mu\text{m} \times 8.3\mu\text{m}$
- Optional interlaced imaging using field integration.

The ASC contains a Camera Head Unit (CHU), which is basically a digital camera used to acquire images of the star-field. The images are input to a Data Processing Unit (DPU), a computer that determines the 3-axis orientation or attitude of the CHU based on the image position of stars relative to a star database. The process of attitude determination is realized in a series of logical steps:

- *Image acquisition* where the image is integrated and read out from the image sensor. The image is quantized using analog to digital conversion (ADC), before it is finally transported to a storage location.
- *Image post-processing* where the image read from the CHU is rectified and prepared for the image analysis. This step include image cropping

to the required dimensions, merging of image fields in case of interlaced image integration, and filtering to suppress noise and radiation damage effects. The output of this step is a proper processed image.

- *Centroiding* is the step of image analysis, where the image is systematically sifted for objects (stars). The objects are isolated and their positions and luminosity are found. The result of this step is a list of centroids (image positions describing the center of intensity) as well as the intensities of the isolated objects.

- *Pattern matching.* The list of centroids is input to a pattern matching algorithm that determines the attitude of the image by comparison against a database of star positions and visual intensities.

3.1.2 Analysis

Since the TDI star-tracker is designed for an aerospace application, the key design drivers (§1) must be taken into account. Introduction of a folding mirror in front of the CHU will add both mass, power and system complexity. Mounting the CHU on a mechanical drive will face the same difficulties. Image super-position will add noise to the measurements and will require extended computational power to perform the image pixel addition. On the other hand, the techniques where the electrons are moved on the CCD seems favorable.

The integration time of the ASC is defined by the internal clock oscillator and can only be varied in 8 discrete steps, such that:

$$T_{int} = 0.951 \cdot 2^{n-4}\text{s} \qquad n \in \{0..7\} \tag{3.1}$$

In case the drift scan motion compensation (§2.8.4) should be applied, the fully compensated motion rates $\dot{\omega}$ supported can be found from eq. 2.56:

$$\dot{\omega} = \frac{2\beta_y}{T_{int}} = \frac{13.7^\circ}{0.951 \cdot 2^{n-4}\text{s}} \qquad n \in \{0..7\} \tag{3.2}$$

such that $\dot{\omega}$ must be found within the discrete set:

$$\dot{\omega} \in \{230, 115, 57.6, 28.8, 14.4, 7.20, 3.60, 1.80\}^\circ/\text{s} \tag{3.3}$$

Since the attitude recovered by the star-tracker is included in the spacecraft attitude control loop, there are strict constrains about the attitude accuracy as well as the attitude latency. This timing latency is measured from the center of integration (COI) to attitude output. The possibility of

fulfilling these requirements together with the spin rate requirement is very low, effectively limiting the possible applications.

Alternatively, the instrument flexibility can be increased substantially by implementing the TDI motion compensation. This compensation technique has been chosen for the further study.

3.1.3 Implementation

The ASC star-tracker CHU's have at the time of this work acquired some 35years of in-flight heritage. A design driver for this implementation is therefore to modify the current hardware in such a way that the minimum design impact is reached, and as much of the CHU as possible can retain its flight heritage. For this purpose, a short introduction to digital imaging is required. A block diagram of the required components is shown in figure 3.4.

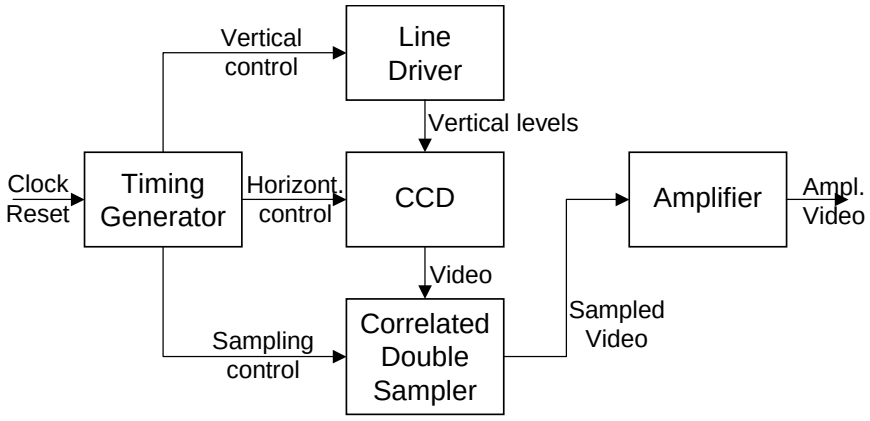

Figure 3.4: Block-diagram of a CHU architecture.

The CHU contains the following logical (and physical) blocks:

- The *Timing generator (TG)* module uses the master clock and the vertical and horizontal reset pulses as input. The vertical reset pulse marks the beginning of an image (image, field or frame), whereas the horizontal reset pulse marks the beginning of a new line. The output is control signals to flush the integrated charges from the integration layer into the readout layer (vertical registers) (XSG1 and XSG2). In addition, pulses to move the charges in the vertical registers (XV1-XV4), and in the horizontal (readout) register (H1 and H2) is ouput.

Finally, the output reset gate pulse (RG) as well as sampling pulses (SHP and SHD) are generated .

- The *line driver* is a simple level converter that transforms the flush and vertical TTL level pulses into the right potentials needed for the vertical charge carriers within the CCD. The output pulses are the vertical potentials V1-V4 and the flush levels SG1-SG2.

- The *CCD* used for the ASC is an inter-line transfer type CCD, which means that the charges are integrated for a certain integration period T_{int}. After integration, the charges are all concurrently moved to a parallel (covered) readout register (using SG1 and SG2), so that a new image integration can start immediately. The levels V1-V4 are used to shift the charges one line at a time in the vertical readout register. The pulses H1-H2 (internally level-converted) are used to shift the charges within the horizontal readout register one pixel at a time into the output gate. For further description please refer to the CCD data sheets [21].

- The *Correlated Double Sampler (CDS).* After each pixel readout, the output gate must be reset, such that the following integrated charge can be moved to the gate. This reset potential can cause a non-constant potential at the gate, which will add noise to the measurement. After each gate reset, the gate potential is therefore latched in the CDS, such that the charge is amplified relative to this level. The latching of the reset potential and the charge potential is controlled by the SHD and SHP pulses.

- The *amplifier.* When the video signal has been sampled it is amplified to the correct (system dependent) levels.

It appears from the block diagram in figure 3.4 that the camera integration is fully controlled by the timing generator (TG). Since the CCD is an interline-transfer type, the vertical readout registers are used as intermediate charge storage during the image integration. The task of moving the integrated charges one line (tracking the object motion) must therefore be immediately superseeded by a flush operation, to move the current charges to the readout layer. The integrated charges can be moved within the readout layer in the forward direction by applying the standard V1-V4 level sequence, or in the backward direction by reversing the V1-V4 level sequence.

The architecture of the interline-transfer CCD featuring a decomposition into two layers (integration and readout) allows for parallel integration of the second field (odd lines) of the image while the first field (even lines) is moved out. A 100% duty cycle of the chip is hereby achieved. A timeline showing the integration and readout of two field-integrated images are shown in figure 3.5.

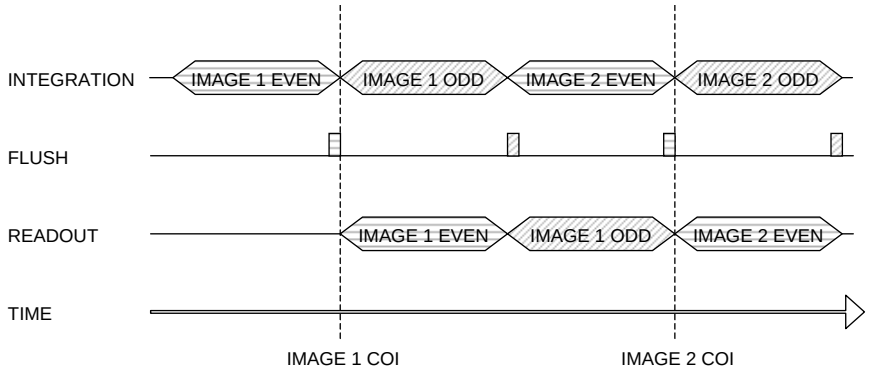

Figure 3.5: Timeline of field integration of two images. The integration of the odd field is performed while the even field is being read out. The image center of integrations (COI) are marked with dashed lines.

Since both the integration layer and the readout layer are involved in the TDI image integration, this pipelining can not be realized. Interlaced imaging is achievable, but since a high image motion is taking place, it is not meaningful to implement. The TDI compensation operation will consequently generate images with only the half number of lines ($N_y = 290$ for the applied CCD). Since each line is found from a superposition of two neighbor lines (field integration), the effective integration time of one field is equal to the effective integration time for a complete interlaced image (two fields).

The acquisition of a TDI image is divided into two phases, which cannot be pipelined: The TDI phase and the image readout phase. The number of TDI shifts (sub-integrations) required is a function of ω and β_y and can be determined from eq. 2.59. Each sub-integration contains the following sequence:

1. Integration of charges in the integration layer.

2. Moving the charges in the readout layer one pixel in either the forward

or backward direction (depending on the sign of $\dot{\omega}$).

3. Flushing the integrated charges into the readout layer.

The timeline of two TDI image integrations with $N_{tdi} = 3$ is shown in figure 3.6

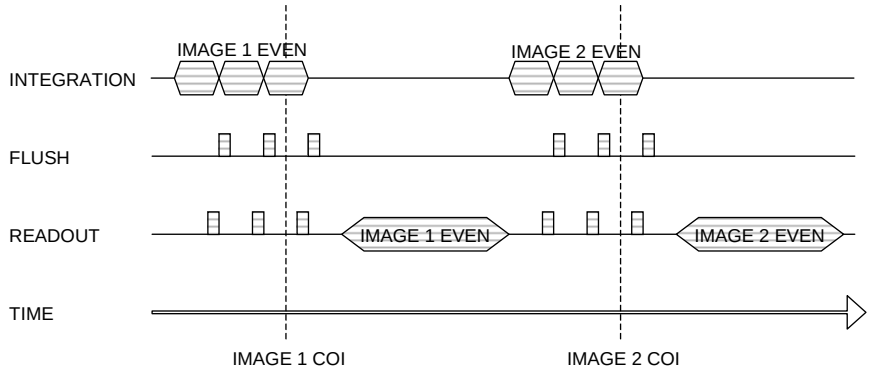

Figure 3.6: Timeline of TDI integration of two images with $N_{tdi} = 3$. Only integration of one field (the even) is possible. The image COI's found from eq. 3.4 are marked with dashed lines.

Since the spacecraft will be spinning with an angular velocity of several degrees pr. integration period, and the aim is to measure the attitude with an arc-second accuracy, the image timestamping relative to the integration is crucial. If the COI is displaced by just a few milli-seconds, the attitude measurement will generate huge biases that are rotation rate dependent.

This timestamping integrity can only by ensured if the angular acceleration $\ddot{\omega} = \frac{d\dot{\omega}}{dt} = 0$. Two apparent methods are available:

1. Since the TDI mimics an on-chip sub-image superposition, the object position in the final image will be equal to the object position in the last integrated sub-image. The temporal position of the COI is therefore in the center of the last sub-integration. The COI offset relative to the beginning of integration (BOI), ΔT_{COI} can therefore be found from:

$$\Delta T_{COI} = \frac{T_{int}}{2}\left(1 - \frac{1}{2N_y}\right) \qquad N_y \geq 1 \tag{3.4}$$

Unfortunately, if the true image motion is slightly different from the expected (modelled), a residual image motion will be present and the centroid will be misplaced relative to the COI.

2. Alternatively, the full integrated image can be physically displaced during post-processing corresponding to the TDI motion taking place during integration. The number of lines to displace the image N_{disp} is found from:

$$N_{disp} = \frac{N_{tdi} - 1}{2} \tag{3.5}$$

Since this adjustment is based on the true image displacement rather than the expected (eq. 3.4), it is favored.

As seen from table 2.3 one advantage of TDI motion compensation, is that the thermally generated pixel noise is averaged due to the super-positioning principle. In case the CCD suffers from radiation damages (§3.4), the characteristic hotspots will be averaged according to the TDI motion as well. In a TDI compensated image, these damages will therefore appear as elongated stripes rather than single pixels. Since the hotspots appear from thermally released charges, the effect can be reduced be lowering the operational CCD temperature.

It appears that the control signals used for the expected TDI operation are all generated by the TG. One obvious solution is therefore to exchange this with a custom built TG having the required capabilities. The Field Programmable Gate Array (FPGA) technology was chosen for this purpose.

A parallel computer interface was used to load the FPGA configuration as well as the TDI configuration, which allowed for 16 different TDI velocities in both forward and backward directions. The velocities supported are: $N_{tdi} = \{1, 2, 6, 8, 12, 14, 18, 20, 24, 28, 31, 34, 39, 44, 52, 62\}$ lines/integration.

3.1.4 Results

Two different tests were conducted for the prototype verification: A laboratory test, where the basic system functionalities were verified, and a real-sky (in-situ) test verifying the end-to-end performance. Throughout both testings the setup in figure 3.7 was applied:

The DPU was a standard ASC DPU. The CHU was a modified ASC CHU, where the TG was replaced by an FPGA implementation. The DPU is controlled by an Electronic Ground Support Equipment (EGSE) software

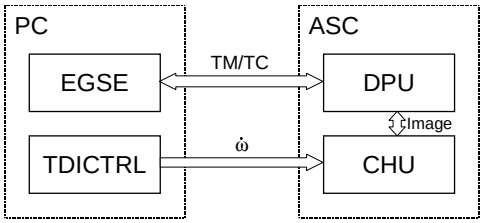

Figure 3.7: Test setup for the TDI compensation test.

program, capable of interpreting the attitude output. Finally, the CHU is controlled by a small console program, TDICtrl, capable of configuring and controlling the FPGA. TDICtrl and EGSE were located on the same test PC.

In the laboratory test a CCD hotspot was applied as target. Since the hotspot is a defect in a single CCD cell, it will appear in the same pixel of the image repeatedly. In addition, the intensity will be well established at a given temperature. The following test points were carried out:

- The introduction to the FPGA TG with $N_{tdi} = 1$ did not cause an image displacement.
- By monitoring the hotspot intensity it was verified that the system amplification was not affected.
- A slight increase in the background intensity variation was observed, which is expected to be due to the "mock-up" implementation with the FPGA being connected to the CHU electronics through relatively long cables.
- The time coherence between sub-integrations was verified by verifying that the pixel to pixel variation within the hotspot trace was comparable to the general pixel background variation.
- It appeared that compensation was only possible in the forward direction (i.e. towards the horizontal readout register). When backward compensation was exercised (e.g. moving the charge from $p_{x,y}$ to $p_{x,y+1}$), instead a smearing between $p_{x,y}$ and $p_{x,y-1}$ was realized (see figure 3.8).

  It is expected that this effect is generated by the architecture of the selected CCD, which could either be optimized for higher Charge Transfer Efficiency (CTE), be prepared for progressive scan, or similar. This

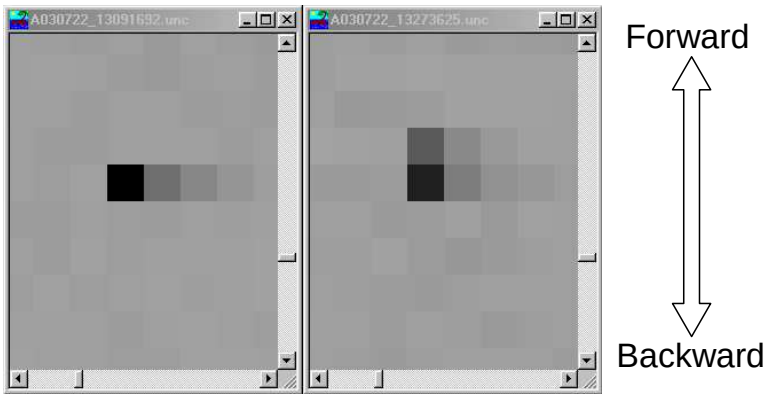

Figure 3.8: Result of backward charge transfer. The left zoomed image part shows an area with integrated charges. In the right zommed image part a backward motion was exercised leading to a forward smearing.

shortcoming limits the operational envelope of the selected setup, but does not affect the general verification of the TDI principle.

During the real sky testing, the CHU and DPU were mounted on the tip of a telescope, placed on a polar aligned altitude/azimuth drive.

By controlling the telescope pointing direction, arbitrary rotation vectors Ω and angular velocities $\dot{\omega}$ could be selected from the telescope console. Angular velocities up to $|\dot{\omega}| = 4°/s$ about each axis were supported by the telescope drive. The CHU was oriented, such that a motion about the right-ascension drive axis resulted in a star-field motion in the CCD y-axis. The response to non-orthogonal motions ($\Omega \cdot \bar{p} \neq 0$, $\bar{p}$ being the star-tracker pointing direction) could thereby be exercised. This was done by moving the declination drive axis, such that the pointing direction is non-orthogonal to the right-ascension drive axis.

When the attitude determination is concluded, a certain number of the stars within the image is recognized. Their observed apparent position can therefore easily be calculated. The deviation between this position and the true apparent position (found in a star catalogue) can be used as a measure of the obtained accuracy.

The integration period T_{int} and the angular velocity $\dot{\omega}$ were varied independently. The accuracy of the following centroiding is found in table 3.1.

The decreased accuracy at $T_{int} = 0.119$s (fastest CCD readout) is related

Table 3.1: Obtained centroiding accuracies (measured in arc-seconds) as function of T_{int} and $\dot{\omega}$. The entries marked "-" are not measured, "n/s" is not supported. The numbers in the parentheses are the number of TDI shifts (N_{tdi}).

Centroid accuracy [as] (TDI shifts N_{tdi})		Angular Velocity $\dot{\omega}$ [°/s] 1	2	4
$T_{int}[s]$	0.119	-	-	30" (8)
	0.238	-	17" (8)	23" (14)
	0.476	22" (8)	21" (18)	26" (39)
	0.951	20" (8)	22" (39)	n/s

to the mock-up design with long cables. Otherwise, the accuracies found are comparable with those obtained within stationary star-tracking. An image acquired at $\dot{\omega} = 4°/s$ with $T_{int} = 0.476s$ and $N_{tdi} = 39$ is shown in figure 3.9.

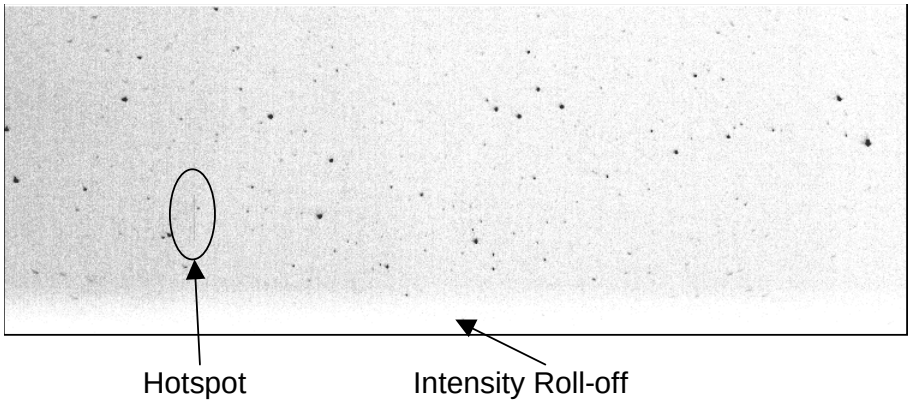

Figure 3.9: TDI compensated image at $\dot{\omega} = 4°/s$ with $T_{int} = 0.476s$ and $N_{tdi} = 39$

Based on the TDI image in figure 3.9 the following observations are made:

- The stars appear as distinct non-elongated objects.
- The stars appearing close to the edges are smeared. This is partly due

to optical aberration, which is an artifact of the applied lens system and is not related with $\dot{\omega}$, partly due to the observed direction (from the image rim) not being orthogonal to Ω.

- At the bottom (39 lines) the intensity roll-off characteristic for the TDI technique can be observed.
- Finally, the trace of a hotspot is present some 20% from the left edge, in the lower part of the image. As expected, the trace stretches over exactly 39 pixels.

In addition, images were acquired at non-orthogonal rotations. The basic problem is, that the apparent motion along the vertical axis is no longer constant in the different parts of the image. Secondly, a motion component will be present along the horizontal axis as well, which cannot be compensated for. An image acquired at a rotation angle from boresight of 62° at $\dot{\omega} = 4°/\text{s}$ with $T_{int} = 0.951\text{s}$ and $N_{tdi} = 62$ is found in figure 3.10.

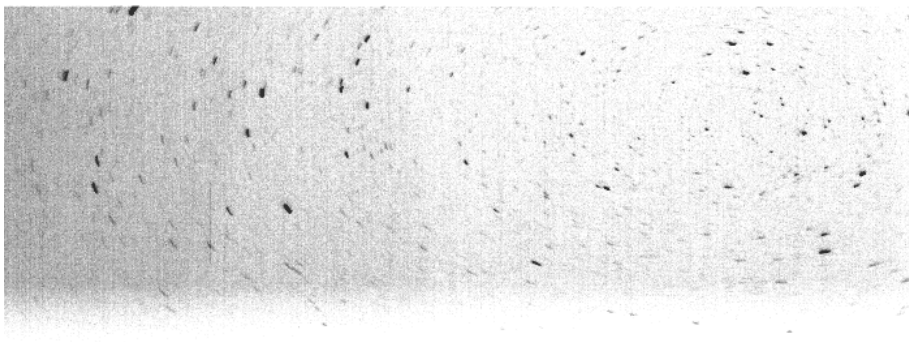

Figure 3.10: TDI compensated image at $\dot{\omega} = 4°/\text{s}$ (non-orthogonal) with $T_{int} = 0.951\text{s}$ and $N_{tdi} = 62$

As expected, it appears that full motion compensation is only achievable in one (small) region of the image.

Finally, a series of 28 consecutive attitude measurements were acquired, denoted $\underset{\sim}{\bar{A}}_i, i \in \{1..28\}$. For the entire series the following configuration was used: $\dot{\omega} = 4°/\text{s}$ (orthogonal), $T_{int} = 0.476\text{s}$, $N_{tdi} = 39$, and the time between the updates was $T_{upd} = 0.951\text{s}$. Every single attitude was successfully (and autonomously) calculated by the system.

The rotation of the CHU between each attitude measurement can be used to establish the accuracy of the system. The velocity matrix between

$\bar{\bar{A}}_i$ and $\bar{\bar{A}}_{i+1}$, denoted $\bar{\bar{V}}_i$ is found from:

$$\bar{\bar{V}}_i = \frac{\bar{\bar{A}}_i^T \bar{\bar{A}}_{i+1}}{T_{upd}} \tag{3.6}$$

introducing T_{upd} in the denominator, such that the unit of $\bar{\bar{V}}_i$ becomes [°/s] rather than [°/update]. The matrices $\bar{\bar{V}}_i$ contain both Ω and $\dot{\omega}$, where the latter can be isolated from [24]:

$$\cos 2\dot{\omega}_i = \sqrt{\frac{1 + \mathrm{tr}(\bar{\bar{V}}_i)}{4}} \tag{3.7}$$

where the function tr() is the matrix trace function. Since 28 attitude measurements exist, 27 such measurements of the angular velocity can be isolated. Individually, they can be used to derive the actual rotation velocity. In combination, they can be used to assess the total noise of the system, including attitude measurement noise and telescope drive noise. The attitude series are plotted in a worldplot in figure 3.11.

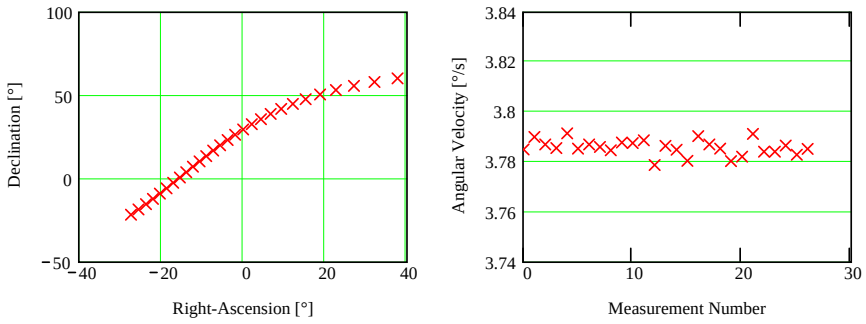

Figure 3.11: Attitude measurements at $\dot{\omega} = 4°/\mathrm{s}$, $T_{int} = 0.476\mathrm{s}$ and $N_{tdi} = 39$. The left plot shows the measurements in a worldplot. The right plot shows the measured angular velocity based on two consecutive attitude measurements in [°/s].

The standard deviation of the 27 velocity measurements is $\sigma_{\dot{\omega}} = 11\mathrm{as/s}$. Since V_i is found from two independent attitude solutions acquired T_{upd} apart, the standard deviation for the attitude measurements σ_A can be found:

$$\sigma_A = \frac{1}{\sqrt{2}} T_{upd} \sigma_{\dot{\omega}} = \frac{1}{\sqrt{2}} 0.951 \cdot 11\mathrm{as} = 7.5\mathrm{as} \tag{3.8}$$

This value is a very conservative estimation of the TDI attitude measurement performance (accuracy), since it also includes the telescope drive noise. The results obtained from the images acquired at different rates and integration periods (table 3.1) indicate standard deviations in the range of 1-2as.

3.1.5 Summary

Throughout this section, the design of a TDI star-tracker prototype has been presented. The prototype includes redesign of the CHU hardware, implementation of FPGA software for the TDI timing generator as well as configuration support software.

The TDI star-tracker is capable of motion compensation of 16 different rates about the focal plane x-axis. The supported compensation rates are selected in such a way that star-tracking can be performed at any angular rate up to 48°/s.

A limitation in the prototype was the shortcoming of the CCD to perform backward compensation. However, the successful motion compensation in the forward direction verifies the concept.

Real sky tests showed that the performance of the TDI star-tracker at high angular velocities was comparable to a non-TDI star-tracker in a non-rotating environment.

3.1.6 Recommendations for future work

It is recommended that the performance envelope of a non-commercial CCD is verified, such that compensation in both directions of the y-axis can be accomplished.

Research at the MIT Lincoln Labs has resulted in the development of an orthogonal transfer CCD, which is capable of moving the integrated charges along both axes. Such technology is of high interest for star-tracking at high rotation rates, because all rotation vectors orthogonal to boresight can be compensated for.

3.2 Case: Target Tracking

Motion characterization using attitude sensing. Motion compensation using a folding mirror and/or mechanical drives.

Operation of pointing instruments on space borne platforms face a unique class of difficulties associated with operations involving acquisition of non-distinct or moving targets. Especially for long time exposing systems, the difficulties are aggravated by the subsequent high accuracy tracking for a longer time span.

A typical pointing system for an aerospace application is built around a given instrument, of which the orientation must be controlled relative to a given target. Since the instrument is a pointing instrument, only the 2-axis orientation is of importance. The rotation about the pointing direction is usually not relevant.

The pointing system will also contain an attitude sensor that determines the current orientation of the pointing instrument. Finally, the system will contain an actuation mechanism that is capable of physically rotating the pointing instrument and/or platform.

A typical application of a pointing system is within the field of space-borne astronomical imaging, where a telescope system is mounted on a 3-axis stabilized satellite platform. By rotating the telescope it is effectively pointed towards the target. Since the mass of a typical space borne telescope is considerably high relative to the total spacecraft mass, high torques will be imposed on the platform orientation. It is therefore proposed that a folding mirror is placed in front of the telescope, such that the telescope boresight can be effectively re-oriented with a much lesser effort (§2.8.1).

3.2.1 The Bering Spacecraft

Starting from 2002 a feasible study for a deep space mission to the asteroid belt was carried out by scientists from University of Copenhagen, Technical University of Denmark and Danish Space Research Institute. The main mission objective is to increase the knowledge about the smaller asteroid population, which is not observable from the Earth. Such information is expected to provide insight about the formation and evolution of the asteroid belt [1]. Since the mission will be exploring untrodden parts of the solar system, it is named after the famous Danish explorer Vitus Bering.

The main payload is a 0.3m telescope with an EFL of 2m, and an FOV of about 1°. The 1K x 1K image sensors will ensure an image resolution

of 3.6as. The targets are automatically detected and isolated by one of the six body-mounted star-trackers and an onboard prospective target catalogue [12]. The spacecraft will be rotating slowly at 1RPH in order to maximize the supported target envelope. A folding mirror in front of the telescope is realized, both in order to point the telescope towards the prospective targets and to avoid image smearing from the rotating platform during observation. The mirror orientation will be controlled in two axes. As discussed in §2.8.1 such an implementation can point the telescope in the given direction inside a certain envelope. A residual field rotation will, however, be present for rotation vectors that are not parallel to any of the actuator axes. Figure 3.12 shows a sketch of the science telescope configuration.

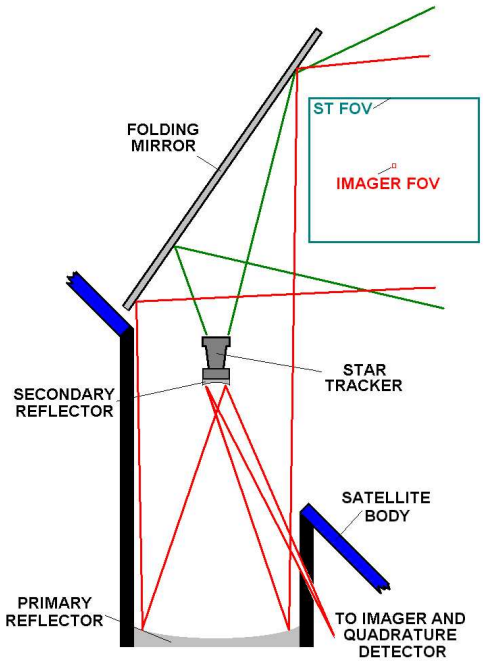

Figure 3.12: The folding mirror proposed for the Bering mission

The folding mirror shown in the figure reflects the light onto the primary mirror, which reflects the light onto a secondary mirror. This mirror is mounted on the structure via small relatively fast actuators (e.g. piezo crystals) in a tip/tilt configuration in order remove second order high frequent motion components.

The secondary mirror reflects the light through a ∼5% mirror. This mir-

ror reflects a small portion of the incoming light onto a quadrature detector, controlling the position of the secondary mirror actuators at a frequency of some 100-1000Hz. The remaining ∼95% light is focused onto a multi-spectral imager, baselined to 6 spectral bands.

The structure used for the mirror orientation control will by design raise accuracy and stability concerns. Issues like thermal strain, erosion, gearing play build-up, etc. will change the calibration. A very elegant way to avoid frequently re-calibrations is to include the folding mirror position in the attitude sensing. This technique is possible for all photon based attitude sensors.

A star-tracker CHU is therefore located on the backside of the secondary mirror structure. The mount is made such that the star-tracker boresight is largely co-aligned with the telescope boresight. This setup provides the obvious advantage that the absolute telescope attitude is determined autonomously independently on the folding mirror position. This co-alignment is illustrated in figure 3.13.

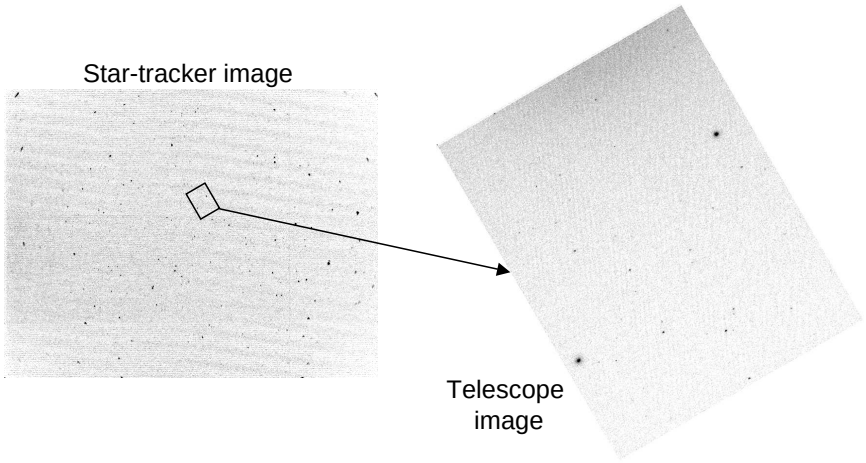

Figure 3.13: Co-alignment between star-tracker and telescope. The left image is acquired by the large FOV star-tracker, whereas the right image is acquired by the narrow FOV (1°) telescope. The location of the telescope image within the star-tracker image is marked with a rectangle

Apart from directly outputting the orientation of the science telescope, the secondary mirror mounted star-tracker serves another important task. When approached by the mirror drives, the targets will appear in the star-tracker FOV, ranging from small luminous points to larger objects. The

position of the target will be calculated by the centroid module in parallel with the star centroiding. Since the pattern matching will *not* recognize the target as being a star, it will be omitted from the attitude determination. A list of celestial positions of such objects can optionally be output from the star-tracker along with the attitude. A prospective target selection can be subtracted from a sequence of such lists based on the relative object motion. Secondly, a target discrimination based on catalogue inaccuracies is considered. A detailed description of the target detection philosophy is given by Jørgensen [12]. Since the telescope FOV is contained in the star-tracker FOV (figure 3.13), the target position can be recovered by the star-tracker as long as it is available for telescope acquisition.

Since the goal is to obtain pointing accuracies in the arc-second range (confined by the imager resolution) a three-axis inter-boresight calibration is performed between the instrument boresights. This alignment is determined autonomously on-board either after the telescope acquisition or at regular intervals. The result is a rotation matrix from star-tracker coordinates to telescope coordinates, found from combining the star-tracker output with the attitude found from the telescope image. This attitude is found using the publicly available software package AscFIT [14]. This tool determines the attitude based on a telescope image and an attitude seed. The AscFIT performance is well established and does not require additional validation.

In addition, the drive axes will change as function of temperature, erosion, from launch load impacts, etc. An automated calibration procedure to establish the motion of the telescope boresight as function of the motion in the individual drives must therefore be implemented as well.

Finally, since tracking of very faint targets is planned, they will, in turn, be too dim to be detected by the star-tracker. They will, however, still be observable for the telescope. A relative velocity model can therefore be generated while the target is still visible for the star-trackers. This model can serve as input to an open loop tracking. The observation period for each target is hereby extended substantially.

3.2.2 Concept Verification

The folding mirror drive control signals are highly similar to the corresponding telescope drive control signals, and can be obtained from these by a simple transformation. The folding mirror control using a star-tracker can therefore be mimicked by a telescope control using a star-tracker.

On-ground controlling of a science telescope using a star-tracker has been exercised previously. Jørgensen [15] describes a setup, controlling the

University of Hawai'i 24 inch equatorial mounted science telescope. The telescope was guided in a closed loop in the setup. The star-tracker was mounted on the secondary mirror structure. However, the telescope was mounted in a polar orientation such that the actuation axes (right-ascension and declination) were considered determined.

In order to verify the concept of a telescope in an unknown reference frame, experiments were carried out controlling an unaligned telescope. For this purpose the University of Hawai'i operated 20" equatorial mounted telescope was kindly made available. This particular telescope is generally used for public outreach, wherefore it is located on a custom built cart for rapid relocation. The telescope can therefore be placed in an unaligned position by simply turning the cart. Again the star-tracker was mounted on the secondary mirror structure, as shown in figure 3.14.

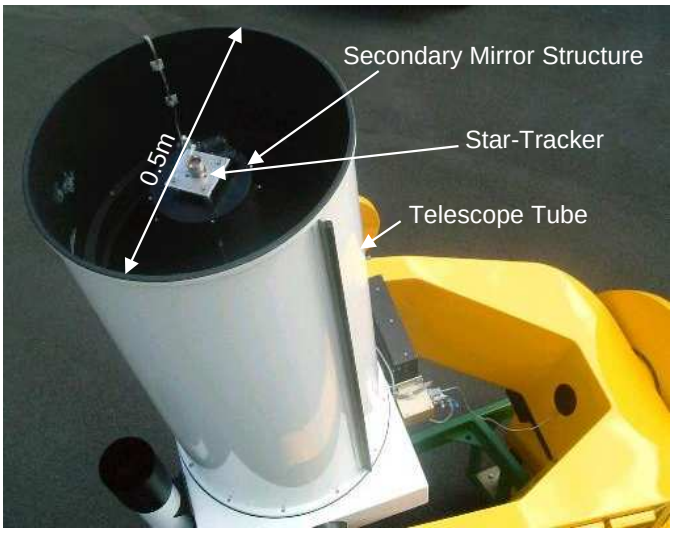

Figure 3.14: Test setup for the target tracking concept verification. An ASC star-tracker is mounted on the secondary mirror structure of the UH-20" outreach telescope.

In order to be able to perform the verification, a small software console was implemented, referred to as *AscDFM*. As input to AscDFM was the measured telescope pointing (given by the star-tracker). Control signals dictating the requested drive velocities were output, interfacing to a separate telescope control console. By a customized Windows interface on the AscDFM console, selection of automatic actuator alignment, tracking and

guiding could be made. The control laws of the system was implemented carefully in order to avoid control loop instabilities and to minimize the response time.

Actuator Characterization

The telescope drive axes for the Bering mission will be coarsely calibrated from ground, but since the possibility of in-flight calibration exists relaxation can be put on the actuation drive stability. This in-flight calibration can be performed on a regular basis by the secondary mirror mounted star-tracker using the following automated procedure:

1. The on-board attitude control system is put in "quiet" mode, such that no attitude maneuvering or maintenance is performed.
2. The rotational state of the spacecraft is recorded by the star-tracker
3. A motion in the first mirror drive axis is executed.
4. The rotational response is recorded by the star-tracker. After compensation for the platform rotation, the attitude change response can be determined.
5. Step 3-4 is repeated for each of the mirror drive axes

In order to verify the concept, the automated drive characterization procedure was implemented for the 20" telescope. The drive axes was presumed to be orthogonal, wherefore only the right-ascension drive axis was established. In addition, the "platform" motion, i.e. the rotation of the Earth, was considered known.

The performance of the characterization was evaluated, by a following open loop tracking. The result will be presented in the following section.

Open Loop Target Tracking

After characterization of the current system motion and drive orientations, an open loop tracking was performed. The selected target was the current star-field while the sidereal rotation of the Earth mimicked the target motion model.

At a frequency of 2Hz, the position of the target 1s later was extrapolated from the model. The telescope drive motion required to achieve this position was found and decomposed into the single drive axes.

The position of the target could be measured directly from the star-tracker, simply as the attitude output. It is important to note that the star-tracker in this test configuration is used only to establish the target position, i.e. the result of the control. It is *not* included in the control loop. The star-tracker measured the target position continuously for two minutes at a frequency of 2Hz, yielding 240 measurements. The pointing results and the decomposed control velocities are shown in figure 3.15.

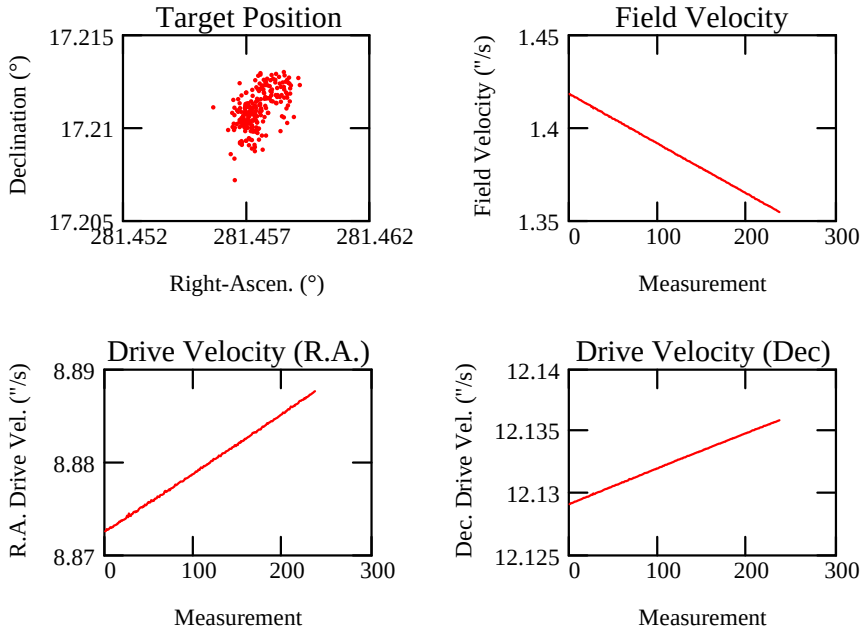

Figure 3.15: Results from the open loop target tracking test. The upper left graph shows a worldplot of the celestial position of the target during the two-minute test sequence. The upper right graph shows the residual field velocity. The two lower graphs show the control velocities commanded to the telescope drives during the test sequence.

Since the first measurement in the series, $\bar{p}_1$, is selected as the target position, the pointing accuracy can be measured as the angular deviation between the successive measurements $\bar{p}_i, i > 1$ and $\bar{p}_1$. This pointing error is plotted in figure 3.16.

The graph shows a pointing drift of about 0.1as/s over the observation period. Compared to the true target motion of about 15as/s, the relative motion has been decreased by a factor of 150. This is unfortunately not suffi-

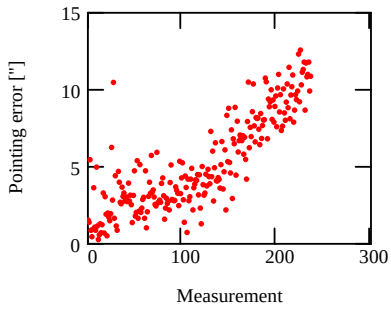

Figure 3.16: Pointing error for the open loop test. The residual drift of 0.1mas/s can be seen as a trend in the measurements.

cient for the long integration periods foreseen. The source of the inaccuracy can reside in two locations: The target motion model or in the actuator characterization. Since the target motion model is quite well established (the Earth sidereal rotation), the inaccuracy must be located in the drive characterization. The drift indicates either an error of 0.5° in the drive vector characterization, or a 0.7% error in the drive velocity determination.

Since the target motion is not parallel to any of the two drive-axes, a residual field velocity is present, as given in figure 3.15. The total field rotation within a telescope image acquisition is found by integration of this field velocity over the acquisition period.

In order to establish the accuracy of the individual measurements, the drift originating from the pointing error must be removed. Since all the measurements in the series are calculated independently of each other and the observed motion is relatively small, the accuracy of one measurement $\bar{p}_i$ can be found simply be comparing it with the following measurement $\bar{p}_{i+1}$. The pointing error ϵ_i is found from:

$$\epsilon_i = \frac{\arccos\left(\bar{p}_i \cdot \bar{p}_{i+1}\right)}{2} \tag{3.9}$$

where the denominator of 2 is inserted due to the pointing error being distributed between two measurements. The standard deviation of the pointing errors σ_ϵ is found from:

$$\sigma_\epsilon = \sqrt{\mathrm{E}[\epsilon^2]} = \sqrt{\frac{1}{N}\sum_{i=1}^{N-1}\left(\frac{\arccos\left(\bar{p}_i \cdot \bar{p}_{i+1}\right)}{2}\right)^2} = 1.85\mathrm{as} \tag{3.10}$$

where N is the number of measurements. It should be emphasized that this accuracy estimate is based on the assumption that the pointing errors are uncorrelated.

The test shows that the open loop tracking is certainly possible for short integrations (< 1 min) with the applied setup. The short-term accuracy in the range of a few arc-seconds is comparable with the star-tracker performance for the night of the test. For longer acquisitions a more accurate drive characterization is needed.

Closed Loop Target Tracking

Inaccuracies in the target velocity model will eventually lead to an inaccurate pointing and/or image smearing. As long as the target under observation is luminous enough to be detected by the star-tracker, its position is directly measurable and determined continuously by the star-tracker. Applying the measured rather than the modelled position to the drive control is preferred, whereby a bias-free observation is achieved.

During the test sequence, three arbitrarily selected target positions on the celestial sphere were commanded. A dwell time of ∼90s at each target was programmed, before the next target was commanded. The star-tracker measured the current telescope pointing position at 2Hz and calculated the required motion to achieve the target. This motion was finally decomposed into the two drive axes and then actuated.

Once again the position of the target is measured directly from the star-tracker. The test results are shown in figure 3.17.

The error in the lower graph of the figure shows a drift-free control, as soon as a target is approached. The two target re-commandings are clearly visible as two discrete pointing error jumps that decrease as the targets are approached. By isolating a subset of the data excluding the target approach, the closed loop tracking accuracy can be directly measured. The standard deviation of the pointing errors σ_ϵ is determined from:

$$\sigma_\epsilon^2 = \mathrm{E}[(\arccos(\bar{p}_i \cdot \bar{p}_t)^2)] \tag{3.11}$$

where $\bar{p}_i$ is the i'th measurement and $\bar{p}_t$ is the target position. The accuracy of the three target acquisition are summarized in table 3.2.

σ_ϵ is slightly higher for the second target, however all pointing accuracies are within the required range of the planned imager resolution of 3.6as.

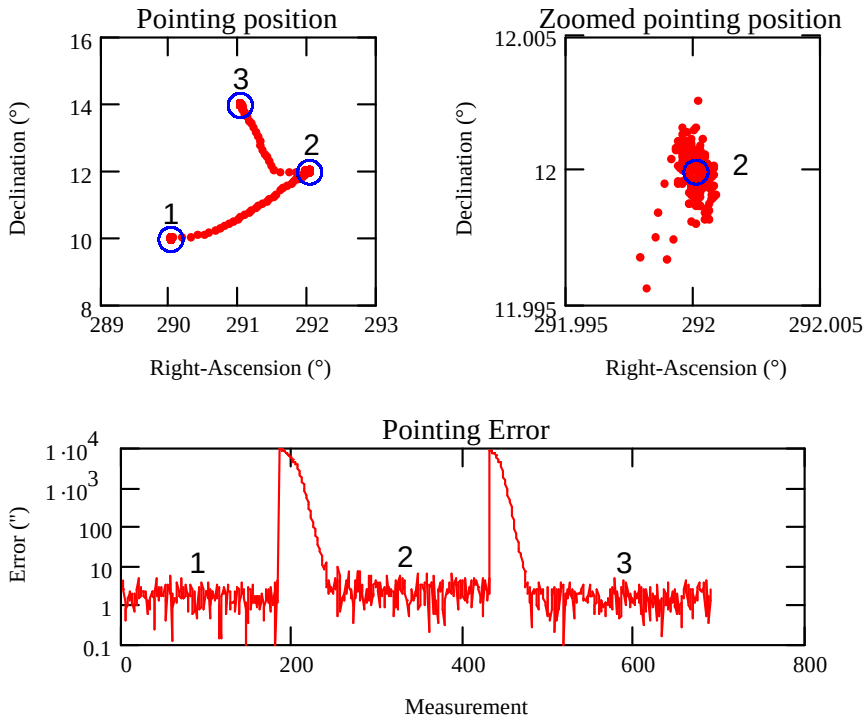

Figure 3.17: Results from the closed lop target tracking test. The upper left graph shows a worldplot of the position of the telescope during the entire measurement period. The three selected targets are marked with circles. The upper right graph shows a zoom of the second target. The lower graph shows a logarithmic plot of the error between the target position and the observed positions.

3.2.3 Summary

Throughout this chapter a part of the Bering mission feasibility study has been presented. The rotating platform will intrinsically cause smearing in imaging from the satellite telescope.

A solution including a movable folding mirror in the optical pathway is presented. The mirror drive inaccuracies are removed by placing a star-tracker in the same optical pathway. Closed loop control of the mirror can therefore be achieved.

Three parts of the concept have been verified using a mobile science telescope as test platform. The actuator characterization step was verified

Table 3.2: Pointing accuracies during closed loop tracking of three targets

Target - RA [°]	Position Dec [°]	Dwell time [s]	Accuracy σ_ϵ ["]
290.0	10.0	87	2.02
292.0	12.0	91	3.03
291.0	14.0	102	1.89

by establishing the absolute telescope drive axis in an unaligned setup. Open loop target tracking was conducted (with a small drift) using the sidereal rotation of the Earth as motion model. Finally, closed loop target tracking was performed, again using the Earth rotation as the moving target.

3.2.4 Recommendation for future work

In order to verify the full Bering target tracking concept, a number of subjects should be further investigated:

- The target motion model should be autonomously determined. This task is aggravated by the diversity in relative velocity and intensity of the targets.
- The actuator characterization was limited to the direction of one drive for the tests described here. The second drive axis was considered orthogonal to the first axis, and the two drive velocities were considered established. A test containing full characterization including position and velocity of all (both) drive axis should be conducted.
- A test where the pointing direction is controlled by a folding mirror rather than the telescope drive should be conducted.

3.3 Case: Two-Stage Star-tracking

Motion characterization using high accuracy attitude sensing

The ever increasing demands for accurate instrument motion compensation impose similarly increasing demands for fast, robust and accurate attitude sensing. In addition, since space applications only allows for a limited supervision (when the spacecraft happens to pass a ground station), the interest for autonomous instrumentation is growing.

For absolute (inertial) attitude reference, the modern autonomous star-trackers are by far the most accurate autonomous sensors, where the highest performing trackers are capable of determining the attitude with an accuracy down to 1as. A higher accuracy of the individual centroid is achievable using a smaller FOV optics, however the constellation observed within the FOV will then not be guaranteed to be identified uniquely. A successful solution of the Lost In Space (LIS) problem, where the orientation is found without a priori knowledge, is not guaranteed.

One solution to this limitation is to perform the star-tracking in two stages using two different FOV optics. The first stage has a short focal-length yielding a wide FOV, whereas the second stage has a long focal-length yielding a narrow FOV. The two stages are mounted in an optical bench, such that their mutual orientations are fixed relative to each other. This inter-calibration is presumed to be established up to a certain accuracy before operation and is not discussed further here. Such a setup is sketched in figure 3.18.

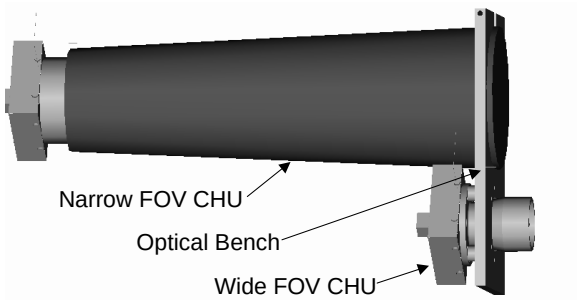

Figure 3.18: A two-stage star-tracker mounted on an optical bench

Image integration of the two stages are done in parallel and fully synchronous, resulting in two star images referring to the same point in time.

In the first stage, the star-tracking is performed nominally with an accuracy of 1as. Using images from this stage the LIS problem can be solved for all possible orientations. This "crude" attitude solution serves as a seed to the second stage (high resolution) attitude determination. The functionality is illustrated in an architectural diagram in figure 3.19.

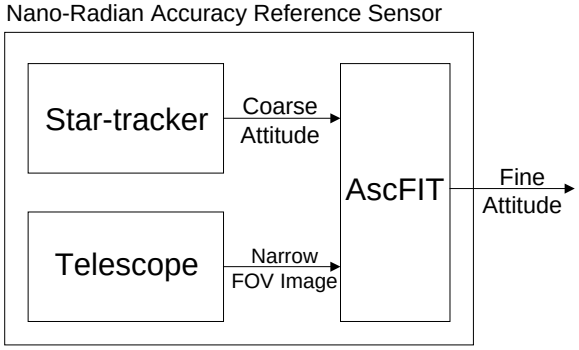

Figure 3.19: Architectural description of a two-stage star-tracker

In figure 3.19 the AscFIT [14] program is introduced, which is a publicly available software package capable of determining the 3-axis attitude of astronomical images when supplied by an approximate seed. The package has been developed in a cooperation between Technical University of Denmark and University of Hawai'i. It is used for attitude recovery by astronomers at all levels, e.g. by amateur astronomers, by professional astronomers at the University of Hawai'i controlled 2.2m telescope at Mauna Kea, Hawai'i and at the Caltech controlled telescopes at Mount Palomar.

In it's current form, AscFIT operates on the star catalogue supplied by the United States Naval Observatory (USNO), whereas the centroiding is performed using the open source software package SExtractor. Finally, the pattern matching is based on the same techniques used within the ASC pattern matching software.

3.3.1 Analysis

The accuracy of the second CHU stage depends primarily on the following parameters:

- The *centroiding accuracy* is the accuracy at which the centroid can be determined. For the narrow FOV foreseen for the second stage, the

optical aberration and distortion will be minimal, wherefore an accuracy within 0.2 to 0.3 pixel is achievable using conventional centroiding algorithms.

- The *number of stars*. By using several stars a hyper accuracy attitude solution can be formed. The final accuracy is proportional to the square root of the number of stars included.

- Finally, the *catalogue accuracy* is addressed. Since the attitude determination is based on these reference positions, the deviations must be small compared to the targeted accuracy.

In order to estimate the attitude accuracy based on the centroiding accuracy, the following observations are made: The attitude accuracy is decomposed into a pointing accuracy (about the x- and y-axes) and a roll accuracy (about the z-axis). The number of pixels $N_{2\pi}$ used to describe a full 2π revolution about any of the axes is sought. When this number is established, the angular accuracy about the given axis ϕ can be found from:

$$\phi = 2\pi \frac{c}{N_{2\pi}} \tag{3.12}$$

where c is the centroiding accuracy having the unit [pixel]. The number of pixels describing a full revolution about the x-axis is found from the imager y-axis FOV $2\beta_y$, such that

$$N_{2\pi,y} = N_y \frac{2\pi}{2\beta_y} \tag{3.13}$$

where N_y is the number of CCD pixels along the y-axis. The angular accuracy about the x-axis ϕ_x can now be resolved:

$$\phi_x = 2\beta_y \frac{c}{N_y} \tag{3.14}$$

Analogously, the angular accuracy about the y-axis is:

$$\phi_y = 2\beta_x \frac{c}{N_x} \tag{3.15}$$

Finally, the angular accuracy about the z-axis is found. The number of pixels to represent a full revolution $N_{2\pi,z}$ is proportional to the pixel distance to the origin $r = \sqrt{x^2 + y^2}$ such that $N_{2\pi,z} = 2\pi r$. Both $N_{2\pi,z}$ and

r is given in unit [pixels]. From insertion into eq. 3.12 the angular accuracy about the z-axis ϕ_z can now be determined:

$$\phi_z = \frac{c}{r} \tag{3.16}$$

It appears from eq. 3.14 and eq. 3.15 that the obtainable angular accuracies are directly proportional to the FOV of the imager. It also appears from eq. 3.16 that the angular accuracy about the z-axis is independent of the FOV, since r is given in pixels. It is therefore concluded that adaptation of the second narrow FOV optical stage will only improve the accuracy about the x- and y-axes (the pointing accuracy). The accuracy about the z-axis (the roll accuracy) will remain unchanged.

The selection of the narrow FOV optics will directly improve the angular accuracy - with the penalty of a higher mass. An EFL of 250mm appears to be a rasonable mass-performance tradeoff such that the resolution will be 12.5 times higher than the standard ASC CHU's. On the other hand, such optics can be realized with a reasonable low mass, which is highly beneficial for a space-borne attitude sensor. A rectangular FOV of $1.5^\circ \times 1.1^\circ \approx 5 \cdot 10^{-4}$sr is hereby achieved (approximation is valid for small angles).

Secondly, the visual sensitivity is considered. The FOV of a 250mm optics will for the ASC CCD be $\sim 1^\circ$ and will cover only 39ppm of the celestial sphere. In order for the attitude to be determined with a sufficient accuracy and robustness, at least 10 stars must be present and recognized within the field of view. The minimum number of stars in the onboard catalogue needed for meeting this number is 10/39ppm = 260k stars. On the other hand, that attitude can be determined with only 5 stars, but the accuracy will be decreased.

The stars are unfortunately not dispersed homogeneously over the celestial sphere. Approximately half of the stars which can be individually discerned at a given visual magnitude are located close the equatorial plane of our galaxy, the Milky Way. The number of stars observed within the imager FOV (at a given sensitivity) is therefore highly dependent on the line of sight and may vary several decades. The possibility is therefore to either:

1. carry an onboard catalogue with a varying sensitivity, such that a higher sensitivity is used in the lower star density regions. Minimum catalogue storage and search time consumption is thus achieved.

2. carry an onboard catalogue with a high sensitivity in all regions. The catalogue storage requirements and search time will be higher, however perfectly valid and bright stars in rich regions will not need to be discriminated. A higher accuracy in these regions is hereby directly achieved.

Since the modern technology is striving for higher capacities at smaller components, solution number 2 is preferred, such that the second stage optics soon will become the limiting "bottle neck".

Figure 3.20 shows a star density map of the celestial sphere at a visual magnitude $m_V = 10$ compiled from the Tycho-2 star catalogue. The applied bins are circular with a radius of 0.75° simulating a circular FOV of $5{\cdot}10^{-4}$sr.

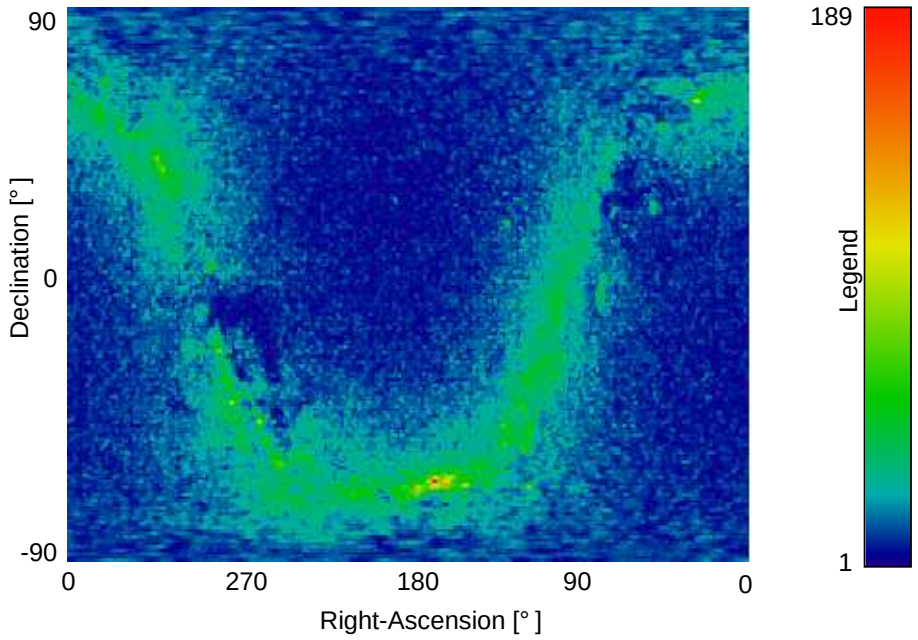

Figure 3.20: Star density map showing the star distribution. The densities are based on a 1° circular FOV with a sensitivity of $m_V = 10$. The higher densities are showed brighter than lower densities, such that the milky way is clearly visible as a high density (bright) sinusoidal trace.

It can be observed from the density map in figure 3.20 that the number of stars within a bin varies from 1 to ∼200. In order to evaluate the dis-

tribution, a histogram over the occurrences can be created. By normalizing the histogram it becomes a probability density function over the number of stars within a bin. This probability density function p and the probability distribution function P are shown in figure 3.21, together with a performance map, illustrating the performance as function as pointing direction.

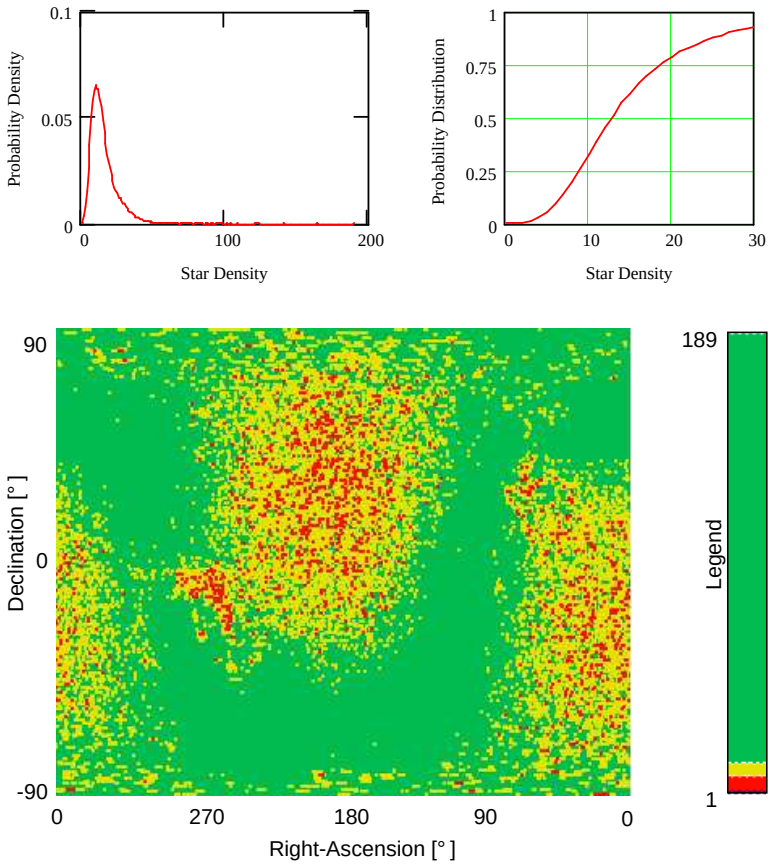

Figure 3.21: Upper left: Star density probability. Upper right: Zoomed part of the star density distribution. Lower: Thresholded density map, marking areas with no performance in red, limited performance with yellow and nominal performance with green.

The probability of having 10 or more stars within the field of view can

be found either from:

$$1 - P(10) = 1 - \sum_{n=10}^{\infty} p(n) = 0.673 \tag{3.17}$$

I.e. at 67.3% of the celestial sphere, the attitude can be determined with the accuracy foreseen (or higher). At the remaining portion, the accuracy will be reduced. At a very small portion of the sphere (5.5%), high accuracy attitude determination will be impossible with the selected sensitivity.

Since the sensitivity is directly proportional to the optics aperture (area), the required aperture can be found from similarity. It is proven that stars up to $m_V = 8$ can be isolated and centroided with a reasonable S/N ratio with the applied star-tracker CHU design. Increasing the sensitivity x orders of magnitude will require an aperture increase of 2.512^x, where 2.512 is the base number for visual magnitudes. A 2 order increase will therefore require a $2.512^2 = 6.3$ times larger aperture area, or a $\sqrt{6.3} = 2.5$ times larger aperture diameter. Since the current CHU aperture (diameter) is 2.5cm, a 6.3cm aperture is implemented.

The AscFIT package is prepared for a large community of astronomical applications. The centroiding is based on the SExtractor package, which offers centroiding with numerous possibilities such as compensation for background non-uniformities, morphological categorization of objects, etc. These capabilities are not relevant to star-tracking, wherefore a simpler (and faster) centroider is implemented.

Secondly, the AscFIT reference star catalogue is based on the USNO catalogue. This reference catalogue is complete to very high star sensitivities, but the accuracy is limited (primarily due to a poorly determined star proper motion). The Tycho-2 catalogue has a much higher proper motion accuracy, but is only complete to a limited sensitivity ($m_V = 12$). The second stage star-tracking is therefore based on a subset of this catalogue containing $\sim 350,000$ stars.

3.3.2 Test Results

A prototype setup was realized where the two optical stages were mounted largely co-aligned in an optical bench. The first stage was based on a standard (20mm, F/0.8) ASC star-tracker optics, while the second stage was based on a 250mm, F/4 lens, realizing a 1° FOV with $m_V = 10$ sensitivity. The setup, mounted zenith pointing, is shown in figure 3.22.

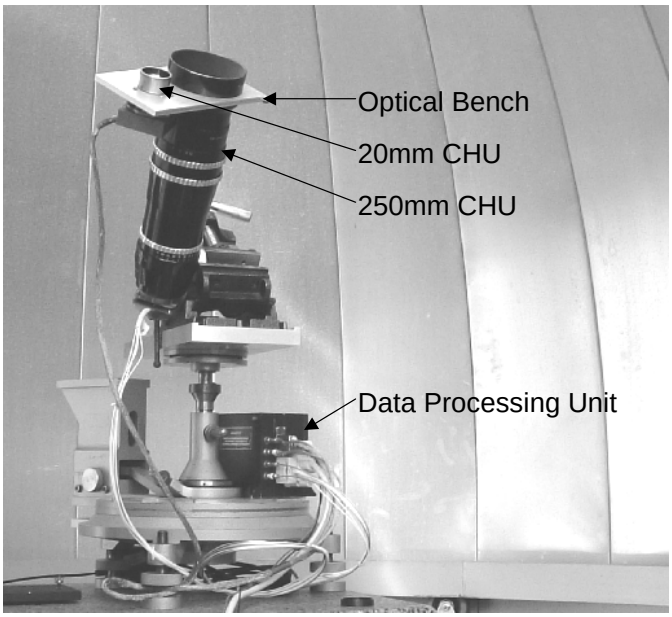

Figure 3.22: Two-stage star-tracker test setup. The two CHU's mounted on the optical bench is shown together with the DPU.

The boresight inter-calibration was performed by pointing the telescope system towards a well known celestial constellation that could easily be discerned from both systems. For this purpose, the Pleiades constellation was selected, yielding two images: A high and a low resolution. The images are shown in figure 3.23

In order to reduce the atmospheric distortions, a local zenith pointing orientation was selected. Two measurements series were recorded: One covering a rich star-field (averaging 40 stars) with the RA axis aligned with the x-axis, and one covering a meagre field (averaging 8 stars) with the declination axis aligned with the y-axis. Both series were recorded from the Technical University of Denmark located at 56° latitude.

In order to verify the accuracy, two different methods were applied:

1. Since the setup pointing is fixed, the observed star-field will drift at a well-defined rate corresponding to the rotation of the Earth. If this motion is removed from the measurements, the pointing must remain stable. The system accuracy determined from the deviation from this

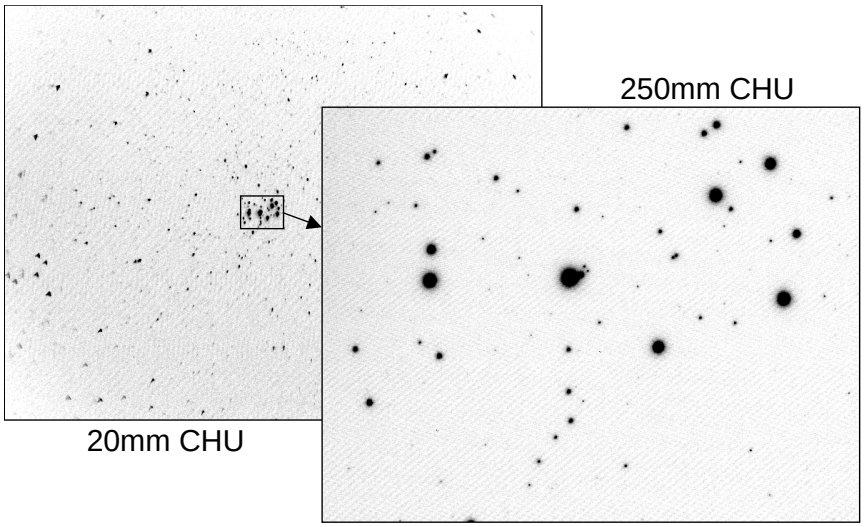

Figure 3.23: The two images used for boresight inter-calibration. The high resolution image is shown as a zoom of the low resolution image.

pointing is denoted σ_p:

$$\sigma_p^2 = \sigma_{\alpha'}^2 \cos^2\delta + \sigma_\delta^2 \tag{3.18}$$

where δ and α' are the declination and the sidereal adjusted right-ascension respectively. Small angles are presumed.

2. The image centroids are linked to the star-catalogue using a least-square fit. The RMS deviation between the star-catalogue and the centroids, the residual ξ, can be used as a measure of the obtained accuracy, denoted σ_r:

$$\sigma_r = \frac{\xi}{\sqrt{N_{st}}} \tag{3.19}$$

where N_{st} is the number of stars.

The obtained accuracies have been calculated using both methods. They are summarized in Table 3.3:

It should be noted that the performances are measured in terms of relative accuracy by the methods described (the instrument has only been tested against itself). In addition, lower frequency terms such as relativistic aberration effects have not been compensated for (even though the star-tracker contains this feature).

Table 3.3: Obtained accuracies for high accuracy star-tracking

Star-field	σ_p	σ_r
Rich	367mas	266mas
Meagre	739mas	836mas

3.3.3 Summary

Throughout this section the thesis work on a high accuracy motion determination using a two-stage star-tracker has been presented. The resolution ratio between the two stages was 1:12.5, and the sensitivity ratio 1:6.3 corresponding to two orders of magnitude.

The performance has been verified on a rich as well as a meagre star-field, obtaining relative pointing accuracies ranging from 300mas to 800mas. The measured performance is a little lower than what was expected, based on the centroiding accuracy foreseen and the number of stars expected for processing.

The centroiding accuracy is somewhat limited by the atmospheric seeing at the test site. A slightly improved performance is expected, if the measurements are repeated at a high-altitude astronomical site.

3.4 Case: Star-Tracker Radiation Handling

Source and drain field characterization using feature discrimination

When a CCD sensor is subjected to ionizing radiation, it's photosensitive structure can, depending on the nature of the radiation, be adversely affected. The effect of such radiation on a CCD is somewhat different from the effects measured on regular electronics wherefore they are described in some details below. Generally the CCD structure is relatively resilient to ionizing gamma and X-ray, i.e. no or little degradation is measurable even after substantial total doses. Also irradiation with energetic leptons such as electrons are handled well by the CCD structure. Only in the case of energetic baryons high sensitivity is experienced. Even light baryons such as protons may produce substantial damage to the CCD or degrade the image from it. Consequently the dominant detrimental effects from energetic baryons are described below.

1. As the CCD substrate is penetrated by the impinging energetic baryon, which is highly to fully ionized, lattice electrons are liberated by interaction between the positively charged particles and the silicon structure. The number of electrons liberated depends on the linear energy transfer (LET) characteristics of the incoming ion, its energy and the substrate. The electron-hole pairs thus generated from the baryon impact, are indiscernible from the normal photon-generated electron-hole pairs. It is therefore impossible in such an environment to evaluate, whether an integrated charge within an image pixel stems from a photon from the observed target or a particle irradiation. The only marked difference is, that each photon only liberates Qe electrons (Quantum Efficiency, Qe < 1), whereas the baryon may liberate several thousands of electrons along its path through the CCD. When the image integration phase is terminated, all liberated electrons, disregarded the nature of generation, is shifted out of the CCD. The ionization charges generated by a single particle impact will therefore *not* be present in the subsequent image integration. In a steady irradiation scenario, a variable number of impacts will therefore appear in random pixels in each image and disappear in the following image. The motion regime implemented by this phenomenon is therefore a *source and drain* motion regime. (§2.5.5).

2. At rare occasions the incoming energetic particle will collide a substrate nucleus. A consequence of such a collision is the introduction of

a small displacement damage in the silicon structure. Such displacements will change the band-gap energy levels for the atoms around the displacement such that the number of thermal generated electrons are increased. I.e. such sites in the silicon will act as bridges for liberation of valence electrons to the conduction band. The result of this effect to the image being acquired is, that the number of thermal electrons in the area around the dislocation will be integrated into a surplus charge of a specific pixel. Since the generation rate is proportional to the available thermal energy, this surplus charge is exponentially growing with the silicon temperature. The surplus thermal charge is also depending on the incoming particle energy as well as the dislocation centre location(s) within the substrate. When the image integration is concluded, the integrated charges are shifted out of the CCD. Since the displacement damage is permanent, these charges will be present in the affected pixel in all subsequent images. Because of the limited range of recoil particles in the silicon, the individual damages will typically be confined within a single pixel. Since the dislocation represent a region within the silicon lattice with elevated energy levels, the damaged substrate structure may regenerate, at least to some extent, over time by simple stress release mechanisms of the lattice. This regeneration rate is however infinitesimal when compared to the integration periods considered. The generation effect is often referred to as *annealing*.

If a dark image is acquired (i.e. an image with no photon irradiation), the charges stemming from a particle impact will appear as a small luminous dot dispersed over only one pixel after readout. Since it appears as a bright spot, such a phenomena is often referred to as a *hotspot*. The hotspots of type 1 is referred to as *transient hotspots* while type 2 is *static hotspots*. The relationship between the luminosity/population and the integration period is summarized in table 3.4.

Table 3.4: Relationship between the luminosity/population and the integration period T_{int} for static and transient hotspots

	Luminosity	Population
static	$T_{int}\times$ generation rate	accumulated number of impacts
transient	linear energy transfer	$T_{int}\times$ impact rate

Common for the two types of hotspots is the dependency of T_{int}. The static hotspot luminosity and the transient hotspot population are proportional with the integration period. The generation of hotspots will therefore have the highest impact for low-light applications in two aspects: 1) Because only a small part of the sensor dynamic range is used, the luminosity may be comparable to the objects to be measured; 2) because the relatively high integration periods required by the low-light application will increase both the static hotspot luminosity and the transient hotspot population.

The inconvenience from this phenomenon is particularly obstructive to point object based low-light applications, such as star-tracking. The hotspots effectively producing luminous image dots appear very similar to the image projection of stars.

A related problem is introduced, when a true image object (a star) is located in the same image region as a hotspot. The following star projection deformation will consequently bias the star position leading to an inaccurate centroiding.

In particular, these effects were experienced on the DTU star-trackers [13] on-board the ESA SMART-1 satellite destined for the Moon using electric propulsion (EP) [16]. Due to the very low EP engine thrust a slow orbital altitude increase was realized. At the early mission phase the satellite was therefore passing the van Allen belt twice pr. orbit. In this particular region in an altitude ranging from ∼2000-4000km high energetic protons are trapped by the Earth's magnetic field [9]. At a later phase the orbit perigee had been raised to ∼2000km causing a constant appearance inside the belt for up to 15 minutes/orbit. Please refer to [9] for a description of orbital theory and [16] for a star-tracker performance summary during passage of the radiation belts.

The result was that typically 300 transient hotspots pr. image integration were observed during the belt passages. This number must be put in contrast to the typically 40 (photon generated) star projections pr. image.

At the SMART-1 trajectory, there is an orbital variation of the CCD sensor temperatures depending on the spacecraft pose and the geometry between the Sun, the Earth and the spacecraft. Since the static hotspot luminosity is highly dependent on the temperature, and the detection threshold is based on a certain luminosity, a variable number of this class of hotspots is observed. This variation ranges from 10 up to 10,000 pr. image at the hottest sensor environments. These numbers must also be put in contrast to the typically 40 stars observed within an image.

From the above it appears that radiation damages are posing a sizable challenge to star-tracking. Active sensor cooling is a possibility to limit the

number of static hotspots, but this type of cooling adds system complexity to the spacecraft and consumes a considerable amount of power. Furthermore, the appearance of larger thermal gradients will lead to thermal stress, effectively introducing measurement biases. Increased radiation shielding is another possibility, but the additional amount of mass needed is generally not desired for space applications due to increased launch costs and complexity. Finally CCD radiation hardening techniques exist, but the performance in terms of radiation tolerance is limited and rarely sufficient. An alternative solution to this problem is therefore of a high value. Such a solution has been developed as part of this dissertation work.

3.4.1 Analysis

A highly cost effective alternative to the above mentioned mitigation strategy is if the hotspots can be reliably discriminated from the true objects during the image processing or analysis step. For this purpose, the different characteristics that apply to a hotspot and a star must be investigated:

- The static hotspot luminosity is highly temperature dependent. Since the CCD temperature is usually measured for house-keeping purposes, this dependency can be directly modelled, such that an accurate centroiding can be achieved.
- Since the observed stars are effectively point sources, the projected image will be equal to the PSF of the lens. The image effects stemming from the radiation damages do not obey this PSF. Knowledge about the expected shape of an imaged star as well as the expected hotspot effect can be used for the discrimination.
- Since the static hotspots are permanent damages of a specific area of the CCD (i.e. a specific pixel), bookkeeping of the damaged pixels can be used for the discrimination.
- Since the transient hotspots appear in one image only, they can be identified and removed by a simple subtraction of two subsequent images.
- Since the hotspot is confined to a single CCD cell, a hotspot centroiding will result in a centroid position in the center of the pixel.

The characteristics described above have different computational requirements. A solution is therefore sought, requiring a minimum computation

load, still maintaining a high discrimination success rate. A minimum data latency and a maximum reliability is hereby ensured. The optimal solution will require an application specific combination of several of the discrimination techniques described.

3.4.2 Results

One of the advantages of the ASC is the possibility of in-flight debugging. The processed data and derived intermediate results can be dumped after all essential phases: Acquisition, object segmentation, centroiding and outlier discrimination. This functionality was used onboard the SMART-1 satellite mission to verify the in-flight functionality of the hotspot discrimination.

An end-to-end test of the filters was carried out by conducting a comparison between the images acquired by the cameras and the derived attitude information. A series of "hot" images were acquired with a CCD temperature of up to 20° after a radiation dose of $\sim$ 1kRad. This temperature was the highest reached during that period. One of these images is shown in the upper left of figure 3.24, where the difficulties of descerning stars are obvious. To the lower left is shown a zoom of a small area.

Following the hotspot identification of 4516 hotspots above the detection threshold, they are removed from the image by subtracting the derived hotspot intensity from the affected pixels. The following hotspot filtered image is shown to the right in figure 3.24, where the stars now clearly appear.

Following a standard ASC star-tracking procedure, the attitude is trivially found to: $(\alpha = 307°, \delta = -71°, \theta = 190°)$. The objects not tracked as hotspots are visible in figure 3.25, where the recognized stars are marked with circles and the residual unknown objects and rejected stars are marked with rectangles. The size of the circles marks the deviation between the centroided position and the catalogue position.

As a result of the implemented hotspot discrimination techniques, the following operation was observed:

- The star-trackers operated nominally during the Van Allen belt passages. An expected negligible increase of the number of centroided objects passing the filters was observed. This increase originates from transient hotspots falsely being reported as stars. This number was well within the instrument margin to ensure proper operation.

- When the star-trackers were operated in a hot environment, a decrease in the number of true objects passing the filters was observed. This decrease originates from stars, falsely being discriminated as being static

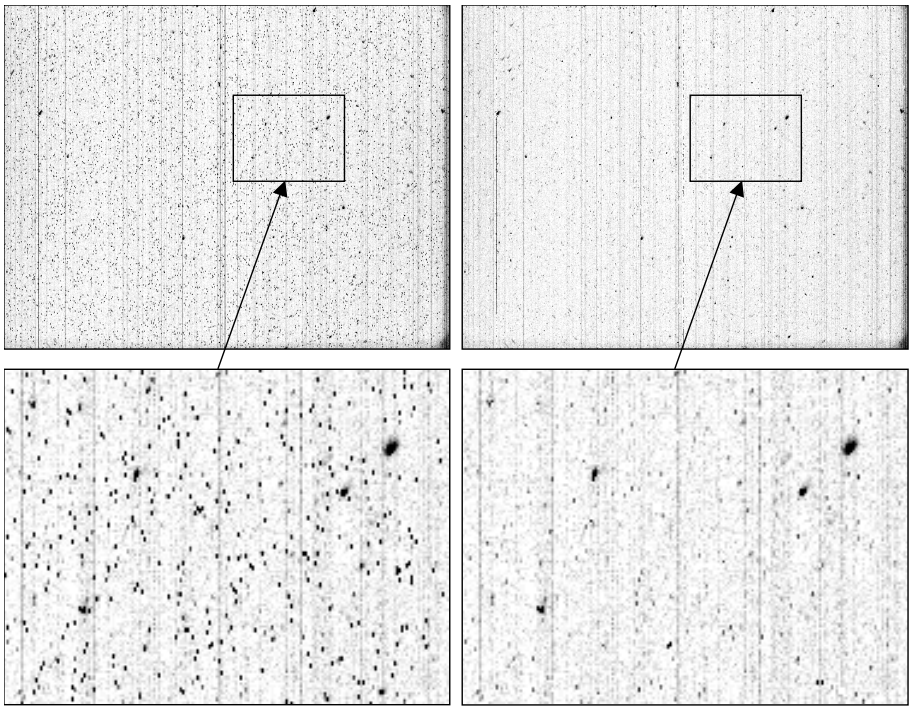

Figure 3.24: High temperature image acquired from the SMART-1 satellite mission. The static hotspots obtained from the $\sim$ 1kRad radiation dose is visible as small dark dots (inverted image) in the left image. The stars are difficult to discern by a visible inspection. In the right image a hotspot discrimination has been applied, such that the stars are easily discernable.

hotspots. At celestial regions with very few stars, attitude determination was occasionally found to be rendered by too few identifiable stars to allow reliable pattern recognition.

The performance of this filter bank has brought a considerable attention inside the field of aerospace, and has been officially recognized and emphasized by ESA.

To further investigate the performance and in order to confirm the operation for another satellite mission, a ground test was performed using a hotspot discrimination technique similar to the combination implemented for SMART-1. The static and transient hotspot population was carefully

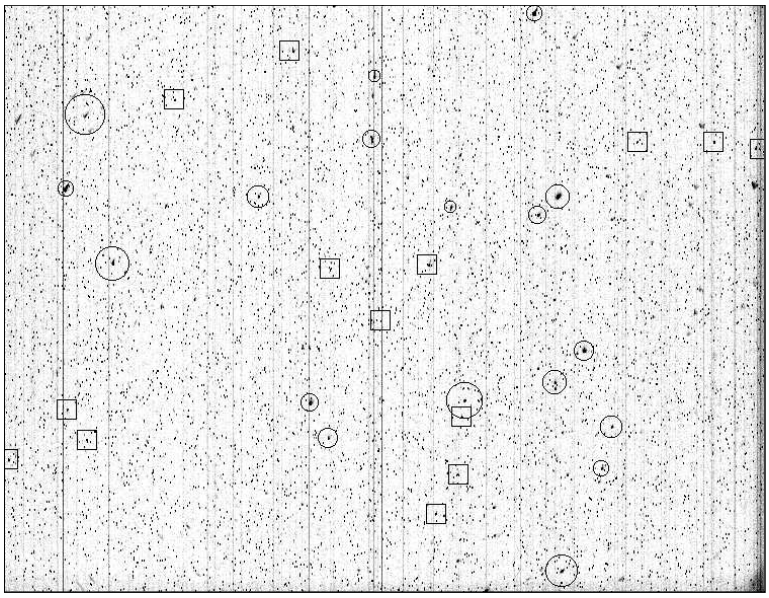

Figure 3.25: High temperature image after star-tracking. The radius of the 18 circles marking the recognized stars indicates the centroid/catalogue deviation. Unknown objects and rejected stars are marked with 14 rectangles.

determined from the SMART-1 experiences. The star-fields were projected onto the star-tracker using an optical stimulator, such that complex maneuvers could be programmed. During the test sequence, up to 51000 static hotspots and 1800 transient hotspots were injected by a simulation script in the star-tracker software. The star-tracker operated nominally during the full simulated maneuvers. A worldplot of one of the maneuvers is plotted in figure 3.26.

Out of the 616 attitude measurements performed during the maneuver, the 609 were correctly determined, corresponding to a validity of 98.9%.

3.4.3 Summary

Throughout this section, the SMART-1 case has been used to illustrate the dissertation work of developing a fast and reliable detection and discrimination of a specific source and drain motion field. The techniques that are focussed on application specific characteristics have been optimized towards discrimination of CCD radiation damages within the field of star-tracking.

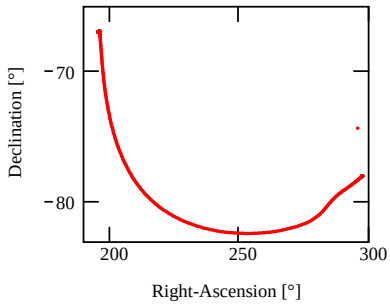

Figure 3.26: Worldplot from simulated maneuver in a high radiation environment. During the maneuver, 51000 static and 1800 dynamic hotspots were injected and discriminated in each image.

The techniques have been successfully verified in space onboard the SMART-1 satellite mission, being a reference worst case mission. Apart from the onboard star-trackers being operated in a relatively hot environment, the satellite has been subject to the worst solar mass ejections ever measured. During this solar storm, the satellite was flying through the van Allen belts, hereby accumulating substantial radiation damages to the star-tracker CCDs.

The techniques have further been characterized in a laboratory setup using an optical stimulator to project the star-field. A dedicated software test script was implemented to inject the hotspots in the acquired images before processing.

3.4.4 Recommendation for future work

Through this work a multistage filtering based on hotspot characteristics has been developed. The static hotspot population depends both on the temperature, the radiation dose sustained and the level of annealing, while the transient hotspot population depends on the present radiation level. In order to increase the overall robustness, autonomy may be built into the hotspot filter process such that the combination of filters is automatically optimized based on these dependencies. This level of autonomy is essential for autonomous star-tracking.

Chapter 4

Conclusion

Throughout this work, the field of system motion handling has been investigated. A special focus has been put on aerospace applications and the associated design drivers. A break-down of the field has identified the tasks of *characterization* of the system motion, *compensation* for the motion and the possibilities of *post-processing*. Focus within this work has mainly been put on the characterization and compensation tasks.

A selected subset of applications, each suffering from different types of image motion have been presented. These applications are all related to star-tracking. Through analysis, proposals for solutions have been derived. The solutions have been implemented and experimentally verified.

Star-tracking from rotating platforms is a type of system motion often encountered within aerospace. Traditionally, dedicated, less accurate, instruments have been used for attitude recovery. In this work, it was verified that a TDI motion compensated star-tracker could be utilized. Thus the high accuracy would be maintained while the total number of instruments was decreased. The analysis led to the design and implementation of a prototype TDI star-tracker, supporting 16 angular velocities in one direction. It was proven from real sky tests, that pointing accuracies below 7.5as is achievable for a rotation rate of $4°/s$ (corresponding to 13% field of view pr integration period). This measure includes all the external noise sources, e.g. the noise induced by the platform drives. Another, less accurate but highly indicative, measure indicates an independent pointing accuracy in the range of 1-2as. This measure is highly satisfactory and are comparable with the star-tracker performance in a stationary setup. Compensation for all rotation vectors parallel to the focal plane will require a different CCD technology (orthogonal transfer). Compensation of rotation vectors not parallel

to the focal plane cannot be performed using TDI. The test results prove that star-tracking at high angular rates can be efficiently performed using the time delayed integration technique, as long as the rotation vector is (close to) orthogonal to the optical axis. Such an orientation is easily achievable by design on "spinner" satellites, where the spacecraft is rotating at a certain rate in order to be less sensitive to external perturbation forces.

Onboard the Bering satellite mission, a science telescope used for target tracking will be pointed at the targets using a folding mirror. In order to remove control biases, a star-tracker will be put into the optical pathway, such that the absolute telescope pointing direction will be given at all times. It was verified whether a sufficient stability can be achieved, both for open-loop and closed-loop target tracking. The tracking must be performed autonomously including the necessary calibration processes. After development of the algorithms capable of performing the automated calibrations and the target tracking, the concept was tested on a small mobile science grade telescope. The closed loop testing was successfully maintained with a standard deviation in the range of 2-3as, wherefore the solution presented is found highly feasible. Using open loop control, compensation was achieved for 99.3% of the applied motion (in the given test setup). This is highly satisfactory for shorter image integrations periods. For longer integration periods this method can, in combination with other techniques such as image superpositioning, be applied to achieve non-smeared image acquisitions.

For high-accuracy demanding pointing missions, the accuracy of ∼1as obtained using modern autonomous star-trackers is not sufficient. The feasibility of a two-stage autonomous star-tracker was therefore examined. A prototype was implemented, realizing a focal-length ratio of 1:12 and a sensitivity ratio of 1:6, which was found to be a suitable mass/performance trade-off. Real-sky verifications of the setup proved an accuracy of 200-300mas within the rich star regions, and an accuracy of 700-800mas within the meagre star regions. These inaccuracy measures are slightly poorer than expected, and are traced to the star centroids being too inaccurately determined. A better performance is expected, if (when) the measurements are repeated at a high-altitude astronomical test site. For further performance improvements, the S/N ratio of the applied system must be decreased. It is therefore concluded that the star-tracker staging concept is highly feasible, but it poses high demands for the noise performance of the star-tracker imager.

For most aerospace applications the presence of the harsh ionizing radiation environment is a challenge. For star-tracking a particular radiation effect is the generation of additional charges on the acquired images,

hotspots, which are very similar to stars. Observed as an image sequence, these hotspots constitute a source and drain motion regime. Traditionally, pre-acquisition compensation has been applied, such as heavy and cumbersome particle shielding or active power-consuming CCD cooling. It was therefore investigated whether compensation could be implemented as a post-processing step. Algorithms based on particular hotspot features was developed and tested. Software filters based on these algorithms were successfully verified flying onboard the ESA SMART-1 spacecraft. After in-flight installment of these filters, the SMART-1 ASC star-trackers operated nominally during the Van Allen Belt passages as the first autonomous star-trackers. Furthermore, the installment of the filters increased the thermal operational envelope of the star-trackers by more than 20°C. The filters are further planned for several upcoming high-radiation satellite missions and have become an important part of the ASC star-tracker operational envelope. Based on the successful operation in space, it is concluded that CCD radiation damages can be efficiently discriminated from the star-tracker source images using post-processing up to a certain extent.

Bibliography

[1] Anja C. Andersen, René Michelsen, Henning Haack, and John L. Jørgensen. Bering - the first deep space mission to map asteroidal diversity, origin and transportation. In *Proceedings of International Conference on Recent Advanced in Space Technologies*, pages 361–367, Istanbul, Turkey, November 2003. ISBN 0-7803-8142-4.

[2] Centrovision. A primer on photodiode technology. http:// www.centrovision.com/ tech2.htm.

[3] Erik Dalsgaard, Torben Skettrup, and Mette Owner-Petersen. *Optik (optiske komponenter)*. Polyteknisk Forlag, 1989. ISBN 8-750-20686-9.

[4] T. Denver, J. L. Jørgensen, M. Betto, and P. S. Jørgensen. The bering target tracking instrumentation. In *Proceedings of International Conference on Recent Advanced in Space Technologies*, pages 250–254, Istanbul, Turkey, November 2003. ISBN 0-7803-8142-4.

[5] T. Denver, P.S. Jørgensen, and J.L. Jørgensen. High accuracy target tracking concepts. In *Proceedings of the 4th symposium - Small Satellites Systems and Services*, 2004.

[6] Troelz Denver, John L. Jørgensen, Troels Riis, and Maurizio Betto. The autonomy of the advanced stellar compass in-flight performance compared to on-ground testing. In *ESA Workshop on On-Board Autonomy*, pages 351–358, ESTEC, Noordwijk, The Netherlands, October 2001. ESA, ESA.

[7] Troelz Denver, Peter S. Jørgensen, John L. Jørgensen, Richard Shelton, Edwin Sousa, Joshua. Hoblitt, and Mike Maberry. Autonomous control of a mobile 20-inch outreach telescope using a star-tracker. In *2003 AMOS Technical Conference*, September 2003.

[8] Jens Eising. *Lineær algebra*. Stougaard Jensen/København, Matematisk Institut, Danmarks Teksiske Højskole, 1993. ISBN 87-88764-39-7.

[9] Peter Fortescue and John Stark, editors. *Spacecraft Systems Engineering*. John Wiley and sons, 2 edition, 1995. ISBN 0-471-95220-6.

[10] Berthold Klaus Paul Horn. *Robot Vision*. The MIT Press, 1986. ISBN 0-262-08159-8.

[11] Laura Køster Jensen and Troelz Denver. High accuracy intercalibration between the telescope and the image startracker on the bering mission. Report, Technical University of Denmark, June 2002.

[12] John L. Jørgensen, Troelz Denver, Maurizio Betto, and Peter S. Jørgensen. The bering autonomous target detection. In *Proceedings of International Conference on Recent Advanced in Space Technologies*, pages 361–367, Istanbul, Turkey, November 2003. ISBN 0-7803-8142-4.

[13] John Leif Jørgensen and Carl Christian Liebe. The advanced stellar compass, development and operations. *Acta Astronautica*, 39:775–783, November 1996. Elsevier.

[14] P. S. Jørgensen, T. Riis, M. Betto, and A. J. Pickles. Ascfit - automatic stellar coordinate fitting package. In *Astronomical Data Analysis Software & Systems XI*, Victoria, 2001.

[15] Peter S. Jørgensen. *Inter-calibration of accurate attitude instruments*. Phd thesis, Technical University of Denmark, August 2002. ISBN 87-91184-12-6.

[16] Peter S. Jørgensen and John L. Jørgensen. Smart-1 performance summary of the advanced stellar compass star tracker from launch to 7000km perigee. Summary, Technical University of Denmark, Ørsted•DTU, December 2003.

[17] Hyunjae Lee, Choong-Suk Oh, and Hyochoong Bang. Modified grid algorithm for star pattern identification by using star trackers. In *Proceedings of International Conference on Recent Advanced in Space Technologies*, pages 361–367, Istanbul, Turkey, November 2003. ISBN 0-7803-8142-4.

[18] Kevin Ng. Technology review of charge-coupled device and cmos based electronic imagers. http:// www.eecg.toronto.edu/˜kphang/ papers/ 2001/ ng_CCD.pdf.

[19] Khalid Sayood. *Introduction to Data Compression*. Morgan Kaufmann Publishers, 1996. ISBN 1-55860-346-8.

[20] Robert J. Schalkoff. *Digigal Image Processing and Computer Vision*. John Wiley & Sons, inc, 1989. ISBN 0-471-50536-6.

[21] Sony, Japan. *CCD Area Image Sensor*, '94 - '95 edition, September 1994.

[22] Per Lundahl Thomsen and Flemming Hansen. The bering mission space segment. In *Proceedings of International Conference on Recent Advanced in Space Technologies*, pages 361–367, Istanbul, Turkey, November 2003. ISBN 0-7803-8142-4.

[23] Eric W. Weisstein. Mirror symmetry. From *MathWorld*–A Wolfram Web Resource. http://mathworld.wolfram.com/MirrorSymmetry.html, 1999–2004.

[24] James R. Wertz, editor. *Spacecraft Attitude Determination and Control*. D. Reidel Publishing Company, 1978.

[25] Charles Woodworth. How photographic film works - developing film: Color. http://science.howstuffworks.com/film8.htm.